An Observational Study of the Tropical Tropospheric Circulation

Ioana M. Dima

A dissertation submitted in partial fulfillment of
the requirements for the degree of

Doctor of Philosophy

University of Washington
2005

Program Authorized to Offer Degree: Department of Atmospheric Sciences

University of Washington
Graduate School

This is to certify that I have examined this copy of a doctoral dissertation by

Ioana M. Dima

and have found that it is complete and satisfactory in all respects,
and that any and all revisions by the final
examining committee have been made.

Co-Chairs of the Supervisory Committee:

John M. Wallace

John M. Wallace

Dennis L. Hartmann

Dennis L. Hartmann

Reading Committee:

John M. Wallace

John M. Wallace

Dennis L. Hartmann

Dennis L. Hartmann

Edward S. Sarachik

Edward S. Sarachik

Date: 10/26/2005

In presenting this dissertation in partial fulfillment of the requirements for the doctoral degree at the University of Washington, I agree that the Library shall make its copies freely available for inspection. I further agree that extensive copying of the dissertation is allowable only for scholarly purposes, consistent with "fair use" as prescribed in the U.S. Copyright Law. Requests for copying or reproduction of this dissertation may be referred to Proquest Information and Learning, 300 North Zeeb Road, Ann Arbor, MI 48106-1346, to whom the author has granted "the right to reproduce and sell (a) copies of the manuscript in microform and/or (b) printed copies of the manuscript made from microform.

Signature Joana Lima

Date 10/26/2005

University of Washington

Abstract

An Observational Study of the Tropical Tropospheric Circulation

Ioana M. Dima

Chairperson of the Supervisory Committee:
Professor John M. Wallace
Department of Atmospheric Science

This observational study focuses on four different aspects of the general circulation of the tropical troposphere: the seasonality of the mean meridional circulation (MMC), the zonal momentum balance of the tropical troposphere, the structure of the equatorial stationary waves and the variability of the equatorial stationary waves.

The annual march of the climatological MMC is shown to be dominated by two components of comparable mean-squared amplitude: 1) a seasonally invariant pair of "Hadley cells" with rising motion centered just to the north of the equator and subsidence in the subtropics, and 2) a seasonally reversing, sinusoidally varying "solsticial" cell with ascent in the outer Tropics of the summer hemisphere and subsidence in the outer Tropics of the winter hemisphere.

The analysis of the seasonal cycle of the zonal-mean zonal momentum balance in the tropics shows that the climatological stationary waves in the tropical upper troposphere produce an equatorward eddy flux of westerly momentum in the equatorial belt. The resulting westerly acceleration is balanced by the advection of easterly momentum associated with the cross-equatorial MMC. The eddy momentum fluxes and the cross-equatorial flow are strongest during the monsoon seasons.

The three-dimensional analysis of the annual mean equatorial stationary waves in the ECMWF model reveals a complex vertical structure of various fields associated

with these waves. There seems to be something 'special' about the warm pool that enables the planetary-scale ascent to extend higher than elsewhere in the tropics. It is conceivable that the slow, hydrostatically-balanced ascent in the planetary-scale stationary waves in this region rather than the updrafts in the convective clouds is responsible for maintaining the extremely cold temperatures in the tropopause transition zone in this region.

The main modes of tropical variability (ENSO, the MJO and the annual cycle) are shown to share a number of common characteristics: they can all be described as oscillations of the planetary-scale waves between two preferred states. One state can be described as a *relaxed* pattern, in which the geopotential height is practically flat over the whole tropical belt and the zonal and meridional winds in the equatorial belt are relatively weak. Such a state is characteristic of situations with reduced precipitation over the warm pool and a weakening of the equatorial cold tongue in the Eastern Pacific. The *perturbed state* can be generally described as having opposite characteristics to the relaxed state.

Table of Contents

List of Figures

List of Tables

Acknowledgements

Foremost I would like to thank my advisor, Professor Mike Wallace. He has been a model of scientific excellence and generous mentorship. I deeply appreciate his guidance, support, patience and understanding, as a teacher, a researcher and a friend. I admire his incommensurable knowledge, his real zest for science and unmatched modesty. Most of all, I am grateful that he gave me the opportunity to come and study with him, in one of the most prestigious Atmospheric Science departments in the world.

Thank you to my committee, Professors Dennis Hartmann, Ed Sarachik and Chris Bretherton, for reading my thesis and providing me with very useful comments and suggestions. I would also like to acknowledge Professors James Holton and Peter Hobbs, who, unfortunately, are no longer with us. They have always encouraged and supported me throughout my graduate school years.

In JISAO, I appreciated Todd's help with many computer and research related problems, as well as his daily Romanian salutation. Kevin and Justin have proved to be one of the nicest people I have ever met, very considerate, helpful and fun. I also enjoyed very much my interaction and collaboration with Ian, which resulted in a published paper together; we had many interesting talks and I want to thank him for that valuable experience.

Thank you to my very good friends Socorro, Robb, Tom, Ignatius, Nadine, Bobby, who have helped make my life, inside and outside of school, a lot more fun and a lot

more interesting. They have been a constant support and a source of good time. Special thanks go to my closest friend, Roberta … we have so many nice memories together … for sure life in grad school would not have been the same without her.

This thesis would never have been completed without the continuous moral support, unconditional love and total devotion of my family in Romania. I want to thank Mihai, the other atmospheric scientist in our family, for always encouraging me and building up my confidence, for reading my thesis and giving me good feedback, for including my research in his sphere of interest and for opening my eyes to many other interesting problems outside the immediate subject of my thesis. Thank you also to Gabriel for always being there for me, ready to listen to all my problems, giving me well thought advices and, not last, for solving (by phone!) all the computer problems I have ever had. I don't know what I would have done without him.

I am grateful to my Mom and Dad for making me who I am, teaching how to live my life in good spirits and how to achieve any goals through much work, persistence and resilience. I dedicate this PhD thesis to them!

Thank you Jason for the love and support you have surrounded me with all this time, for making me happy and bringing joy into my everyday life. Any achievement I may have won't make much sense if I didn't share it with you.

Dedication

Parintilor mei, cu multa dragoste!

Multumesc!

1. Introduction

The present study aims to extend our understanding of the general circulation of the tropical troposphere. Most of the features that we are concerned about are visible in the satellite view of Earth shown in Figure 1.1. Persistent dry zones in the subtropical region are separated by a near-equatorial convection belt, suggestive of the existence of a systematic mean meridional circulation. The zonally symmetric features coexist with longitudinal asymmetries, the signature of the equatorial planetary waves. The most extensive cloud coverage area is located over the Indian Ocean in this image and, more typically, over the maritime continent. Not visible in this figure but an important aspect of the general circulation is the zonal wind field, which is also considered in this study.

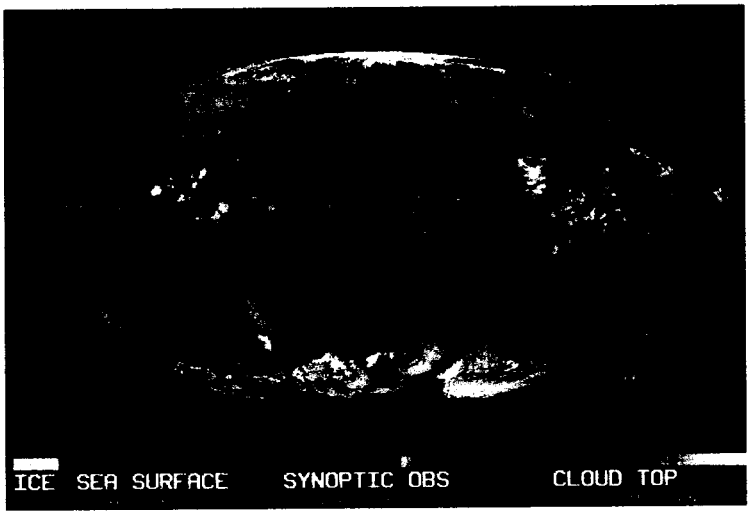

Figure 1.1: Satellite view of the Earth's cloud cover. (http://www.ssec.wisc.edu/data/composites.html)

The multi-scale interactions that extend the influence of the tropical atmosphere and oceans to other regions of the globe were the central focus of the Tropical Ocean - Global

Atmosphere (TOGA) program (Webster and Lukas, 1992; McPhaden et al, 1998). The program afforded the opportunity to closely examine the worldwide impacts of the tropical sea surface temperatures, especially those originating in the Pacific Ocean. There is also evidence that the tropics play an important role in glacial-interglacial transitions (e.g. Seltzer et al., 2002; Lea et al., 2003). The question of whether the tropics are a trigger of climate change or an amplifier of changes that started elsewhere has yet to receive a definite answer, but in either case it is important to understand how the tropical circulation is maintained and how it influences the global climate. A first step in this direction is acquiring a deeper understanding of the tropical circulation itself.

The present study is concerned with several aspects of the observed tropical general circulation that have not yet been thoroughly documented and diagnosed:

- the annual-mean and seasonally varying mean meridional circulation,
- the tropical momentum fluxes in the context of angular momentum budget of the equatorial belt,
- the annual-mean three-dimensional structure of the equatorial stationary waves, with its dominant equatorially symmetric component,
- the seasonal, inter-annual and intra-seasonal variability of the equatorial stationary waves.

The analysis relies heavily on data from NCEP and ERA40 Reanalyses, and covers the entire tropical troposphere, with the main focus on upper tropospheric levels. It encompasses both the annual-mean and the variability about the annual-mean: the seasonally-varying climatological means, the inter-annual and the intra-seasonal

variability. In the space domain, we focus exclusively on motions and features of planetary scale, both in the zonal mean and in the departures from the zonal mean.

In the remainder of this section we provide some background on the features of the tropical general circulation that were investigated in this study.

1.1 The mean meridional circulation

The zonally symmetric circulation of the atmosphere has attracted the interest of scientists for over 300 years. In 1686 Halley described and mapped the geographical distribution of the trade winds, as shown in Figure 1.2. He interpreted the trade winds as being part of the lower branch of a meridional cell driven by rising air in the tropics and sinking air at the poles. However, he was unable to explain the persistent westward component of the equatorial winds. The idea of a direct meridional cell driven by low-latitude heating was reintroduced and reinforced by Hadley (1735), who realized that the Earth's rotation plays a crucial role in determining why these winds have an easterly component.

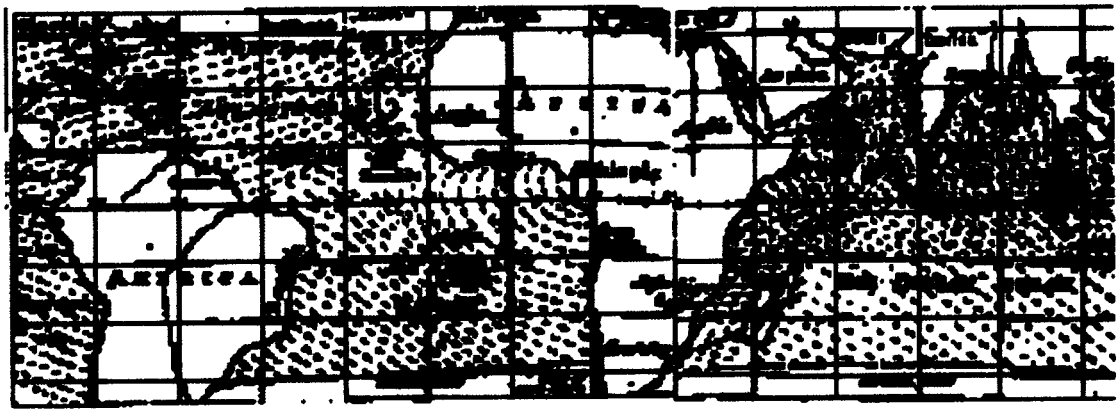

Figure 1.2: The first documented map of the trade winds, drawn by Edmond Halley in 1686.

Following Hadley's work, more comprehensive observations have been acquired and improved numerical models have been used to test theoretical ideas and diagnose dynamical processes. For a thorough review of the historical developments in this field see Lorenz (1967, pages 1-9 and 59-78).

Several more recent contributions to the progress in understanding the zonal mean meridional circulation are particularly relevant to the present study. Schneider and Lindzen (1977) developed a linear, axially symmetric, steady-state model capable of simulating many aspects of the annual mean, zonally averaged circulation. The essential ingredients in their model were latent heat release and cumulus friction. Their simulated Hadley circulation, shown in Figure 1.3a, has realistic dimensions and is approximately half the strength of the observed. In a follow-up paper, Schneider (1977) extended the analysis by taking into account the nonlinear effects (i.e., the advection of zonal momentum by the meridional motions) and he required the motions to satisfy a form of angular momentum conservation. In this nonlinear version, weak Ferrel cells are observed in both hemispheres and the strength of the Hadley cell has increased to about 70% the strength of the observed circulation (Figure 1.3b).

In both these papers the authors emphasize the importance of the dynamics of the zonally symmetric circulation, as opposed to the eddy fluxes, in determining key features of the general circulation. Although they obtained fairly realistic simulations of the tropical temperature fields and the mean meridional circulation, their results depart significantly from observations with respect to the strength of the zonal winds: the westerly jets were far too strong. They attributed these differences to the effects of

zonally asymmetric and transient motions, which were not included in their simulations. The role of the eddies along with the zonal mean processes was explicitly considered by Schneider (1984). The author was able to obtain quite realistic simulations of the zonal mean circulation and temperature field and he also obtained fairly realistic zonal winds (much reduced in strength compared to those in his previous simulations).

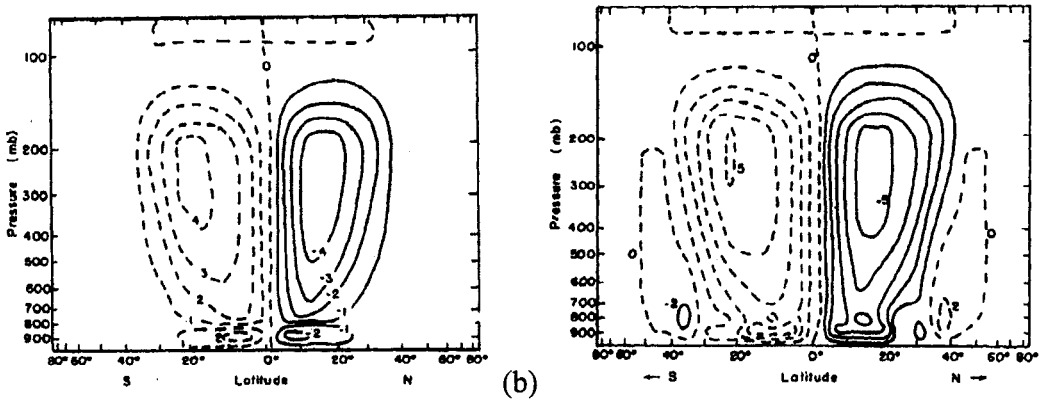

Figure 1.3: Mean meridional circulation in a (a) linear (Schneider and Lindzen, 1977, Fig. 12) and (b) nonlinear (Schneider, 1977, Fig. 5) axially symmetric model. Streamfunciton contour interval: 10^{13} g s^{-1}.

Held and Hou (1980) developed a simple approximate theory for the case in which the atmospheric fluid is sufficiently inviscid that the poleward flow in the Hadley cell nearly conserves angular momentum. They used a nonlinear, axially symmetric model and focused on identifying the parameters that control the width of the Hadley cell, the total poleward mass flux (i.e., the strength of the cell), the latitude of the upper level jet in the zonal wind and the distribution of surface easterlies and westerlies.

With minor exceptions, most of the theoretical studies up to this point considered the heating distribution to be symmetric about the equator. Motivated by observational results of Oort and Rasmusson (1970), similar to those shown in Figure 1.4, Lindzen and

Hou (1988) argued that the equatorial symmetry of the MMC is largely an artifact of time averaging over the year, and that at any given time, the circulation is more likely to reside in a "solsticial" regime, with the Hadley cell straddling the equator and ascent in the tropics of one hemisphere and sinking in the subtropics of the other hemisphere.

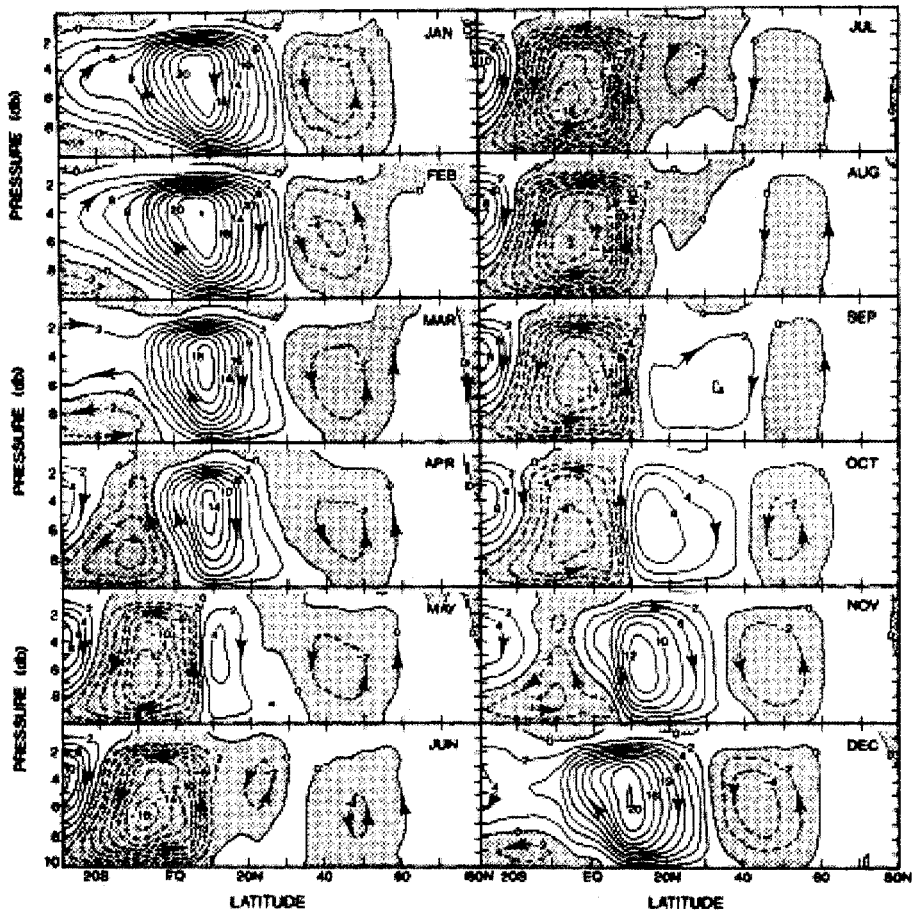

Figure 1.4: Annual cycle of the of the zonal-mean mass streamfunction in units of 10^{10} Kg s^{-1}, based on 1964-89 radiosonde data. (Oort and Yienger, 1996, Fig. 3).

To explain this preference for equatorial asymmetry, they argued that the conventional annual-mean Hadley cell is too strong to be the result of equatorially

symmetric forcing, and consequently that the equatorially asymmetric forcing is then essential for explaining the annual mean climatology.

Lindzen and Hou supported this argument with a series of numerical experiments with an axisymmetric model. They found that small equatorial asymmetries in the prescribed heating give rise to large equatorial asymmetries in the forced mean meridional circulation. In subsequent theoretical studies, Fang and Tung (1999) looked at the influence of an annually-varying heating source on the mean meridional circulation and noticed that, compared to the steady-state solutions, the change in the meridional circulation, as the center of the heating is moved off the equator, is less abrupt.

In Chapter 3 of this thesis, based on Dima and Wallace (2003), we reexamine the observational basis for Lindzen and Hou's assertion that solsticial regimes with strong equatorial asymmetry are the favored configuration of the tropical mean meridional circulation. We will show that the annual march of the climatological mean meridional circulations is, in fact, dominated by two components of roughly comparable mean-squared amplitude: 1) a seasonally invariant pair of "Hadley cells" with rising motion centered near and just to the north of the equator and subsidence in the subtropics, and 2) a seasonally reversing, sinusoidally varying "solsticial" cell with ascent in the outer tropics of the summer hemisphere and subsidence in the outer tropics of the winter hemisphere. The meridional structure and seasonal evolution of the solsticial cell are suggestive of a close association with the monsoons.

1.2 The zonal momentum balance in the equatorial belt

A limited number of observational studies, of Starr et al., (1970), Rosen and Salstein (1980), Oort and Peixoto (1983) and Peixoto and Oort (1992), have shown the existence of low latitude eddy momentum fluxes directed towards the equator, implying an equatorial source of wave activity and a convergence of westerly momentum in the equatorial belt. These fluxes are evident in Figure 1.5, from Peixoto and Oort (1992). But almost exclusively these studies focused on the dominant *extratropical* features in the momentum balance and did not comment extensively on the low latitude, equatorward fluxes.

Results of theoretical studies of Suarez and Duffy (1992), Saravanan (1993), Kraucunas and Hartmann (2004) and others, indicate that zonally asymmetric heating in the equatorial region induces equatorward momentum fluxes that drive an intense westerly jet centered over the equator, in the upper troposphere. This type of circulation is referred to as equatorial *superrotation.* However, despite the modeled and observed equatorward fluxes of westerly momentum, the annually and zonally averaged zonal winds in the tropical upper troposphere are characterized by weak easterlies and there is no evidence of an equatorial westerly jet.

Lee (1999) addressed the question of why are the climatological zonal winds easterly in the equatorial upper troposphere, in the presence of the observed westerly acceleration in the equatorial belt due to the convergence of the eddy flux of westerly momentum. As shown in Figure 1.6, she computed and analyzed different terms in the momentum

balance at a single tropospheric level (200hPa), and showed that the advection of easterly momentum by the seasonally varying, equatorially asymmetric component of the mean meridional circulation plays a critical role in balancing the westerly acceleration on the equator due to the eddy flux convergence.

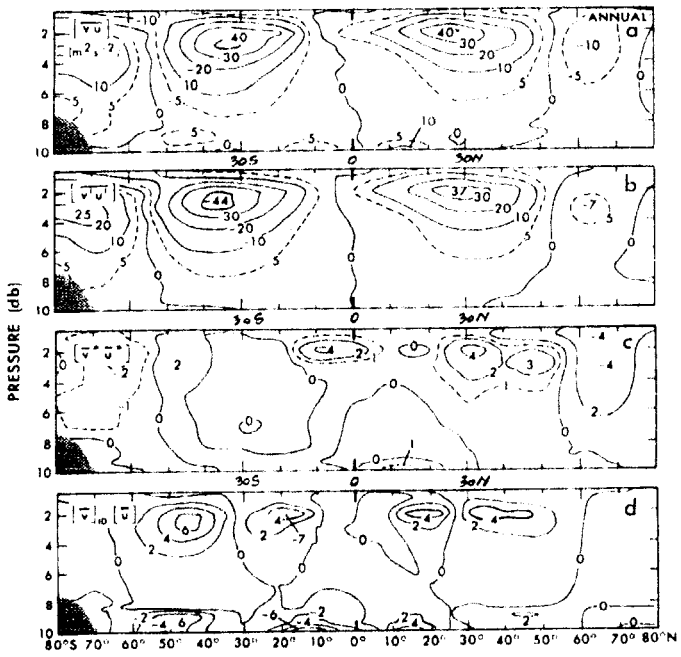

Figure 1.5: Zonal-mean cross sections of the northward flux of momentum by (a) all motions, (b) transient eddies, (c) stationary eddies and (d) mean meridional circulations, in m^2s^{-2}, for annual-mean conditions. (Peixoto and Oort, 1992, Fig. 11.7).

The limited spatial domain and the specific temporal decomposition and equations employed by Lee (1999) imposed certain limitations to her investigation of the tropical momentum balance. We examine this problem in more detail in Chapter 4 of this thesis and in Dima et al. (2005). We document the vertical and latitudinal structure of the equatorward momentum fluxes due to eddies with different time scales, and compare the leading terms in the zonal momentum balance. The temporal separation employed here enables us to underline the key role played by the standing eddies compared to that

played by inter- and intra-annual transient eddies emphasized in Lee (1999). The seasonal variability is considered in a comprehensive way, by analyzing both the transition seasons as well as the monsoon seasons. We also point out the remarkable degree of equatorial symmetry of the climatological-mean equatorial stationary waves, even during the monsoon seasons when the strongest heating is off the equator. The planetary-waves forced by tropical heat sources in a shallow water wave equation model exhibit a similar tendency toward equatorial symmetry.

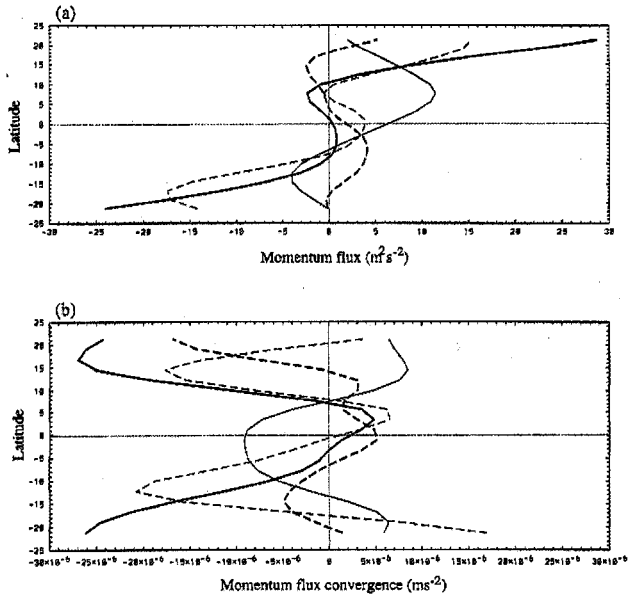

Figure 1.6: (a) Momentum fluxes and (b) momentum flux convergences, by transient eddies (thick solid line), stationary eddies (thick dashed line), transient meridional circulation (thin solid line), and mean meridional circulation (thin dashed line) at the 200-mb level. (Lee, 1999, Fig. 1).

1.3 The stationary waves

The tropical stationary waves, also known as standing eddies, are forced primarily by land-sea thermal contrasts, orography and longitudinal contrasts in sea surface temperature, mediated by the release of latent heat. In the course of our analysis of the

zonally symmetric circulation, we became aware that these waves are primarily responsible for the equatorward flux of westerly momentum in the tropics. Hence, in our subsequent work, we focused on investigating the three-dimensional structure and temporal variability of these waves (Chapters 5 and 6, respectively). While in our previous work the zonally asymmetric circulations were analyzed primarily from the point of view of their role in the zonally averaged momentum balance, here we are particularly interested in the longitudinal and vertical structure of these waves.

The horizontal structure of the stationary waves can be represented either in terms of the streamfunction or geopotential height fields. Because the height perturbations in the tropics are about an order of magnitude smaller than those in the extratropics, the streamfunction field has been more widely used in describing the structure of stationary eddies in studies that extend into the tropics. But since the streamfunction, by construction, represents only the rotational (nondivergent) component of the wind field and since the divergent and rotational components of the wind in the equatorial belt are of equal magnitude, the streamfunction representation is of limited value. Hence we chose to work with the geopotential height to represent the stationary waves throughout our study.

Much of our current understanding of equatorial planetary waves is based on theoretical studies of Matsuno (1966), Webster (1972) and Gill (1980). Matsuno considered the steady-state planetary-wave response to a mass source/sink, in a linearized barotropic model on an equatorial beta-plane. For a mass source/sink centered on the equator he found that the solution consisted of the combination of an eastward-

propagating Kelvin-wave and a westward propagating Rossby-wave. Webster (1972) computed the response in a two-layer model with perturbations to a mean flow like that observed and with a localized heating source (Figure 9 in Webster, 1972). He focused on the flow to the east of the forcing region which he correctly interpreted in terms of a Kelvin wave. Gill (1980) considered the analogous problem in his two-layer baroclinic model forced by a heat source/sink and obtained solutions that had similar horizontal structure as his predecessors but were easier to interpret. The flows in the upper and lower layers were in the opposite sense and Gill explained the vertical structure in his model as the first baroclinic mode of the response to a mid-tropospheric heat source that represents the effects of deep cumulus convection.

The horizontal structure of the pressure and horizontal wind field in the lower layer of Gill's (1980) solution for the response to an isolated stationary heat source is shown in Figure 1.7. The forcing is located at the longitude where maximum convergence is observed. The Rossby-wave component of the solution is dominant to the west of the forcing and the Kelvin-wave to the east.

More recently, nonlinear solutions to the shallow water wave equation were also considered (e.g. Van Tuyl, 1986). Using an idealized one-layer model, for a hydrostatic shallow-water system of equations on an equatorial beta-plane, Van Tuyl (1986) calculated the nonlinear response to tropical wave forcing heating. He noted that the low latitude velocity and longitudinal geopotential difference tend to be most affected by nonlinearity (generally, for nonlinear runs, the zonal wind and the geopotential gradient tend to become stronger along and near the equator).

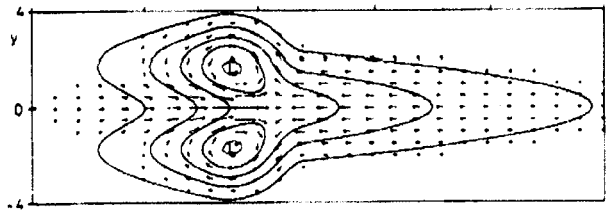

Figure 1.7: The linear planetary wave response to an isolated mid-tropospheric heat source symmetric about the equator, on an equatorial β -plane. The contours represent perturbation pressure.
(Gill, 1980, Fig. 1)

To better understand the modeled stationary wave response, including the nonlinear effects, we also performed a series of runs using a simple model built by James Holton. The model is based on the same set of nonlinear equations used by Van Tuyl (1986). The solution, shown in Figure 1.8, replicates many of the features in the observed upper tropospheric flow, as discussed in more detail in Chapter 4.

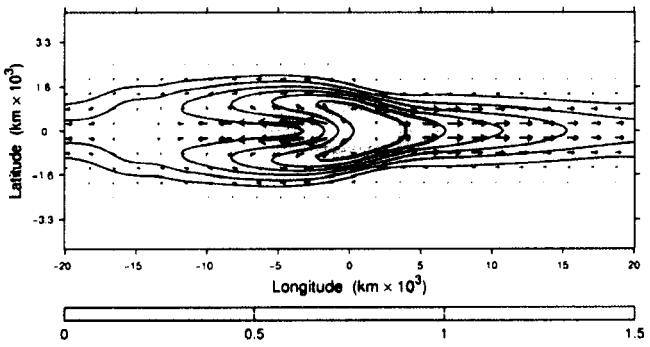

Figure 1.8: Nonlinear solution of the shallow water wave equation forced by an equatorial heat source. The geopotential height field is contoured, the wind field is represented by arrows and the heat source is shown in color. The response bears a strong qualitative resemblance to the observed zonal variations in the geopotential height and wind fields.

Gill's (1980) model and the theoretical representations closely related to it, offer a simplified approach to the problem of tropical stationary waves and we repeatedly make reference to these in our study. However, the simplicity of this model also works to its disadvantage. It should be noted that there are a set of problems associated with this

model, as, for example, the selection of a single vertical sinusoid mode to represent the heating source, the heating being artificially brought down to the surface or the implicit imposed lid at the top of the heating layer (e.g., Wu et al., 2000a,b; Chiang et al., 2001). But most of these problems involve inconsistencies in the representation of surface fields. Since our main focus is, in fact, the representation of upper tropospheric fields, a region where Gill's representation has greater validity, we feel that a qualitative comparison of the observed fields at these levels with fields given by the model has a certain value to it.

The heating source in Gill's model was related to the observed distribution of tropical rainfall. The dominant features of the upper tropospheric standing eddies are located over the Pacific sector, the region with the most prominent east-west differences in tropical convection. The existence of mean cold sea surface temperatures in the eastern part of the equatorial Pacific and warm ocean waters in the western Pacific results in a tendency for the air to rise over the Indonesian region and sink over the eastern Pacific (Figure 1.9). These ascending and descending motions are accompanied by easterly wind flow at lower levels and balancing eastward-blowing winds at upper levels. The circulation that develops in the longitude-height plane is known as "the Walker circulation" (Bjerknes, 1969), named after Sir Gilbert Walker (1868-1958), a renowned British mathematician and meteorologist (the discoverer of the 'Southern Oscillation', Walker, 1924). Analogous circulation cells, of less intensity, are also recognizable over the Indian and Atlantic Oceans (Peixoto and Oort, 1992). Our results confirm that the Walker circulation represents an important part of the tropical stationary waves.

Most of the literature on the seasonal variability of the stationary waves emphasizes the monsoons, which are forced by the annual cycle in solar declination angle. Deep convection of the warm continents of the summer hemisphere gives rise to seasonally reversing equatorially asymmetric circulations, which are strongest about a month after the solstices. In this study we are primarily concerned with the annual variation of the *equatorially symmetric* component of the stationary waves. This component is mainly forced by the weakening of the Pacific and Atlantic equatorial cold tongues in sea surface temperature around March/April each year (Mitchell and Wallace, 1992). We will show that the weakening of the equatorial cold tongue in March/April is followed by a weakening of the stationary waves about a month later.

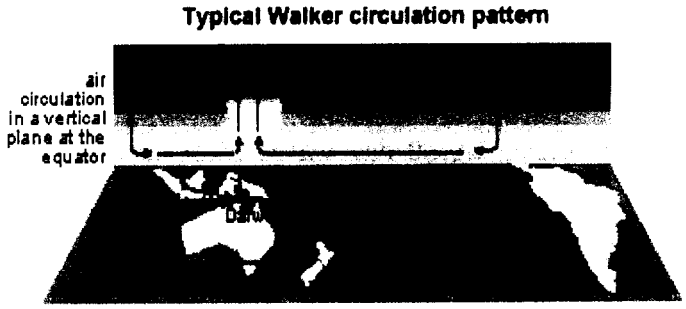

Figure 1.9: The Walker circulation. (http://www.bom.gov.au/lam/climate/levelthree/analclim/elnino.htm)

El Niño / Southern Oscillation (ENSO) is the most prominent known source of inter-annual variability in the tropical climate and around the world. It results from the coupled interaction between atmosphere and ocean in the Pacific basin and it is observed when the easterly trade winds weaken and warmer waters of the western Pacific migrate eastward, eventually reaching the South American coast (e.g. Rasmusson and Carpenter, 1982, Wallace et al., 1998).

The Madden-Julian Oscillation (MJO) dominates the intra-seasonal tropical variability and it is characterized by a pulsation and eastward propagation of a broad area of convection over the Indo-Pacific warm pool region. The associated zonal wind anomalies at upper levels often propagate around the full circumference of the globe (Madden and Julian, 1994; Hsu, 1996).

Given the large difference between their respective time scales, the inter-annual ENSO and the intra-seasonal MJO have usually been considered in separate studies. However, a number of studies have pointed out the spatial similarities between the anomalous circulation and convection patterns associated with these leading modes of variability (Barnett, 1984; Lau and Chan, 1988; Lau and Shen, 1988). For example, Lau and Chan (1988) performed EOF analyses of the tropical variability and identifies a pattern of convection associated with the Walker circulation which was characterized by fluctuations at three time scales: 40-50 day waves associated with MJO, the ENSO-related inter-annual variations and the annual modulation.

In Chapter 6 we look at these phenomena from the perspective of the tropical stationary waves, with emphasis on the total fields rather than the anomaly field. We will show that all three phenomena involve alternate strengthening and weakening of the stationary waves, but each exhibits a slightly different spatial signature.

2. Data and Analysis Techniques

2.1 Data sets

The two main data sets used in the present study were the National Center for Environmental Prediction / National Center for Atmospheric Research (NCEP / NCAR) Reanalysis (Kalnay et al., 1996) provided by the National Oceanic and Atmospheric Administration (NOAA) Climate Diagnostics Center (CDC), and the Reanalysis project ERA-40 (Simmons and Gibson, 2000; http://data.ecmwf.int/data) of the European Center for Medium-range Weather Forecasts (ECMWF). These data are both mapped on a 2.5°x2.5° global latitude / longitude grid. In the vertical the NCEP reanalysis data are available on 17 levels corresponding to the 1000, 925, 850, 700, 600, 500, 400, 300, 250, 200, 150, 100, 70, 50, 30, 20, 10 hPa pressure surfaces. In addition, the ERA-40 reanalysis also includes the 775, 7, 5, 3, 2 and 1 hPa levels. The domain of our study usually extends up to 50hPa. Although both NCEP and the ERA40 represent model output products, we will refer to these data as 'observations', throughout this study.

Also used in our analyses is the precipitation field produced by the Climate Prediction Center (CPC) Merged Analysis of Precipitation (CMAP). The product is mapped on a 2.5°x2.5° global grid and consists of merged data from rain gauges and precipitation estimates derived from several satellite-based algorithms.

In describing the tropical mean meridional circulation (MMC) we used the Stokes streamfunction ψ, derived from the continuity equation of mass in zonally averaged form (Peixoto and Oort, 1992):

$$\frac{1}{R\cos\phi}\frac{\partial[\overline{v}]\cos\phi}{\partial\phi}+\frac{\partial[\overline{\omega}]}{\partial p}=0 \qquad (2.1)$$

The streamfunction field is introduced such that:

$$[\overline{v}]=\frac{g}{2\pi R\cos\phi}\frac{\partial\psi}{\partial p} \quad ; \qquad [\overline{\omega}]=-\frac{g}{2\pi R^2\cos\phi}\frac{\partial\psi}{\partial\phi} \qquad (2.2)$$

To calculate ψ, we performed a downward integration of the observed meridional mass flux $[\overline{v}]$, using data at all available pressure levels (10 - 1000 hPa). At the top of the atmosphere the streamfunction field is assumed to be zero ($\psi=0$). A small correction is applied at the lowest four levels to ensure that $\psi=0$ also on the bottom boundary.

2.2 Time and space considerations

Due to uncertainties regarding the reliability of the global data prior to 1979 when satellite soundings became routinely available on a global scale, we restricted our analyses to the 1979-2001 time interval. The robustness of our results with respect to the global warming trend that characterizes this specific period is considered in Appendix A. Most of our results are based on monthly averaged data, but for specific purposes daily values and pentad (5-day) means were also considered. Aside from specifically defined seasonal averages, all months (or pentads) of the year were taken into account in our analyses.

In Chapter 4 the time averaging is performed as follows: the daily data are first averaged over each of the 73 pentads (i.e. January 1-5, January 6-10, etc.) of a calendar year, then the means from each individual pentad (including covariance quantities) are

averaged over the 23-year period of record to obtain 73 climatological-mean pentad-mean values for each variable. Finally, the climatological-mean pentad-mean data are averaged over individual months, seasons and the entire year to obtain monthly, seasonal, and annual-mean values, respectively, for each variable.

Means of 6 consecutive pentads within January-February (JF) and July-August (JA), the times of the strongest mean meridional circulations, are used in Chapter 4 to represent what we will refer to as the "monsoon seasons", and intervals of comparable length within April-May (AM) and October-November (ON), when the Hadley circulations in the Northern and Southern Hemispheres are of comparable intensity, are used to represent the "transition seasons" (Table 2.1). The features emphasized in this study are generally robust with respect to the definition of the monsoon and transition seasons. For example, similar results are obtained when the seasons JF, AM, JA and ON are defined on the basis of calendar months.

***Table 2.1**: Seasons as defined in Chapter 4*

Season	Pentads	Dates
JF	4-9	Jan 16 - Feb 14
AM	21-26	Apr 11 - May 10
JA	40-45	Jul 15 - Aug 13
ON	58-63	Oct 13 - Nov 11

Throughout the study, the following notation is used: $\bar{x}$ denotes the time average over a specified period, $(x)' = x - \bar{x}$, the departure from the time average, $[x]$, the zonal average and $(x)^* = x - [x]$, the departure from the zonal average.

2.3 Analysis techniques

Throughout the study we used both total fields and anomaly fields. **Anomalies** were calculated by subtracting the 1979-2001 climatological-mean for each calendar month (or pentad) from the values for a month (or pentad) for a particular year.

To determine the primary modes of variability in various fields we used Empirical Orthogonal Function (**EOF**) analysis, also referred to as Principal Component Analysis (PCA) (Lorenz, 1956, Kutzbach, 1967). The EOFs represent the eigenfunctions of the covariance matrix of various state parameters (geopotential height, temperature, pressure etc) in the space domain. The associated principal components (PCs) document the amplitude and polarity of the EOF defined structures, in the time domain. The eigenvalue characterizing each EOF mode is a positive definite number indicative of the amount of variance explained by that eigenvector. Previous to performing the EOF analysis, all data are weighted by the square root of cosine of latitude to ensure that equal areas are given equal weight in terms of variance. When EOF analysis was performed on fields in the vertical domain, data were also weighted by increments of the pressure that they represent. Unless otherwise noted, the EOFs presented in this study are well separated from subsequent eigenvectors, according to the criterion of North et al. (1982).

In isolating combinations of patterns within two fields that tend to be linearly related we used the Maximal Covariance Analysis (**MCA**). The method identifies pairs of spatial patterns that explain as much as possible of the mean-squared temporal covariance between the two fields (Bretherton et al., 1992).

The **compositing** technique consists of sorting the data into categories with respect to a specific event signal, averaging the data in each category and then comparing the means for the different categories. In our study the basis for compositing are indices describing specified atmospheric oscillations. We used the ten top/bottom extreme values of the index to composite the data (total fields) and separate the event signal from other influences. The results were tested for significance by evaluating their consistency with a well-founded theory and also, in some cases, by dividing the dataset into subsets and checking that the derived relationships prevail in each of the subsets.

The **correlation** coefficient between two time series x and y is given by:

$$r = \frac{1}{T}\sum_{i=1}^{T}\frac{(x(i)-\bar{x})\cdot(y(i)-\bar{y})}{\sigma(x)\cdot\sigma(y)} \tag{2.3}$$

where T is the number of samples in the time domain and σ is the standard deviation. The statistical significance of the correlation coefficients was established using the Student t-statistic .

In order to recover the spatial patterns in different variables that go together with specific modes of variability, we **regressed** the unweighted anomaly fields (x) upon standardized indices (y), at each grid point j, using:

$$X(j) = \frac{1}{T}\sum_{i=1}^{T}\frac{(x(i,j)-\bar{x}(j))\cdot(y(i)-\bar{y})}{\sigma(y)} \tag{2.4}$$

The time series used in our regressions are standardized and dimensionless, hence the values in the regression maps represent anomalies in the field that occur in association with a one standard deviation anomaly in the time series and have the units of the anomaly field itself.

2.4 Description of shallow-water wave equation model runs

On a few occasions we made use of a one-layer, shallow water wave equation model built and generously provided to us by Professor James R. Holton. The model computes the nonlinear damped stationary equatorial wave response to a specified isolated heat source. The domain is an equatorial β-plane channel periodic in x and the method is based on finite differences in time and space. It is important to note that the model does not include a realistic mean flow, which has important implications for the representation and the degree of equatorial symmetry of the modeled circulation (Kraucunas, 2005).

For a flow of equivalent depth h_e and shallow water wave speed $c_B = \sqrt{gh_e}$, the nonlinear shallow water equations are given by:

$$\frac{\partial u}{\partial t} + u\frac{\partial u}{\partial x} + v\frac{\partial u}{\partial y} - \beta yv + \frac{\partial \Phi}{\partial x} = -\alpha u \tag{2.5}$$

$$\frac{\partial v}{\partial t} + u\frac{\partial v}{\partial x} + v\frac{\partial v}{\partial y} + \beta yu + \frac{\partial \Phi}{\partial y} = -\alpha v \tag{2.6}$$

$$\frac{\partial \Phi}{\partial t} + u\frac{\partial \Phi}{\partial x} + v\frac{\partial \Phi}{\partial y} + c_B^2\left(\frac{\partial u}{\partial x} + \frac{\partial v}{\partial y}\right) = -\alpha\Phi + Q \tag{2.7}$$

where u, v are the horizontal wind components, Φ the geopotential height, $\beta = df/dy$ the planetary vorticity gradient, α the damping rate (day^{-1}) and Q the thermal forcing. The heat source is of the form $Q = A(t)\exp\{-(x/L_x)^2 - [(y-y_0)/L_y]^2\}$, where L_x, L_y are the length and width of the channel and $A(t) = A_o[1-\exp(-t/\tau)]$ is the amplitude of the forcing. The thermal forcing is modified to give zero mean over the whole domain: $Q^* = Q - [Q]_{domain}$. Steady solutions are found by integrating in time from a state of rest.

3. Seasonality of the Hadley circulation

3.1 Introduction

At low latitudes the solar radiation absorbed exceeds the outgoing terrestrial radiation while at middle and high latitudes the Earth radiates more energy into space than it receives from the sun. The surface tropical air is being warmed and lifted up creating a band of low air pressure referred to as the Intertropical Convergence Zone (ITCZ) that draws in surface air from the subtropics (Figure 3.1). Mass conservation requires that the large amounts of rising air in this convection zone move poleward at upper levels, transporting heat away from the equator in both hemispheres, hence acting to partly restore the energy balance of the planet (the ocean is responsible for the remainder of the heat transport).

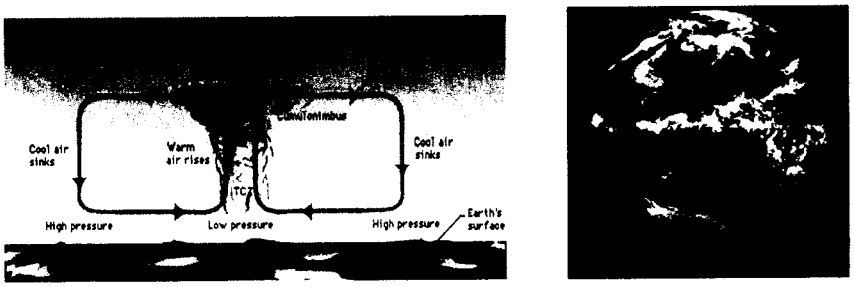

Figure 3.1: The ITCZ: (a) meridional view (www.zeilen.com/publish/article_1688.shtml); (b) satellite view (NOAA, www.ccrc.sr.unh.edu/~stm/AS/Weather_Toolbox/NE_Weather_Primer.html)

The mean meridional circulation (MMC) envisioned by Hadley (1735) and other authors cited in Lorenz's (1967) historical review, consists of a pair of equator-to-pole, thermally direct cells, one in each hemisphere, symmetric about the equator (Figure 3.2a). Such a one-cell model would be valid if one assumes that earth does not rotate (no

Coriolis force), is uniformly covered with water (no differential heating between land and ocean), and the sun is over the equator during all times of the year.

In the earth's atmosphere the mean meridional circulation consists of two directly driven Hadley-type cells at low latitudes (~equator-30°), indirect Ferrel cells at midlatitudes (~30-60°) and direct Polar cells at high latitudes (~60°-poles) (Figure 3.2b). Hence, the "Hadley cell" appellation continues to be used for the tropical, annual mean MMC dominated by the year-round rising motion over the equatorial belt and sinking motion over the subtropics (AMS Glossary of Meteorology - Glickman, 2000), but the same term is also widely used to denote the seasonally varying tropical MMC (e.g. Lindzen and Hou, 1988).

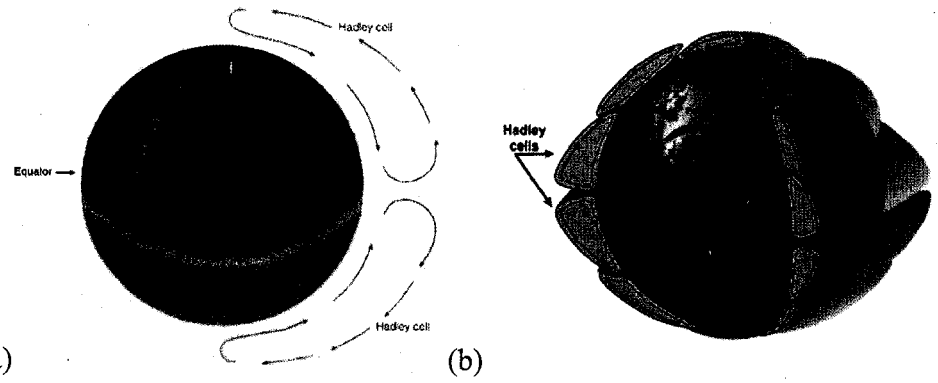

Figure 3.2: (a) The circulation envisaged by George Hadley (1685-1768) comprising of one giant meridional cell stretching from equator to pole (C. D. Ahrens, 1994, "Meteorology Today"), (b) present view of the Earth's general circulation, with three meridional cells in each hemisphere (NASA's Earth Observatory: http://earthobservatory.nasa.gov//Newsroom/NasaNews/2002/200201317366.html)

Analysis of global radiosonde observations (e.g. Oort and Rasmusson, 1970), Oort and Yienger, 1996), have documented the seasonally varying distribution of MMC. Throughout much of the year the MMC is dominated by a cross-equatorial cell with low-level flow from the winter Tropics into the summer Tropics, and an upper tropospheric

flow in the reverse sense. This general scheme is confirmed in the 1979–2001 NCEP–NCAR reanalysis shown in Figure 3.3. Here, as in many previous analyses, the MMC is described using the Stokes streamfunction ψ. Oort and Yienger (1996) obtained similar patterns in an analysis of the MMC based on radiosonde data. The maximum values of ψ at the times of the solstices were slightly stronger in their analysis (20 versus 14–16 $\times 10^{10}$ kg s^{-1}), and the Southern Hemisphere cell was slightly more strongly emphasized relative to the Northern Hemisphere cell.

Lindzen and Hou (1988, hereafter LH) drew attention to the cross-equatorial cell, characterizing it as a "solsticial pattern," as opposed to the classical, equatorially symmetric "equinoctial pattern." Based on their visual inspection of the 1958–63 meridional cross sections in Oort and Rasmusson (1970), they remarked that "the meridional circulation is almost always in a solsticial pattern; the idealized equinoctial pattern is almost never realized." Their theoretical analysis suggested that the distribution of MMC is highly sensitive to small equatorial asymmetries in the imposed temperature of the underlying surface: so much so that the displacement of the thermal equator from the geodetic equator by even a few degrees of latitude would give rise to a solsticial (or equatorially asymmetric) circulation as strong or stronger than the classical, equatorially symmetric "Hadley cell." Mindful of this sensitivity, they predicted that the solsticial component would dominate the tropical MMC throughout most of the year and that its amplitude would exhibit more of a "square wave" than a sinusoidal dependence on Julian day.

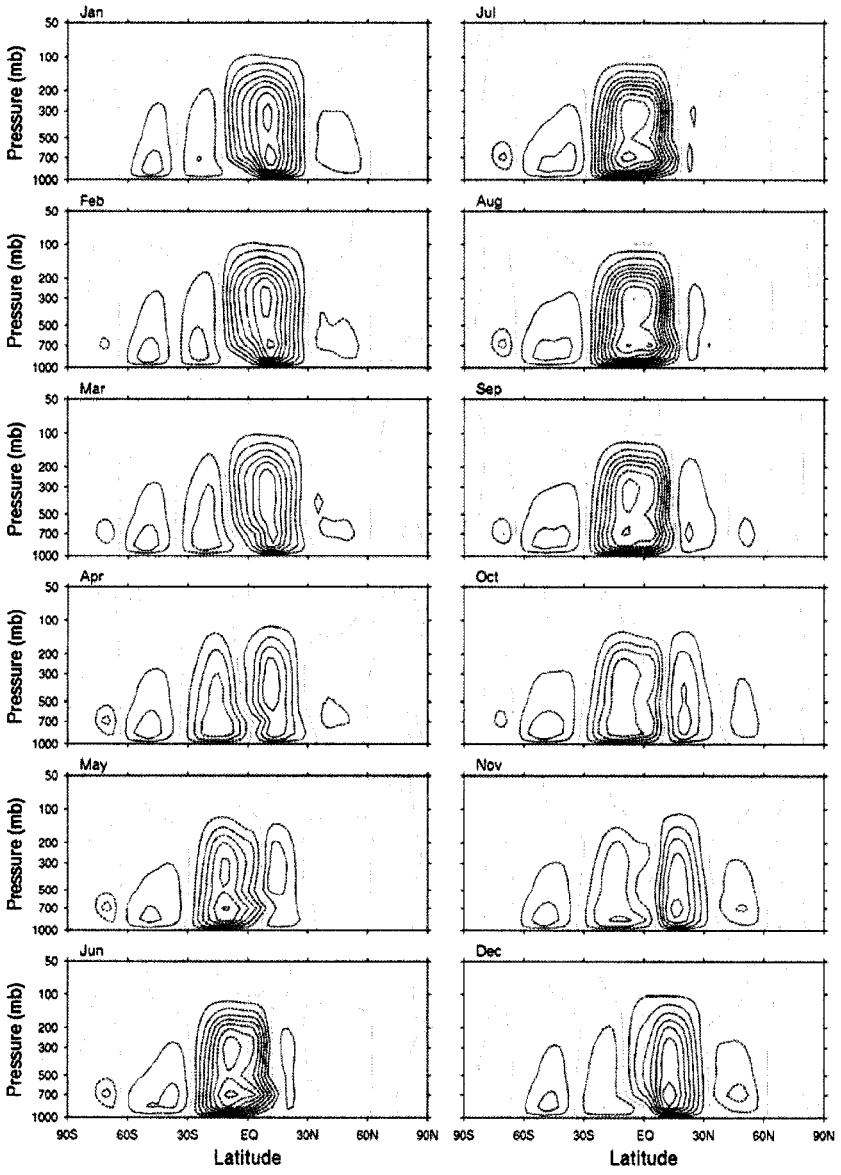

Figure 3.3: Monthly variation of the climatological-mean streamfunction in the NCEP reanalysis. Contour interval: 2×10^{10} kg s^{-1}. Red contours are positive, blue contours are negative, and the zero contour is gray. Cells surrounding positive centers are characterized by clockwise circulations and vice versa.

Fang and Tung (1999) extended the analysis in LH to a time-dependent model and found that the seasonal transitions were not as abrupt as LH had predicted. Nonetheless, the notion that the solsticial cell might be driven primarily by rather modest

displacements of the thermal equator has persisted as an alternative to the traditional view that it is largely a reflection of the regionally concentrated monsoon circulations (Newell et al. 1972; Das 1986).

Here we analyze the MMC in the NCEP-NCAR reanalyses with emphasis on the relative importance and seasonal progression of the solsticial component and the residual derived by subtracting the solsticial component from the total field.

3.2 Results

Figure 3.4 shows a histogram of the difference in the intensities of the northern and southern cells, as given by the average of their extrema in the streamfunction at the 300hPa level, based on 19 years of 5-day-mean data (1979–97). When the circulation is equatorially symmetric, the northern and southern cells are of comparable strength, but of opposing sign, yielding an average close to zero; when the northern cell dominates, the average is positive, and when the southern cell dominates, it is negative. The frequency distribution is bimodal with a minimum near the equator, but the minimum is not as pronounced as it would be if the MMC were dominated by a solsticial cell, whose annual march had the shape of a square wave.

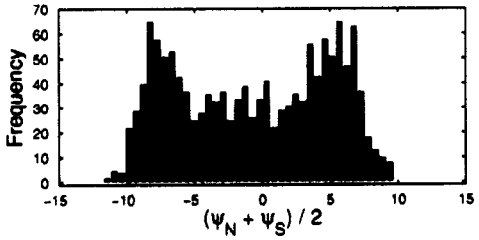

Figure 3.4: Histogram showing the difference in strength between the northern and southern tropical circulation cells in 19 years of 5-day mean data. Units: 10^{10} kg s^{-1}.

The annual-mean streamfunction, shown in Figure 3.5, is dominated by the equatorially symmetric component, with ascent in the tropical belt and subsidence in the subtropics. Upon close inspection it is evident that the axis of symmetry is not precisely on the equator, but a few degrees to the north of it, and that there is a particularly strong meridional gradient of the streamfunction across 7°N, which corresponds to the mean latitude of the intertropical convergence zone over the Pacific and Atlantic sectors.

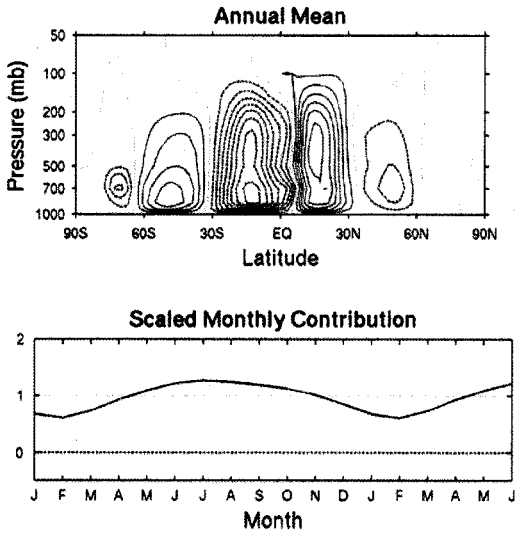

Figure 3.5: Annual mean streamfunction field (upper panel) based on the NCEP–NCAR reanalysis (contour interval 10^{10} kg s^{-1}; color contouring convention the same as in Fig. 3.3). The scaled monthly contribution of the MMC to the annual mean (lower panel). The time series was obtained by projecting the monthly mean climatological MMC onto the annual mean pattern; then the time series was scaled so that its time mean equals 1.

The region of ascent in between the two cells corresponds closely to the band of heavy near-equatorial rainfall, as illustrated in the upper panels of Figure 3.6. Subsidence is dominant in the subtropics around 30° in both hemispheres, at the interfaces between the tropical Hadley cells and the extratropical Ferrel cells. Within the tropics the southern cell is slightly stronger than the northern cell. The lower panel of Figure 3.5 shows the

scaled monthly contribution of the climatological MMC to the annual mean pattern (represented in the top panel). The associated time series exhibits only small annual variations about the time mean, thus indicating that the pattern describing the annual mean MMC is present during all months of the year, with only minor variations in amplitude from month to month.

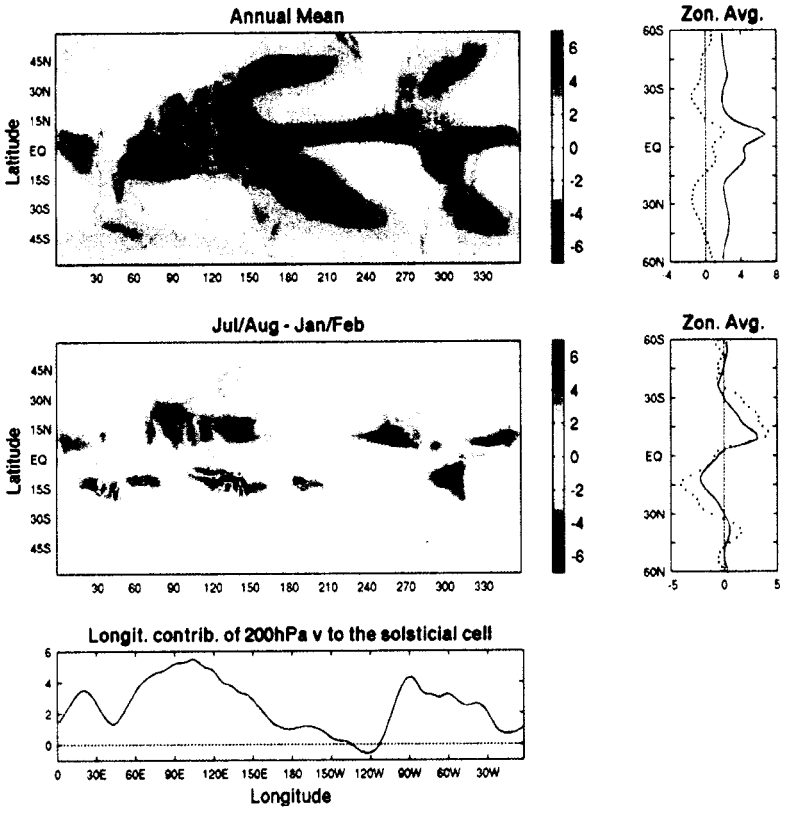

Figure 3.6: Annual-mean and solsticial components of the precipitation field (upper left two panels) and longitudinal contribution of the 15°N–15°S 200hPa meridional wind to the meridional wind associated with the solsticial cell (bottom panel). Precipitation is expressed in mm day^{-1}. The seasonally varying component is approximated as half the difference between the Jul/Aug and Jan/Feb mean fields. The panels on the right show the zonally averaged values (solid). Also shown in the right-hand panels are the 500hPa vertical velocity profiles (units: cm s^{-1}; dotted), rescaled by multiplying them by a factor of 6 to make their profiles more clearly visible in the figure.

In order to document the variability about the time mean we performed an EOF analysis upon the monthly mean climatological ψ field (1979–2001). Figure 3.7 shows

leading standardized principal component (PC) time series and the corresponding regression pattern for ψ.

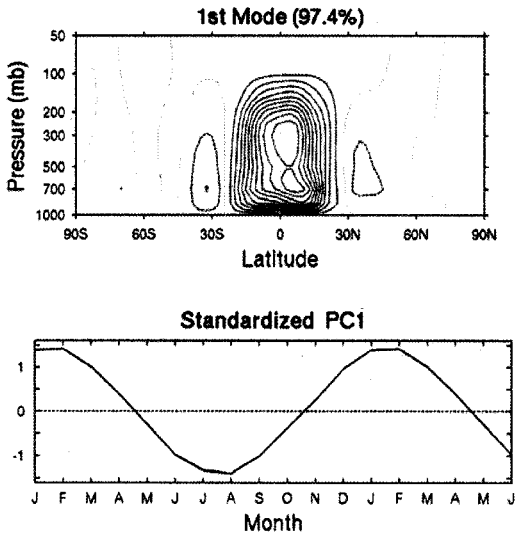

Figure 3.7: Upper panel: The streamfunction field regressed upon the leading principal component of the departure of the climatological-mean streamfunction from its annual mean (contour interval 10^{10} kg s^{-1}; color contouring convention the same as in Fig. 3.3). Lower panel: The corresponding standardized principal component.

This mode accounts for almost all (97.4%) the variance of the climatological-mean streamfunction about the annual mean. It is almost perfectly equatorially asymmetric and seasonally reversing, with extrema in January–February and July–August. Its seasonal variation is sinusoidal, with no indication of square wave behavior.

3.3 Discussion

The residual-MMC, obtained by subtracting the solsticial mode from the monthly streamfunction field, is dominated by the annual mean (Figure 3.8). This was expected since (1) the annual mean accounts for an appreciable fraction of the mean squared

amplitude of the MMC (41%) and (2) the solsticial mode accounts for nearly all the seasonal variability about the annual mean (97.4%). Hence, the classical, nearly equatorially symmetric "Hadley cell" is not an ephemeral equinoctial feature of the general circulation, as envisioned in LH; it is robust and present year round.

This seasonally reversing solsticial mode and the annual mean together account for 98.6% of the mean squared amplitude of the climatological-mean ψ field. The seasonally reversing mode explains somewhat more of the mean-squared amplitude of the ψ field than the annual mean but, owing to its smaller meridional scale, the annual mean explains slightly more of the mean squared amplitude of the vertical mass flux. Qualitatively similar results are obtained when the MMC is formally decomposed into equatorially symmetric and asymmetric components (not shown). Thus, the mean and seasonally reversing (or alternatively, the equatorially symmetric and asymmetric) components of the seasonally varying MMC can be considered to be of roughly comparable importance.

In agreement with prior results of Newell et al. (1972) and Schulman (1973), we find a close correspondence between the vertical mass flux in the seasonally reversing cell and the belts of monsoon rainfall over the tropical continents (Figure 3.6, the panels on the right). The associated cross-equatorial mass fluxes in the upper and lower branches of the cell reach peak values in excess of 1.75×10^{11} kg s^{-1} and are each sufficient to transfer roughly half of the mass of an entire hemisphere across the equator over the course of the monsoon season.

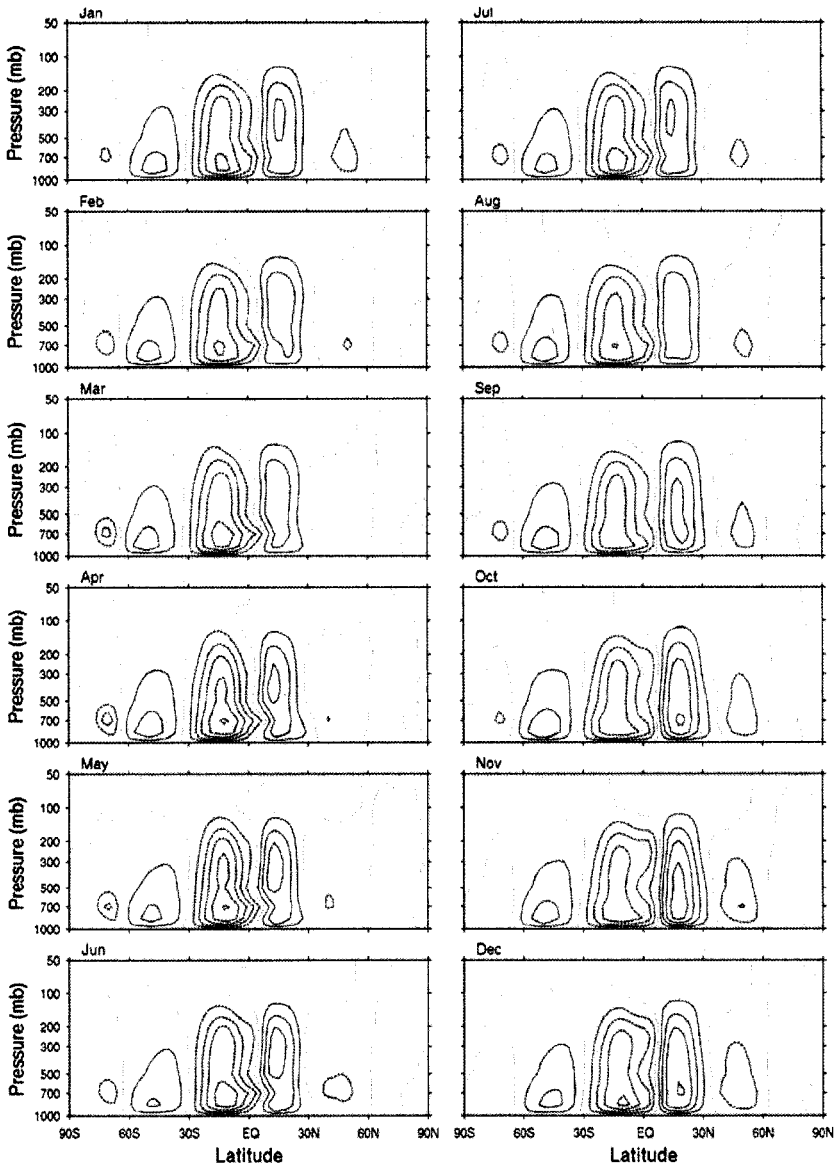

Figure 3.8: Monthly mean residual MMC derived by removing the seasonally reversing component associated with the EOF1. Contour interval: 2×10^{10} kg s^{-1}; color contouring convention the same as in Fig. 3.3)

The peaks in the seasonally reversing "solsticial cell," which are actually observed 6 weeks after the dates of the solstices, correspond closely to the peaks of the monsoon seasons. That the contribution to the solsticial cell (EOF1) comes primarily from the

monsoonal regions is also apparent in the lower left panel of Figure 3.6 in which the 200hPa meridional wind is used to represent the longitudinal contribution of the monthly mean climatological field to the solsticial cell. The maximum contributions come from the continental/monsoonal regions while the minimum contributions come from the "pure" oceanic regions (central Pacific). The timing, together with the strong correspondence between the meridional structure of EOF1 of MMC and the belts of seasonally varying rainfall (Figure 3.6), supports the view that the seasonally reversing solsticial cell is closely associated with the monsoons.

In recent work, Walker and Schneider (2005) have performed additional model simulations of the structure and behaviour of the observed mean meridional circulation. In conflict with LH's simulations but consistent with our findings, they concluded that an annually averaged axisymmetric Hadley circulation is very close to the circulation forced by an annually averaged heating. They attributed the discrepancies between their model results and those of LH to the rigid lid used in LH's model, which induces a spurious nonlinear amplification of the Hadley circulation.

4. Zonal momentum balance of the tropical troposphere

4.1 Introduction

The angular momentum balance of the atmosphere is dominated by the poleward flux of westerly momentum associated with high-frequency baroclinic waves and low-frequency quasi-stationary eddy circulations in the subtropical and midlatitude upper troposphere (Starr, 1948; Peixoto and Oort, 1992). However, at low latitudes the eddy momentum flux is directed towards the equator (Starr et al., 1970; Rosen and Salstein, 1980), which implies an equatorial source of wave activity and a convergence of westerly momentum in the equatorial belt. Since easterly winds are prevalent in the equatorial region, some other aspect of the tropical circulation must provide a mean easterly acceleration in order to balance the convergence of eddy momentum fluxes.

Lindzen and Hou (1988) noted that the mean meridional circulation (MMC) on Earth almost always exhibits some amount of equatorial asymmetry, and found that the equatorward transport of low angular momentum air by a Hadley cell straddling the equator produces a strong easterly acceleration over the equator in an axisymmetric model. Lee (1999) showed that the seasonal cycle of the MMC at 200hPa induces a momentum flux divergence in the equatorial belt that offsets the momentum flux convergence associated with the eddies. Also Kraucunas and Hartmann (2004) (hereafter KH) demonstrated that eddy forcing at low latitudes in an idealized GCM leads to persistent equatorial superrotation under equatorially symmetric boundary conditions, but

not under solstitial boundary conditions. These results imply that the equatorial asymmetry of the MMC is crucial for maintaining the deep easterly flow at the equator in the presence of the westerly acceleration induced by tropical eddies.

In this chapter, we analyze the tropical angular momentum balance in further detail, making use of the NCEP reanalyses at all available levels. We consider the zonally averaged flow, as in previous analyses of Lindzen and Hou (1988), Lee (1999), Kraucunas and Hartmann (2004). However, in contrast to those studies, we also consider the horizontal structure of stationary waves in the equatorial waveguide that are responsible for most of the forcing. We also investigate the degree of hemispheric symmetry of the equatorial stationary waves as a function of season and relate this to the solutions of a simple nonlinear shallow water wave equation model.

4.2 Decomposition of the zonal momentum balance

Here we summarize the diagnostics used to separate the contributions of various kinds of motion to the zonal momentum balance. The zonal wind for a particular location and day may be written $u_d = u_{an} + u_c' + u' + u_d'$ where the subscript "*d*" indicates an individual daily value, "*an*" indicates the long-term annual mean, "*c*" indicates a climatological (23-year) pentad-mean value, and variables without subscripts indicate means for individual pentads; $u_c' = u_c - u_{an}$ represents the deviation from the annual-mean associated with the climatological seasonal cycle, $u' = u - u_c$ indicates low-frequency non-seasonal (i.e. interannual and intra-annual) variability, and $u_d' = u_d - u$

reflects high-frequency (intra-pentad) variability. This temporal separation of the terms allows for a clearer definition of the relative importance of eddies with different time scales in the equatorial momentum budget.

The angular momentum balance is diagnosed using the zonally averaged zonal wind equation in the advective form, which may be written:

$$\frac{\partial[u]}{\partial t} \cong [v]\left(f - \frac{1}{\cos\phi}\frac{\partial[u]\cos\phi}{\partial y}\right) - [\omega]\frac{\partial[u]}{\partial p} - \frac{1}{\cos^2\phi}\frac{\partial[u^*v^*]\cos^2\phi}{\partial y} - \frac{\partial[u^*\omega^*]}{\partial p} - [F_x] \quad (4.1)$$

For seasonal or annual averages, the zonal wind tendency is negligible and the individual terms on the RHS of (4.1) are simply averaged over all years and over the indicated seasons. In this expression the first term on the right hand side may be recognized as being equivalent to $[v](f+[\zeta])$ where $[\zeta]$ is the relative vorticity and $(f+[\zeta])$ the absolute vorticity of the zonally symmetric component of the flow.

We also make use of the following temporal decomposition:

$$[u^*v^*]_{an} = [u^*_{an}v^*_{an}] + [u^{'*}_c v^{'*}_c]_{an} + [u^{'*}v^{'*}]_{an} + [u^{'}_d v^{'}_d]_{an} \quad (4.2)$$

Here $[u^*_{an}v^*_{an}]$ indicates the momentum flux associated with the long-term (23-year) annual-mean stationary waves, $[u^{'*}_c v^{'*}_c]_{an}$ denotes the annual-mean flux of momentum by the climatological seasonally varying stationary waves, $[u^{'*}v^{'*}]_{an}$ represents the contribution from interannual and intra-annual transient eddies, and $[u^{'}_d v^{'}_d]_{an}$ denotes the momentum flux by the high-frequency transients. This latter term includes a small contribution from the intra-pentad correlation between the zonally-averaged zonal and

meridional wind components ($[u]_d^{'}[v]_d^{'}$), but this distinction will be ignored since the intra-pentad momentum fluxes are found to be small in the tropics.

The long-term annual-mean advection of zonal momentum by the MMC (i.e. the 23-year annual mean of the first term on the RHS of (4.1) may also be temporally decomposed in the form:

$$\left([v]\left(f-\frac{1}{\cos\phi}\frac{\partial[u]\cos\phi}{\partial y}\right)\right)_{an} \cong ([v]_c)_{an}\left(f-\frac{1}{\cos\phi}\frac{\partial[u]_c\cos\phi}{\partial y}\right)_{an} + \left([v]_c^{'}\left(f-\frac{1}{\cos\phi}\frac{\partial[u]_c\cos\phi}{\partial y}\right)^{'}\right)_{an} \quad (4.3)$$

(I) (II)

Term (I) represents the advection of zonal momentum associated with the long-term annual-mean meridional wind acting on the long-term mean shear, while term (II), which we will subsequently refer to as the "seasonally-varying MMC advection," reflects the temporal correlations between $[v]_c$ and $\partial[u]_c/\partial y$ over the course of the year. This term is somewhat different from the transient MMC momentum term calculated by Lee (1999), who based her analysis on the mean zonal wind equation in flux form. The cross-correlations between $[v]$ and $\partial[u]/\partial y$ on other time scales were evaluated and found to be 2-3 orders of magnitude smaller than the leading terms, so they are neglected in (4.3).

4.3 Annual mean zonal momentum balance

Figure 4.1 shows the long-term annual-mean zonally averaged zonal wind and MMC. The dominant features in the zonal wind field (Figure 4.1a) are the midlatitude westerly jets. Easterlies prevail in the tropics, with low-level maxima in the tradewind belts and an isolated maximum in the upper troposphere centered a few degrees north of

the equator. The long-term annual-mean MMC (Figure 4.1b) is dominated by a pair of Hadley cells straddling a belt of ascent centered at ~5°N, the mean latitude of the ITCZ.

The southern cell is wider and ~25% stronger than the northern cell, with cross-equatorial flow evident at both upper and lower levels.

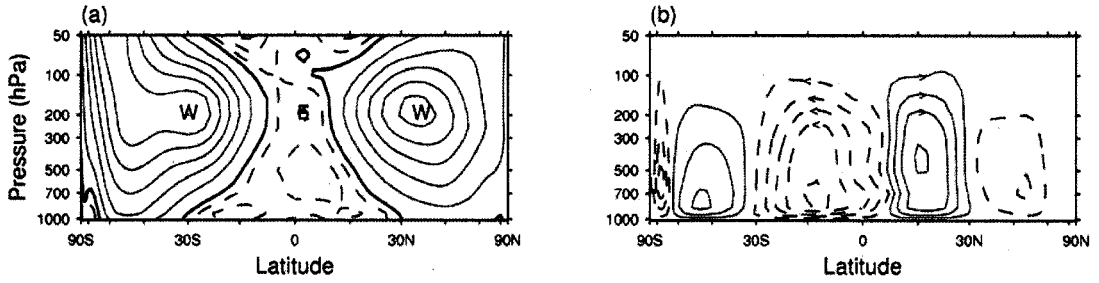

Figure 4.1: Vertical cross-sections of annual-mean (a) zonal wind $[u]_{an}$ and (b) MMC $[\psi]_{an}$. Solid red contours are positive, dashed blue contours are negative and the zero line for $[u]_{an}$ is thickened and black. For the zonal wind, the contour interval is 5 for positive values and 2 for negative values (..-4, -2, 0, 5, 10,..) (m s^{-1}). For the MMC the contour interval is 2 (..-3, -1, 1,..) x 10^{10} kg s^{-1}. Distance along the x-axis is represented as sin of latitude.

Figure 4.2 shows the long-term annual-mean meridional and vertical fluxes of westerly momentum by the eddies. Sandwiched between the belts of poleward fluxes in midlatitudes are weaker equatorward fluxes with maxima centered near 10°S and 10°N at the 150hPa level (Figure 4.2a). The northward fluxes are somewhat stronger than their Northern Hemisphere counterparts, and (like the MMC in Figure 4.1b) extend slightly across the equator. The vertical transport of momentum by the eddies (Figure 4.2b) is downward in the tropical upper troposphere, and strongest directly below the maximum meridional flux convergence. In contrast to the results of the numerical simulations carried out by KH, we find that the vertical fluxes in the NCEP reanalyses play only a minor role in the angular momentum balance and thus we neglect them in our analysis. A

complete amplitude and error analysis of all momentum budget terms and their residual is included in Appendix B.

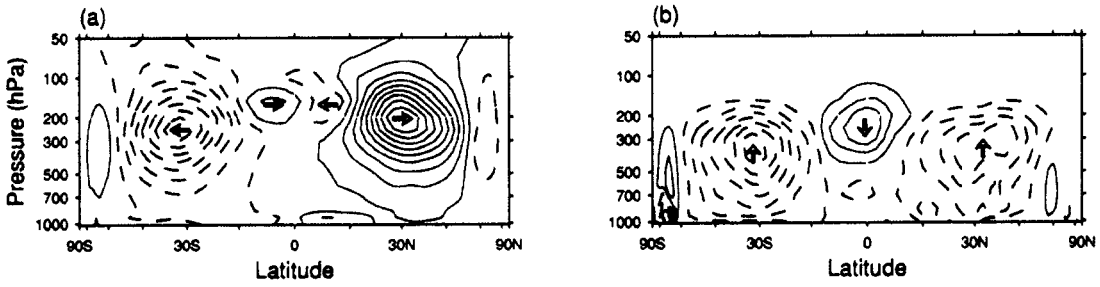

Figure 4.2: Vertical cross-sections of total annual mean (a) meridional $[u^* v^*]_{an} \cos\phi$ and (b) vertical $[u^* \omega^*]_{an} \cos\phi$ eddy momentum fluxes. The color contouring convention is the same as in Fig. 4.1. For the meridional fluxes the contour interval is 5 (..-7.5, -2.5, 2.5,..) $m^2 s^{-2}$ and for the vertical fluxes is 3 (..-4.5, -1.5, 1.5,..) x 10^{-2} m x Pa s^{-2}. A horizontal dashed line at 200hPa has been drawn for reference. Distance along the x-axis is represented as sin of latitude.

To document the contributions from eddies at different time scales to the momentum fluxes in Figure 4.2a, the annual-mean meridional transport of angular momentum by eddies was decomposed into the components defined in eq. 4.2. Figure 4.3 shows cross-sections of these four components. In the extratropics eddies at all four time scales contribute to the poleward eddy momentum flux, consistent with results of Peixoto and Oort (1992). In contrast, within the tropical belt the equatorward eddy momentum transport is dominated by the stationary wave contribution (Figure 4.3a), while the seasonally varying component (Figure 4.3b) and the nonseasonal term resolved by pentad data (Figure 4.3c) make secondary contributions. Lee (1999) obtained similar results, although her analysis focused on the characteristics of the inter- and intra-annual eddies in the frequency domain and did not emphasize the singular importance of the standing eddies in the zonal momentum balance.

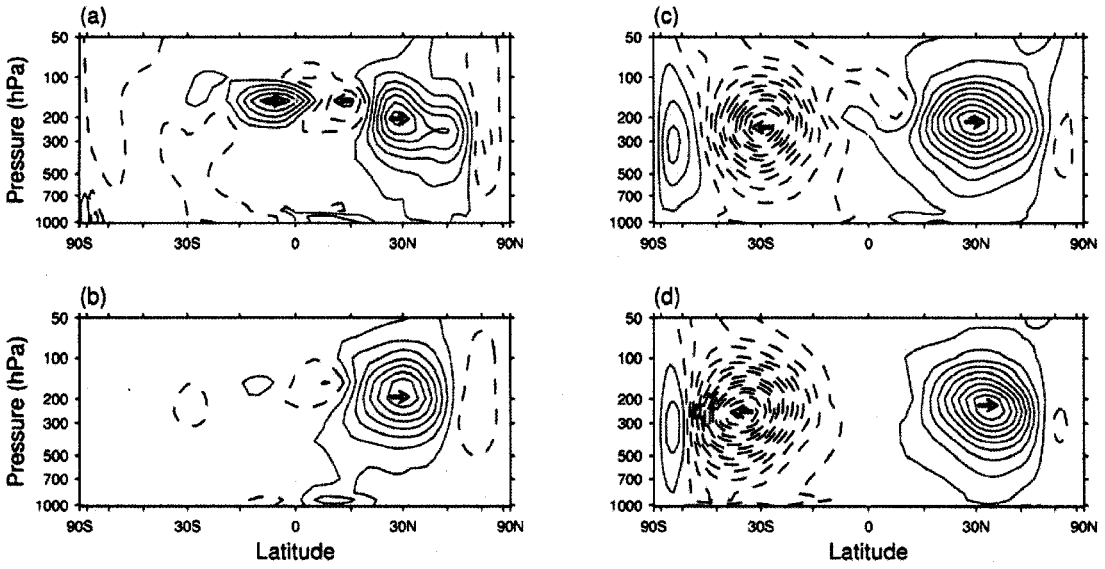

Figure 4.3: Vertical cross-sections of annual-mean components of the meridional eddy momentum flux: (a) annual-mean stationary waves $[u^*_{an}v^*_{an}]\cos\phi$, (b) seasonally varying component of the climatological mean stationary waves $[u'^*_c v'^*_c]_{an}\cos\phi$, (c) nonseasonal transient eddies resolved by pentad-mean data $[u'^* v'^*]_{an}\cos\phi$ and (d) high frequency transients within individual pentads $[u'^*_d v'^*_d]_{an}\cos\phi$. The color contouring convention is the same as in Fig. 4.1. Contour interval: 1.5 (..-2.25, -0.75, 0.75,..) $m^2\ s^{-2}$. Distance along the *x*-axis is represented as sin of latitude.

Figure 4.4 shows the annual-mean 150hPa geopotential height and horizontal wind fields superimposed on the annual-mean precipitation field, which may be viewed as a proxy for tropical diabatic heating. It is interesting to note that the main features observed in the NCEP data tend to be reproduced in theoretical representations of the response of the circulation to the tropical distribution of heating. The flow pattern over the western Pacific and Indian oceans resembles the linear planetary wave response to an isolated equatorial mass source (Matsuno, 1966) or a mid-tropospheric heat source (Gill, 1980) on an equatorial β-plane. The pattern is characterized by an equatorial Kelvin wave to the east of the maximum latent heating and a pair of anticyclonic Rossby gyres at, and to the

west of, the eddy forcing. These features bear an even stronger qualitative resemblance to the nonlinear solutions to the shallow water wave equation (see, e.g., Van Tuyl, 1986, for the full set of these equations) forced by an isolated heat source on the equator (Figure 4.5).

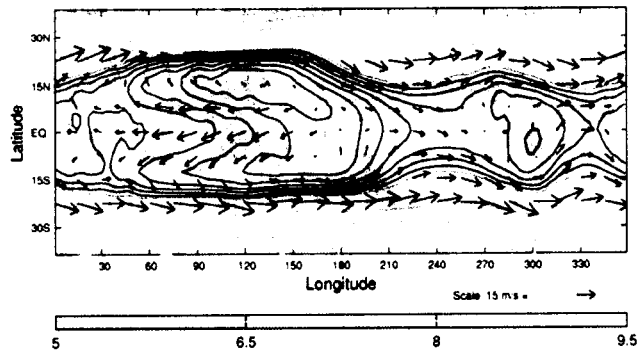

Figure 4.4: 150hPa annual-mean geopotential height (contours) and wind (arrows); superimposed (color) is the tropical annual-mean precipitation (mm day^{-1}). Contour interval for the geopotential height: 100 m (gray lines); additional contours (black) at 10 m are inserted in the tropical belt. Contour succession: (..14100, 14200, 14210, 14220,..) m, with the first black contour at the separation between gray and black contours representing the 14210 m line. The wind arrows are plotted only up to 23° in both hemispheres.

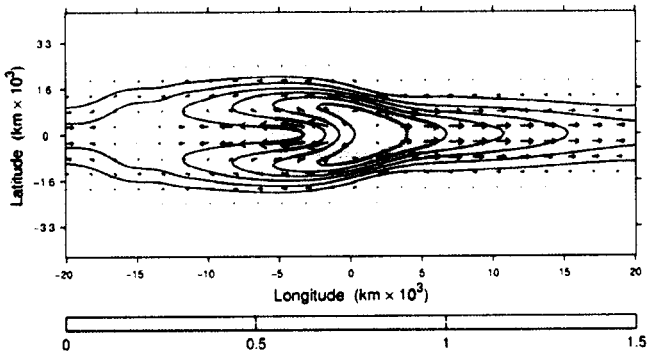

Figure 4.5: Figure 1.8 repeated - Nonlinear solution of the shallow water wave equation forced by an equatorial heat source. The geopotential height field is contoured, the wind field is represented by arrows and the heat source is shown in color.

Note that the meridional extent of the modeled flow is smaller than that found in the observations. Also the westerly (easterly) winds in the equatorial belt to the east (west) of the heat source are stronger (weaker) than the observed. These differences are attributable

to the absence of a zonal mean flow in our model simulation. When a fairly realistic basic state is included in the model, these differences are much reduced (Kraucunas, 2005).

The observed (Figure 4.4) and, to a lesser extent, the modeled (Figure 4.5) wind vectors near the equator both exhibit a predominantly northwest-southeast tilt in the Northern Hemisphere and a northeast-southwest tilt in the Southern Hemisphere, with diffluent easterly flow to the west of the heat source and confluent westerly flow to the east of the heat source. This tilt is responsible for the equatorward eddy flux of westerly momentum noted in Figure 4.2a and Figure 4.3a.

The leading terms in the annual-mean zonal momentum balance (eq. 4.1) are shown in Figure 4.6. In the free troposphere there exists a strong compensation between the MMC term (Figure 4.6a) and the eddy momentum flux convergence (Figure 4.6b). The contribution from the vertical eddy flux and mean vertical advection (not shown) are at least an order of magnitude or more smaller than the leading terms; including these terms does not significantly alter the appearance of the residual in Figure 4.6c (see Appendix B for a detailed amplitude comparison of all terms in the momentum budget). The most significant imbalances (Figure 4.6c) occur outside of the region of interest in this study: in the boreal stratosphere, where gravity wave drag during wintertime may be an important factor, and in the planetary boundary layer where frictional drag is one of the dominant terms in the momentum balance.

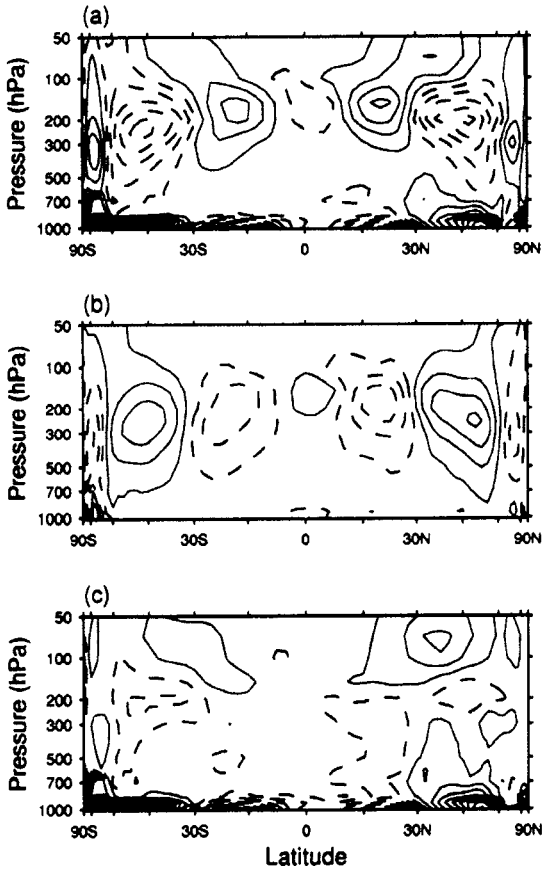

Figure 4.6: Vertical cross-sections of the leading terms in the annual-mean momentum budget: (a) MMC associated fluxes (term 1 on RHS of eq. 4.1), (b) eddy associated fluxes (term 3 on RHS of eq. 4.1), and (c) sum of the two contributions in (a) and (b). The color contouring convention is the same as in Fig. 4.1. Contour interval: 1 (..-1.5, -0.5, 0.5,..) x 10^{-5} m s^{-2}. Distance along the *x*-axis is represented as sin of latitude.

Figure 4.7 shows the annual-mean acceleration induced by the MMC (Figure 4.6a) decomposed into annual-mean and seasonally varying components, in accordance with eq. 4.3. The upper tropospheric advection of momentum by the annual-mean meridional winds (Figure 4.7a) induces a weak easterly acceleration near the equator by virtue of the small equatorial asymmetries in the annual-mean MMC and zonal mean zonal winds (Figure 4.1a and b), but this acceleration is clearly not sufficient to balance the annual-mean eddy momentum flux convergence over the equator (Figure 4.6b).

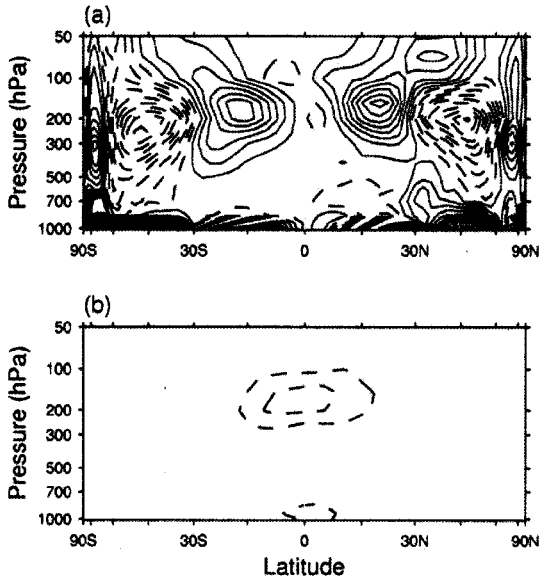

Figure 4.7: Vertical cross-sections of MMC momentum flux (eq. 4.3): (a) the product of annual means and (b) the annual-mean of the seasonal transient product. The color contouring convention is the same as in Fig. 4.1. Contour interval: 0.5 (..-0.75, -0.25, 0.25,..) x 10^{-5} m s^{-2} (half of that used in Figure 4.6a). Distance along the *x*-axis is represented as sin of latitude.

The seasonally varying MMC advection (Figure 4.7b), on the other hand, induces an easterly acceleration throughout the tropical upper troposphere by virtue of the strong positive temporal correlation between the climatological seasonally varying mean meridional wind ($[v]_c$) and the mean zonal wind gradient ($\partial[u]_c/\partial y$) over the course of the year. Note that the MMC component responsible for this equatorial easterly acceleration was represented in Chapter 3 as the leading EOF of the departure of the seasonally varying, climatological-mean streamfunction field from its annual mean (Figure 3.7). The relationship between $[v]_c$ and $\partial[u]_c/\partial y$ is examined in more detail below.

4.4 The monsoon and transition seasons

The zonally averaged zonal wind, MMC, and eddy momentum fluxes during the monsoon seasons January-February (JF) and July-August (JA) are shown in Figure 4.8. During both seasons, strong easterly flow is present in the tropical upper troposphere of the summer hemisphere (Figure 4.8 a and d). Also during those seasons the MMC is dominated by a single cell straddling the equator (Figure 4.8 b and e). In the upper troposphere over the equator, $-\partial[u]/\partial y$ is negative during JF and negative during JA, while $[v]$ is of opposing sign. Hence, the meridional advection of zonal momentum by the MMC induces strong easterly accelerations in the tropical upper troposphere during both monsoon seasons, and accounts for much of the seasonally varying advection of easterly momentum by the MMC in the annual-mean zonal momentum balance (Figure 4.7b).

The eddy momentum fluxes in the equatorial belt, previously pointed out by Newell et al. (1972) and Wallace (1983), are also much stronger during the monsoon seasons than in the annual-mean, and are offset from the equator by ~5° latitude into the winter hemisphere (Figure 4.8 c and f). The eddy momentum fluxes coincide with the strongest mean meridional winds aloft (indicated by the vertical gradient of ψ in Figure 4.8 b and e), and are in the opposite direction. An analogous relationship between $[v]$ and $[u^*v^*]$ is also apparent in Figs. 10-11 of Kraucunas and Hartmann, 2005.

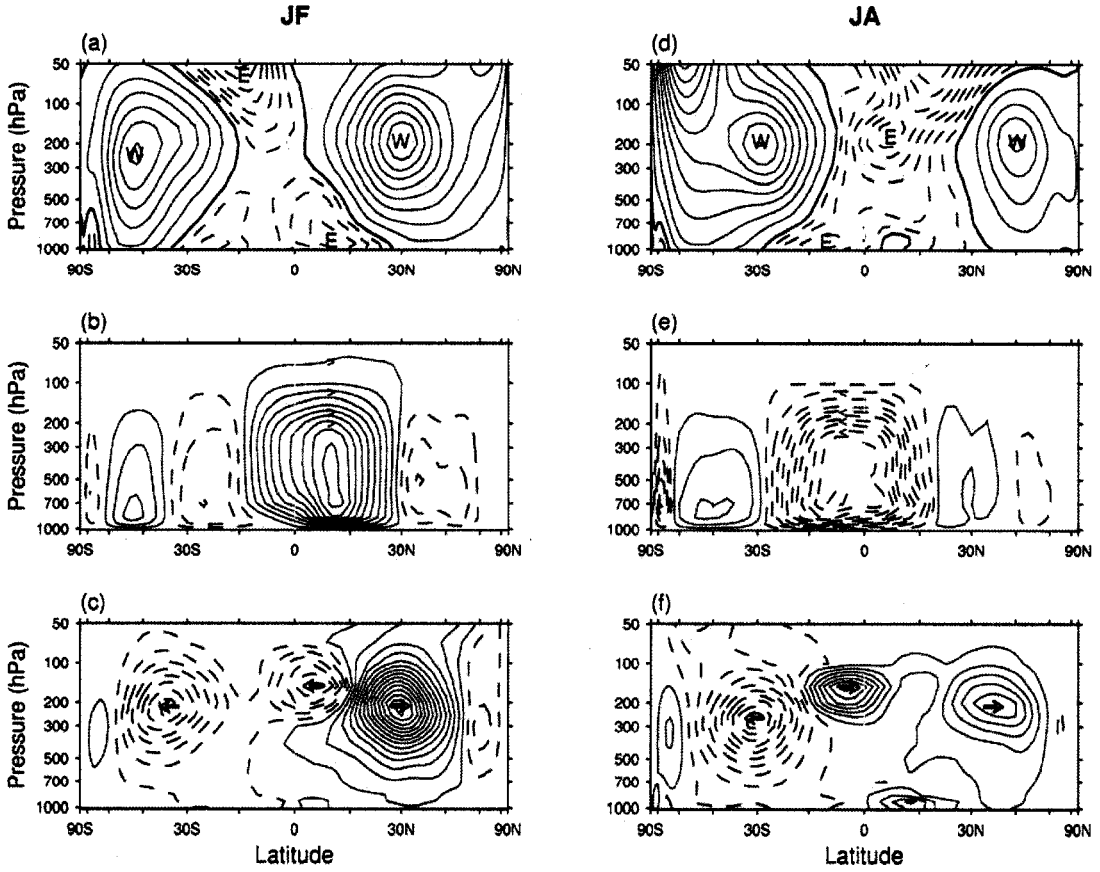

Figure 4.8: Vertical cross-sections of seasonal mean zonal wind, MMC and meridional eddy fluxes of zonal momentum. Panels (a,b,c) are for JF, (d,e,f) for JA. The color contouring convention is the same as in Fig. 4.1. For the zonal wind, the contour interval is 5 for the positive values and 2 for the negative values (m/s); the zero line is thickened. For the MMC the contour interval is 2 (..-3, -1, 1,..) x 10^{10} kg s^{-1}. For the eddy fluxes the contour interval is 5 (..-7.5, -2.5, 2.5,..) m^2 s^{-2}. Distance along the *x*-axis is represented as sin of latitude.

Figure 4.9 shows the climatological mean geopotential height and horizontal winds at the 150hPa level during JF and JA, along with the corresponding precipitation fields. As in the annual-mean patterns (Figure 4.4), the longitudinal variations over the maritime continent resemble the stationary wave response to an idealized mid-tropospheric heat source. The JF pattern in Figure 4.9 resembles the annual mean (Figure 4.4), with a slight enhancement of the Southern Hemisphere geopotential height features, while the JA

circulation is dominated by the Tibetan anticyclone associated with the Asian summer monsoon. Cross equatorial flow from the summer hemisphere into the winter hemisphere is clearly evident in the sectors dominated by the monsoon circulations. The easterly component of the air flowing across the equator gives rise to the eddy fluxes of westerly momentum from the winter hemisphere into the summer hemisphere in Figure 4.8c and f.

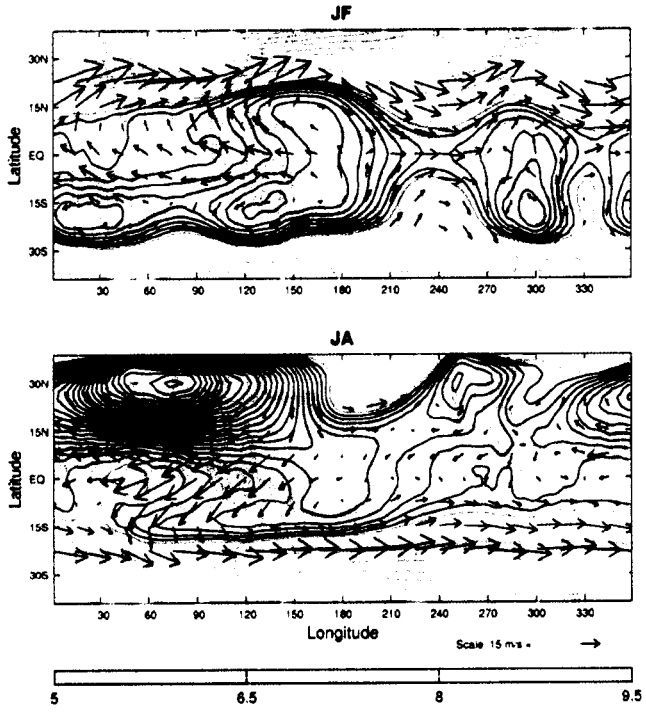

Figure 4.9: As in Figure 4.4 but for the JF and JA seasons.

Many of the features of the geopotential height and wind patterns in the tropics are qualitatively replicated in the nonlinear solution to the shallow water wave equation forced with a heat source centered ~8° off the equator, shown in Figure 4.10. As in the observations, the stationary wave pattern is most intense and most of the cross-equatorial flow takes place near and just to the west of the heating and the maximum values of geopotential height.

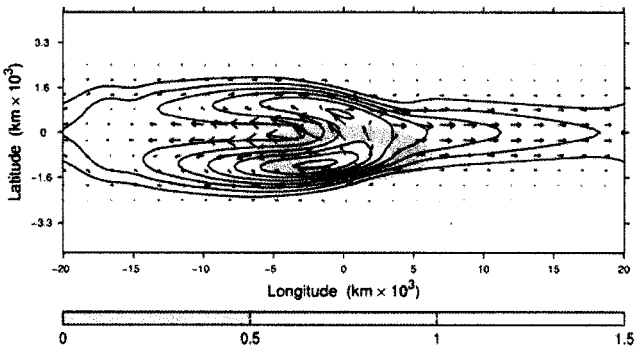

Figure 4.10: As in Figure 4.5 but for a heat source centered off the equator.

As in the annual-mean, the zonal momentum balance for the monsoon seasons (Figure 4.11) is marked by a cancellation between the easterly acceleration associated with the cross-equatorial flow in the upper branch of the MMC (Figure 4.11 a and c) and the westerly acceleration associated with the convergence of the eddy momentum fluxes in the equatorial belt (Figure 4.11 b and d). Both these terms are substantially stronger than the corresponding annual-mean fields shown in Figure 4.6. It is understandable that the MMC term should be stronger, but it is notable that the eddy momentum flux convergence is stronger as well.

Next we examine the mean circulation during the transition seasons, when the monsoons are relatively weak and the MMC is more equatorially symmetric. Figure 4.12 shows the mean zonal wind, MMC and eddy momentum fluxes during April-May (AM) and October-November (ON). The sections for AM exhibit a high degree of equatorial symmetry, with westerly jets centered at ~30° latitude in both hemispheres, very weak cross-equatorial flow, and virtually nonexistent eddy momentum fluxes in the deep tropics.

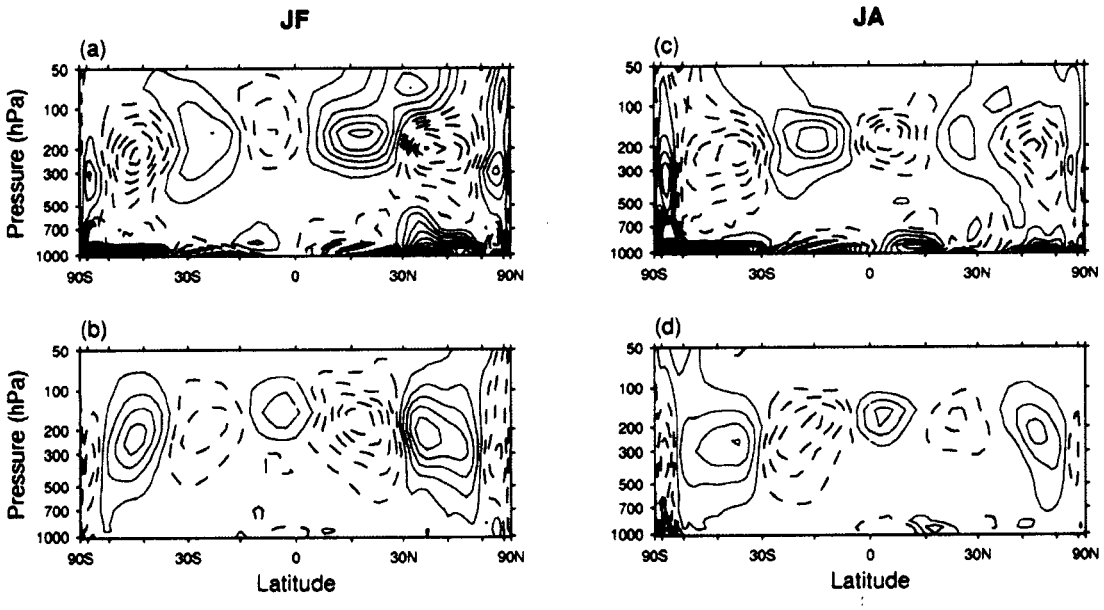

Figure 4.11: Vertical cross-sections of the leading terms in the seasonal mean momentum budget: (a,c) MMC associated fluxes, (b,d) eddy fluxes. Panels (a,b) are for JF and (c,d) for JA. The color contouring convention is the same as in Fig. 4.1. Contour interval: 1 (..-1.5, -0.5, 0.5,..) x 10^{-5} m s^{-2}. Distance along the x-axis is represented as sin of latitude.

In contrast to AM, the zonally-averaged circulation statistics for ON exhibit a substantial amount of equatorial asymmetry. In agreement with results of Fleming et al. (1987), the Northern Hemisphere westerly jet stream is shifted northward in ON relative to AM. Both the Ferrel cell and the Hadley cell are shifted northward relative to their AM positions in the Northern Hemisphere. The Southern Hemisphere MMC cell (Figure 4.12e) extends ~7° of latitude into the Northern Hemisphere, and the belt of easterly surface winds (Figure 4.12d) is also shifted north of the equator. The tropical eddy momentum fluxes (Figure 4.12f) are much stronger during ON than during AM and, as in the monsoon seasons, are directed opposite to upper level $[v]$.

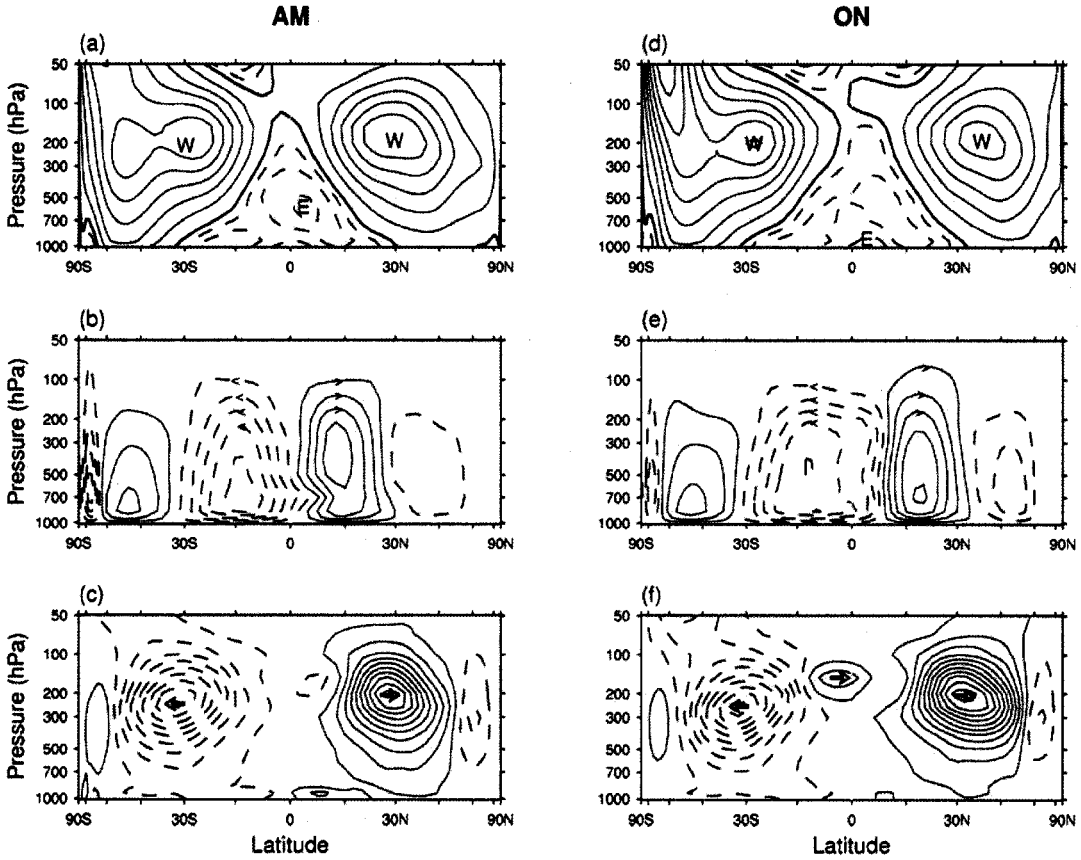

Figure 4.12: As in Figure 4.8 but for the AM and ON seasons.

The differences between the AM and ON zonal wind and MMC fields are shown in Figure 4.13. The westerly wind maximum at 15°N coincides with the region of subsidence at the poleward limit of the equatorial MMC. Analogous relationships are observed during all seasons and in the annual mean. Hence, the latitude of the jet stream appears to be consistent with the structure of the tropical MMC.

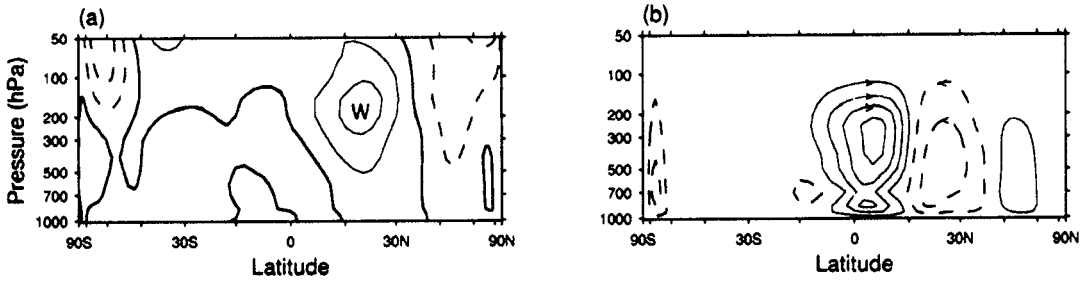

Figure 4.13: Seasonal differences AM-ON for zonal wind (a) and MMC (b). For the zonal wind the contour interval is 5 m s^{-1}; the zero line is thickened. For the MMC the contour interval is 2 (..-3, -1, 1,..) x 10^{10} kg s^{-1}. The color contouring convention is the same as in Fig. 4.1. Distance along the *x*-axis is represented as sin of latitude.

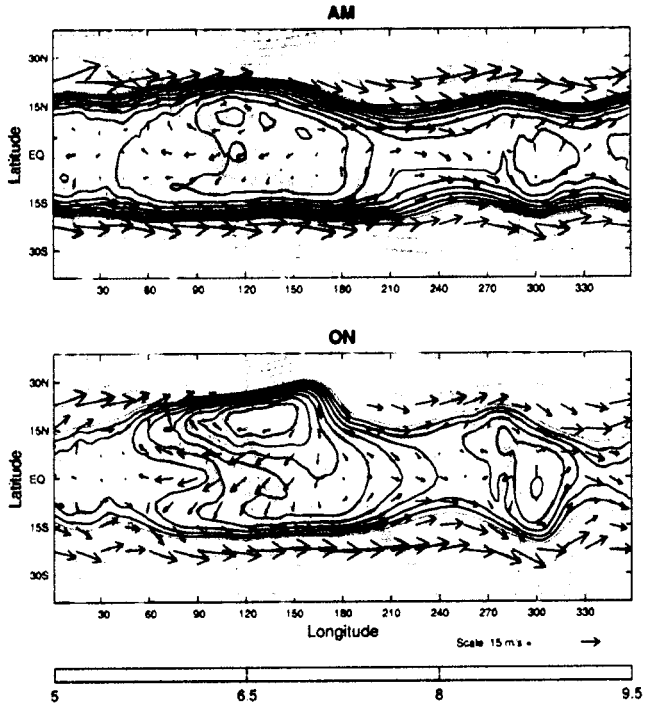

Figure 4.14: As in Figure 4.4 but for the AM and ON seasons.

Figure 4.14 shows the horizontal wind and geopotential height fields at the 150hPa level during the transition seasons. Vestiges of the Asian summer monsoon circulation are still apparent during ON, with northeasterly flow over the maritime continent and the Indian Ocean. In contrast, the AM stationary waves are weak and the circulation is

essentially symmetric about the equator. Although it is not immediately apparent from Figure 4.14a, it is interesting to note that the zonally averaged geopotential height over the equator belt is higher during AM than during any other season.

4.5 Seasonal variations in the zonally symmetric flow

Figure 4.15 shows the annual cycle of the climatological monthly mean zonally averaged zonal wind, meridional wind, and eddy momentum fluxes at the 150hPa level, and Figure 4.16 shows the annual cycle of the dominant terms in the zonal momentum balance (eq. 4.1) at that level. The zonally averaged and root-mean-square precipitation fields ($rms(precip) = [precip^{*2}]^{1/2}$) are indicated by shading in Figure 4.15 b and c, respectively. All three of the contoured fields in Figure 4.15 exhibit a strong, quasi-sinusoidal annual cycle, with opposing extrema in the monsoon seasons and weaker, more equatorially symmetric latitudinal profiles during the transition seasons. The mean meridional wind and flux of eddy momentum both exhibit a pronounced seasonal reversal, which accounts for the relatively weak annual-mean MMC and eddy momentum fluxes in Figure 4.1b and Figure 4.2a. The observed positive correlation between $[v]_c$ and $\partial[u]_c/\partial y$ over the course of the year leads to the easterly accelerations in Figure 4.7b as well as Figure 4.16a. The meridional winds in Figure 4.15b emanate from the belts of heavy zonally averaged precipitation, and the eddy fluxes of westerly momentum in the deep tropics (Figure 4.15c) are directed towards the belts of high rms-precipitation, which presumably represent the regions with the strongest eddy forcing. It is also apparent from

Figure 4.16 that the strong compensation between the mean meridional advection term and the eddy momentum flux convergence noted during individual seasons (Figure 4.11) is present throughout the year, at this level.

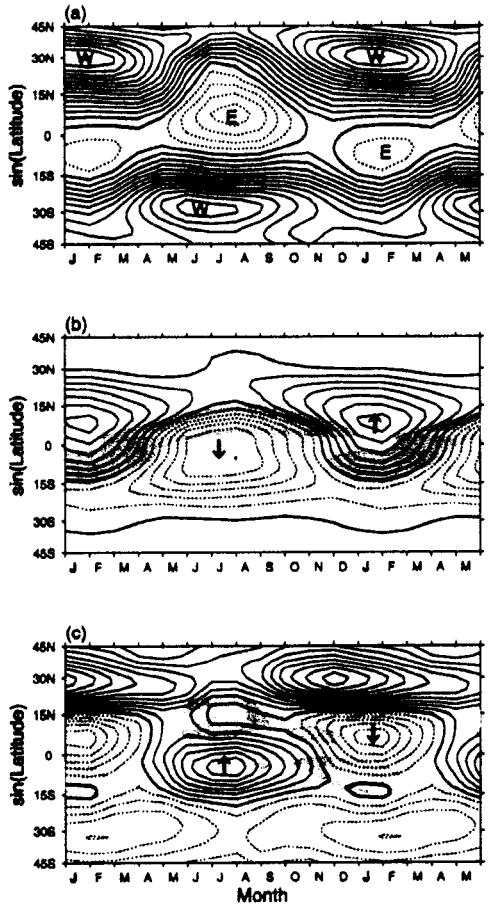

Figure 4.15: Time-latitude sections for 150hPa (a) zonally averaged zonal wind $[u]_c$ (contour interval 2 m s^{-1}), (b) zonally averaged meridional wind $[v]_c$ (contour interval 0.5 m s^{-1}) and precipitation (color) and (c) zonally averaged meridional eddy fluxes $[u^*v^*]_c$ (contour interval 5 m^2 s^{-2}) and rms precipitation (color). Solid contours are positive and dashed contours are negative; the zero line is thickened. The first five months of the calendar year are repeated. Colorbar as in Figure 4.14.

Several other features of the annual cycle in Figure 4.15 relate to the distinctions between the AM and ON transition seasons. The Northern Hemisphere westerlies are located farther poleward during ON than during AM, and the zero wind line that

separates the midlatitude westerlies from the tropical easterlies shifts northward abruptly during late spring and returns more gradually in autumn, consistent with results of Fleming et al. (1987). The tropical rain belt is also located farther northward during ON than during AM.

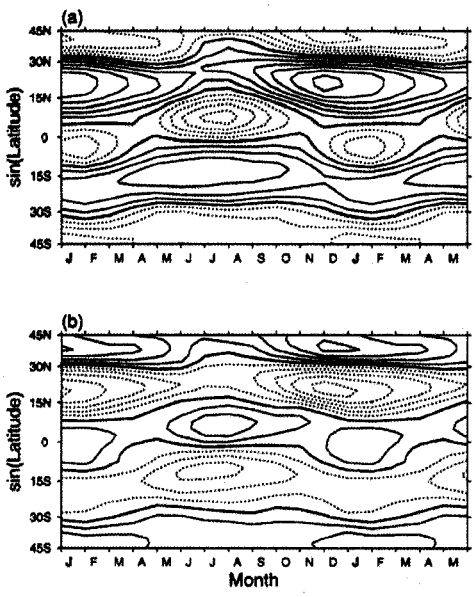

Figure 4.16: Time-latitude sections for the 150hPa leading terms in eq. 4.1: (a) the MMC term (first term on the RHS) and (b) the horizontal eddy term (third term on the RHS) in the momentum budget. Solid contours are positive and dashed contours are negative; the zero line is thickened. The contour interval is 10^{-5} m s^{-2}. The first five months of the calendar year are repeated.

Upon close inspection of Figure 4.15a it is evident that the zonal winds exhibit a weak semi-annual cycle with peak easterlies in the monsoon seasons and a change toward westerlies in the transition seasons. This feature shows up more clearly in the latitude-time section of equatorially symmetric zonal wind ($[u]_{sym} = ([u]_N + [u]_S)/2$), where the subscripts N and S refer to the Northern and Southern hemisphere values) shown in Figure 4.17.

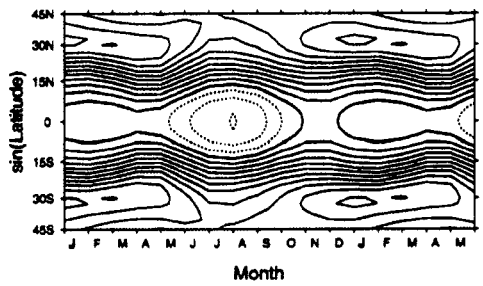

Figure 4.17: Time-latitude section of the equatorially symmetric component of the 150hPa zonal wind, $[u]_{sym}$. Solid contours are positive and dashed contours are negative; the zero line is thickened. Contour interval: 2 m s^{-1}, same as in Figure 4.15a.

The semi-annual variations of the zonal wind are not restricted to the equatorial belt, but extend into middle latitudes. We will consider the semi-annual variability of the tropical circulation in further detail in the next section.

4.6 Seasonal variations in the eddies

The equatorially asymmetric, seasonally reversing component of the stationary waves near the equator accounts for the eddy flux of westerly momentum across the equator from the winter hemisphere into the summer hemisphere, as documented in Figure 4.8 c and f. However, the equatorially symmetric part of the tropical stationary waves accounts for roughly 3/4 of the eddy kinetic energy at the 150hPa level equatorward of 30° latitude and exhibits a pronounced semi-annual cycle, with maximum amplitude during the monsoon seasons (Figure 4.18).

The equatorially symmetric component of the upper level flow pattern in JF, AM, JA and ON is shown in Figure 4.19. A Rossby-wave couplet is evident throughout the year over the Indo-Pacific sector. This equatorially symmetric wave pattern is strongest during JF and JA and weakest during AM.

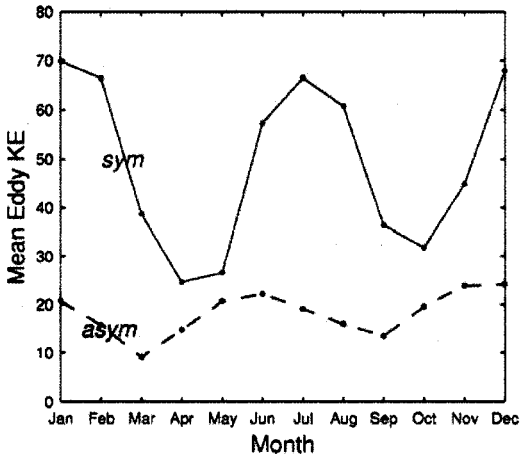

Figure 4.18: Equatorially symmetric (solid red line) and asymmetric components (dash-dot blue line) of the mean eddy kinetic energy of 150hPa wind field for the 30°N-30°S belt.

The center of the gyres shifts in longitude from ~160°E in JF to ~80°E in JA. This east-west shift in the stationary wave pattern is accompanied by a subtle shift in the relative prominence of the rainfall maxima that lie just to the east and to the west of the marine continent.

Equatorial easterlies are evident year round in the zone of east-west geopotential height gradient within and to the west of the Rossby wave couplet. The "Tropical Easterly Jet" across the equatorial Indian Ocean during JA is a manifestation of this feature. Only during JF, when the geopotential height gradients along the equator are particularly strong, do the westerlies in the Kelvin-wave signature, to the east of the couplet, make a significant contribution to the tropics-wide eddy kinetic energy.

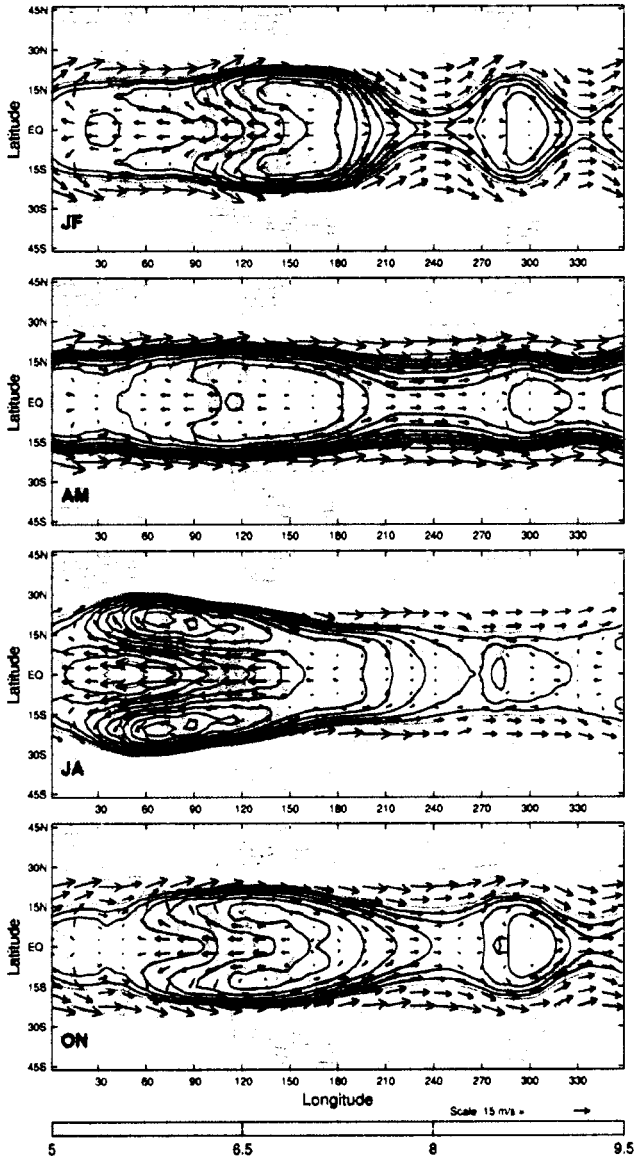

Figure 4.19: Horizontal maps of the symmetric component of 150hPa geopotential height (m), wind (m s^{-1}) and precipitation (color; mm day^{-1}). The contour interval for the geopotential height is 100 m (gray lines); additional contours (black) at 10 m were inserted in the tropical region. The contour range is similar to that in Figure 4.4.

4.7 Discussion

In this study fields derived from the NCEP reanalyses have been used to investigate the seasonal evolution of the zonally averaged circulation, the climatological-mean

stationary waves, and the zonal momentum balance in the tropical upper troposphere. The zonally averaged component of tropical diabatic heating forces a seasonally reversing, thermally direct MMC cell, with strong cross-equatorial flow at the 150hPa level during the monsoon seasons. The advection of momentum by this cross-equatorial flow induces an easterly acceleration of the upper tropospheric zonal flow, which is balanced by the convergence of westerly momentum by the stationary waves. This balance prevails in both the annual-mean and individual seasons. The strength of the tropical eddy momentum fluxes varies in concert with the strength of the mean meridional flow across the equator, so that the net acceleration experienced by the zonal flow in the tropical upper troposphere remains nearly zero year-round. A similar balance was obtained by KH using an idealized GCM forced with a tropical eddy heat source and solstitial boundary conditions.

Presumably, stronger easterlies would be observed in the equatorial upper troposphere during the monsoon seasons were it not for the convergence of westerly momentum into the equatorial belt by the stationary waves. Eddy fluxes are not taken into account in the axisymmetric models, e.g. Lindzen and Hou (1988) and Fang and Tung (1999), and thus such models tend to produce unrealistically strong easterly winds over the equator. Were it not for the easterly acceleration induced by the MMC, the equatorward flux of momentum associated with tropical stationary waves would lead to the buildup of westerly flow over the equator, as demonstrated by KH.

Observations indicate a strong tendency for the mass flux in the upper branch of the Hadley circulations and the flux of westerly momentum by the stationary eddies in the

tropical upper troposphere to be in opposite directions. This tendency for opposition may reflect the preference for the zonally averaged tropical rain belts to occur at the same latitudes as the eddy forcing, so that upper tropospheric mass flux divergence coincides with the eddy flux convergence.

The upper tropospheric stationary waves, which are strongest near the 150hPa level, are dominated by an anticyclonic Rossby-wave couplet centered near or just to the west of the heating and an equatorial Kelvin-wave signature to the east. Diffluent easterly flow around the western flank of the Rossby-wave couplet, in combination with confluent westerly flow to the east of the heating, induces the equatorward eddy flux of westerly momentum.

A notable result is the high degree of equatorial symmetry present in the tropical stationary wave pattern throughout the year. Contrary to what might be expected on the basis of simple inferences based on the distribution of diabatic heating, the equatorially symmetric component is strongest not during the transition seasons, when the heating is most symmetric about the equator, but during the monsoon seasons, when the eddy forcing is located in the summer hemisphere.

Many of the features in the observations can be replicated with a simple model of the nonlinear solution to the shallow water wave equation forced with a tropical heat source. As observed, eddy heating on or near the equator leads to a Rossby-wave response with an equatorward eddy momentum flux and the solution retains a high degree of equatorially symmetric component even when the heating is moved off the equator.

Another intriguing aspect of the seasonality of the tropical general circulation is the marked distinction between the April-May (AM) and October-November (ON) transition seasons. AM is the season of strongest equatorial symmetry in the distributions of rainfall and MMC, and weakest stationary waves and eddy momentum fluxes. In ON the tropical rain belt remains centered north of the equator, resulting in a northward displacement of the Northern Hemisphere Hadley cell and subtropical jet streams relative to their AM positions. The reasons for these asymmetries have yet to be elucidated.

5. Structure of equatorial stationary waves

5.1 Introduction

The zonally asymmetric component of the climatological-mean atmospheric circulation, also known as stationary waves or standing eddies, plays an important role in the general circulation of both the extratropics and the tropics. The *extratropical* stationary waves have received significantly greater attention in the scientific literature (e.g. Lau, 1979; Hendon and Hartmann, 1982; DeWeaver and Nigam, 2000; Held et al., 2002). Most of the literature on the *tropical* stationary waves has tended to focus on the monsoons (Ramage, 1971; Newell et al., 1972; Webster et al. 1998; Trenberth et al., 2000). Throughout the year the tropical stationary waves dominate the tropical circulation and mediate the effects of changes in the tropical heating upon the global circulation. They also influence the zonally symmetric flow through their equatorward transport of westerly angular momentum, as documented in Chapter 4.

The discussion of the equatorial stationary waves in the previous chapter focused on the horizontal structure at the level of maximum amplitude in the upper troposphere. Of the levels included in the ERA40 Reanalysis, the 150hPa wind and geopotential height fields exhibited the highest amplitude. It is notable that this level of peak amplitude occurs above the top of the most vigorous convection (e.g. Highwood and Hoskins, 1998; Gettelman et al., 2002), near the base of the so-called "tropopause transition zone" (Atticks and Robinson, 1983).

In this chapter we examine the vertical structure of the annual-mean equatorial stationary waves using 1000-50 hPa ERA40 data, with emphasis on the near-equatorial, upper tropospheric geopotential height and wind fields. In section 5.2 we describe the horizontal structure of these waves, focusing primarily on the 150hPa atmospheric level and conditions at the earth's surface. In section 5.3 we document the vertical structure of the waves in the equatorial plane, and in section 5.4 we analyze and compare vertical profiles for geopotential height, temperature and vertical velocity. The results are discussed in section 5.5.

5.2 Horizontal structure

The observed annual-mean 150hPa height and wind fields are shown in Figure 5.1a, superimposed upon the 300hPa vertical velocity field. As in the previous chapter, extra geopotential height contours are plotted in the tropical belt in order to resolve the weak near-equatorial features in the stationary waves.

The resemblance between the observed fields (Figure 5.1a) and the response to an isolated equatorial heat source in the simple nonlinear shallow-water wave equation model (Figure 5.1b), although not perfect, is clearly evident: the two patterns exhibit the same overall shape, with a juxtaposition of a Kelvin wave to the east and Rossby-wave gyres to the west of the maximum in the geopotential height field over the western Pacific. A prominent feature of the wind field is the equatorial easterly jet down the geopotential height gradient in the trough that separates the maxima in the geopotential height field associated with the Rossby-wave gyres. The flow in the jet is diffluent, while

the westerly flow to the east of the wave couplet is confluent. Hence, the meridional motions associated with the wave pattern produce an equatorward eddy flux of westerly momentum, as discussed in the previous chapter.

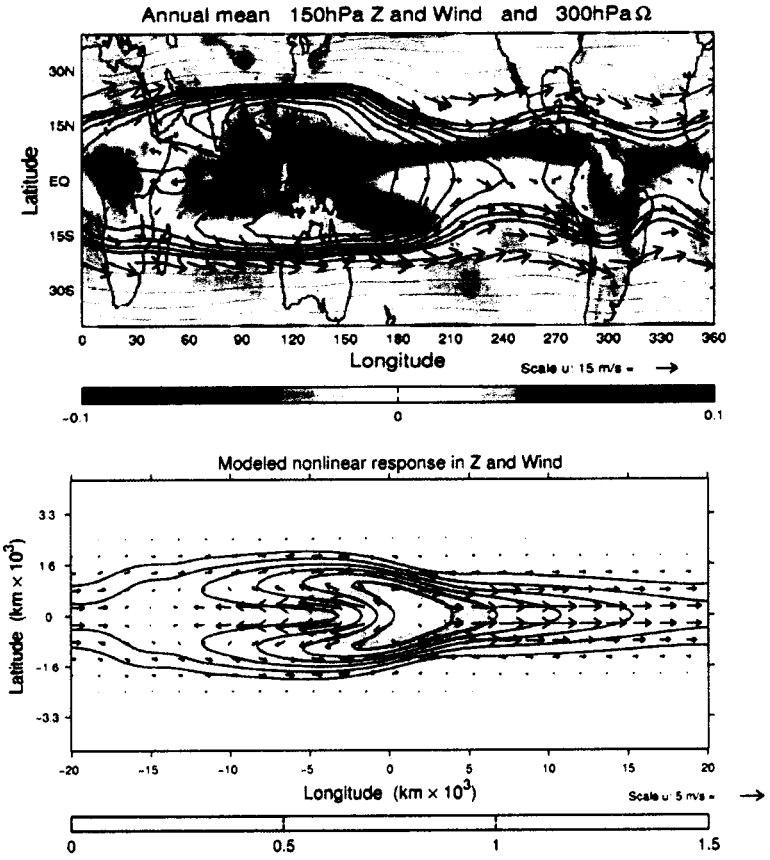

Figure 5.1: (a) 150hPa annual-mean geopotential height (contours; m) and wind (arrows; m s^{-1}); superimposed (color) is the 300hPa omega field (Pa s^{-1}). As in fig. 4.4, the contour interval for the geopotential height is 100 m (gray lines); additional contours (black) at 10 m are inserted in the tropical belt. Contour succession: (..14100, 14200, 14210, 14220,..) m, with the first black contour at the separation between gray and black contours representing the 14210 m line. The wind arrows are plotted only up to 23° in both hemispheres; (b) Figure 1.8 repeated - Nonlinear solution of the shallow water wave equation forced by an equatorial heat source. The geopotential height field is contoured, the wind field is represented by arrows and the heat source is shown in color.

In addition to the primary region of ascent associated with deep convection over the maritime continent (centered ~120°E), more localized maxima are discernible over

equatorial Africa and tropical South America. The associated height and wind perturbations are much less prominent than those in the vicinity of the marine continent. There are no clearly discernible height perturbations associated with the ITCZ over the Atlantic and eastern Pacific sectors, but there is a tendency for southward flow across the equator.

The boundary level counterpart of the upper tropospheric pattern is shown in Figure 5.2. The upper panel shows the sea level pressure (SLP) and surface wind fields. The sea surface temperature field is shown in the lower panel, superimposed on the 300hPa vertical velocity field. Regions of strong ascent (blue shading) are indicative of deep convection. The equatorially symmetric planetary-wave signature observed at upper levels is not as pronounced at this level, and the ITCZ is relatively more prominent in the wind field. These distinctions between the flow at the two levels may be due to the role of boundary layer baroclinicity and friction in shaping the wind and pressure fields close to the earth's surface (Lindzen and Nigam, 1987). Nevertheless, features with opposing polarity to those at upper levels are observed: the central equatorial low beneath the upper level high, the easterlies over the central and eastern Pacific beneath the upper level westerlies, the westerlies over the eastern Indian Ocean beneath the upper level easterly jet and the off-equatorial highs beneath the off-equatorial troughs over the eastern Pacific. Note also the change in sign between the equatorial SLP gradients in the eastern and western hemispheres near 165°E, where the transition from the rain belt centered over the marine continent and the dry zone in the central and eastern equatorial Pacific takes place.

The main region of convection is located in the area where the surface winds are strongly convergent (Figure 5.2a), over the eastern hemisphere 'warm pool' in the sea surface temperature field (Figure 5.2b). Over the Atlantic and over the Pacific east of 165°E, pressure decreases from east to west, maintaining the easterly surface winds which, in turn, sustain the equatorial 'cold tongues' in the SST.

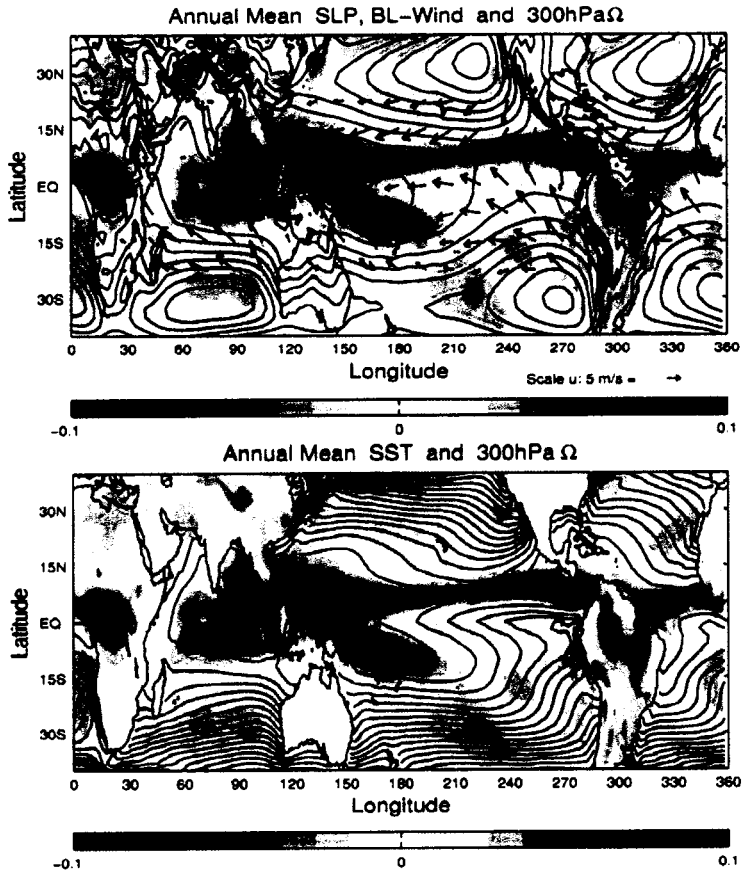

Figure 5.2: Annual mean (a) sea level pressure (contour interval 1.5; min/max values shown 1009/1021 mb), boundary layer wind (arrows) and 300hPa omega field (color, Pa s^{-1}) and (b) sea surface temperature (contour interval 1; max value shown 29°C) and 300hPa omega field (color Pa s^{-1}).

The distribution of deep convection field is determined by the underlying SST distribution: ascent is observed over the warm ocean temperatures in the Indo-Pacific

warm pool region and along the ITCZs, while subsidence dominates over the eastern Pacific and Atlantic cold tongue regions (Figure 5.2b).

5.3 Structure in the longitude-height plane

Figure 5.3 shows the structure of the annual-mean equatorial circulation in the longitude-height plane. This cross-section represents a meridional average over the belt extending from 5°N to 10°S, including the eastern Pacific equatorial dry zone, but excluding most of the ITCZ. The eddy geopotential height (Z^*), defined as the departure of the geopotential height field from its zonal average at each level ($Z^* = Z - [Z]$), is shown together with the total zonal and vertical wind components for all longitudes and from 1000 to 50 hPa.

The most striking feature in Figure 5.3 is the maximum in Z^* with an amplitude of ~25m at 175hPa, centered around 165°E, near the eastern end of the primary region of deep convection over the warm pool. Upper tropospheric minima are observed around 110°W and 25°W (250° and 335° in the figure labels), corresponding, respectively, to the eastern Pacific and Atlantic troughs in the 150hPa height field (Figure 5.1a). The Walker cell (Figure 1.9) is clearly discernible, and an analogous cell is situated over the Atlantic. The strong correspondence between the zonal gradient of zonal wind and the vertical gradient of the vertical velocity suggests that the mean motions in this plane obey a two-dimensional continuity equation. Hence, the meridional mass fluxes into and out of this belt must be relatively small, compared to the zonal mass fluxes within the belt.

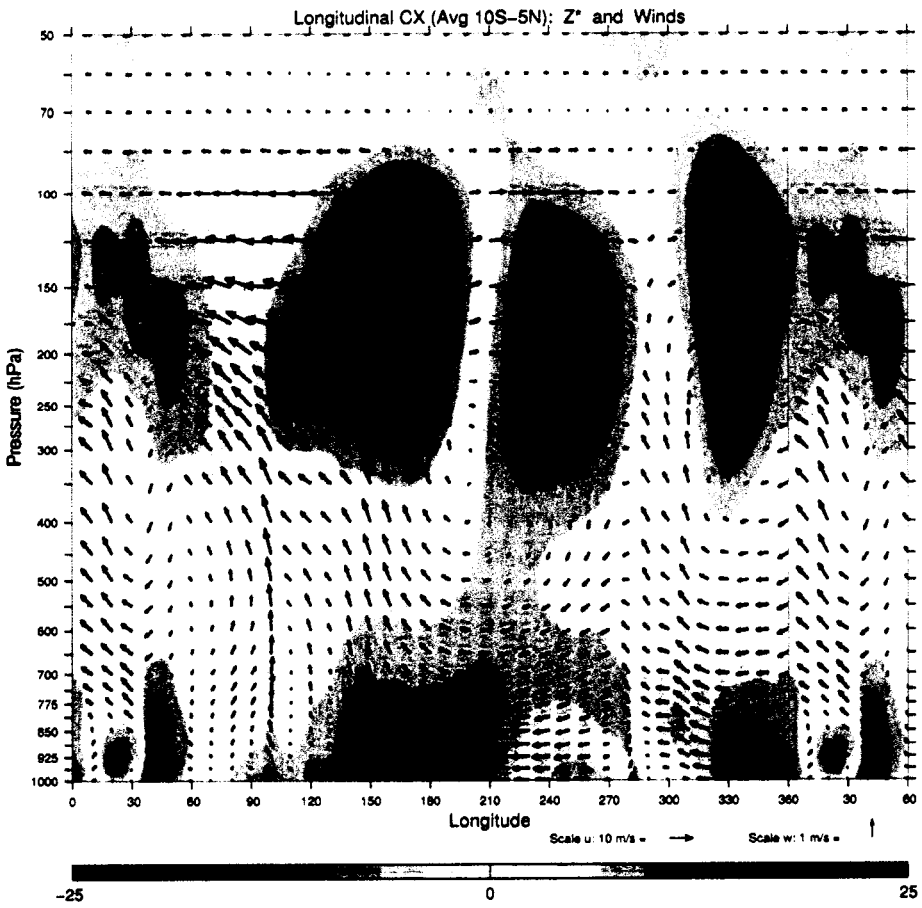

Figure 5.3: Longitudinal cross-section of the eddy geopotential height (Z*) (colored shading; m) and zonal and vertical wind components (arrows; m s^{-1}), for the latitudinally 10°S-5°N averaged region. The longitudinal region 0°-60° is repeated on the right hand side of the figure for visual continuity.

Figure 5.4 shows a longitude-height representation of the annual mean eddy temperature field, T^* ($T^* = T - [T]$). The strongest temperature perturbations are observed in the boundary layer. In the layer extending from the top of the boundary layer up to ~400hPa, where most of the condensation heating is occurring, the temperature perturbations are relatively weak. The strongest perturbations above the boundary layer are located at the tropopause level around 100hPa and in the mid-troposphere around 300hPa. The temperature perturbations at these two levels tend to occur in couplets of

opposing sign immediately above and below the extrema in the eddy geopotential height (Figure 5.3), as required for hydrostatic balance. The dominant feature in the temperature pattern is located around 165°E, at 100hPa, where it is ~1.8°C colder than the zonally averaged temperature.

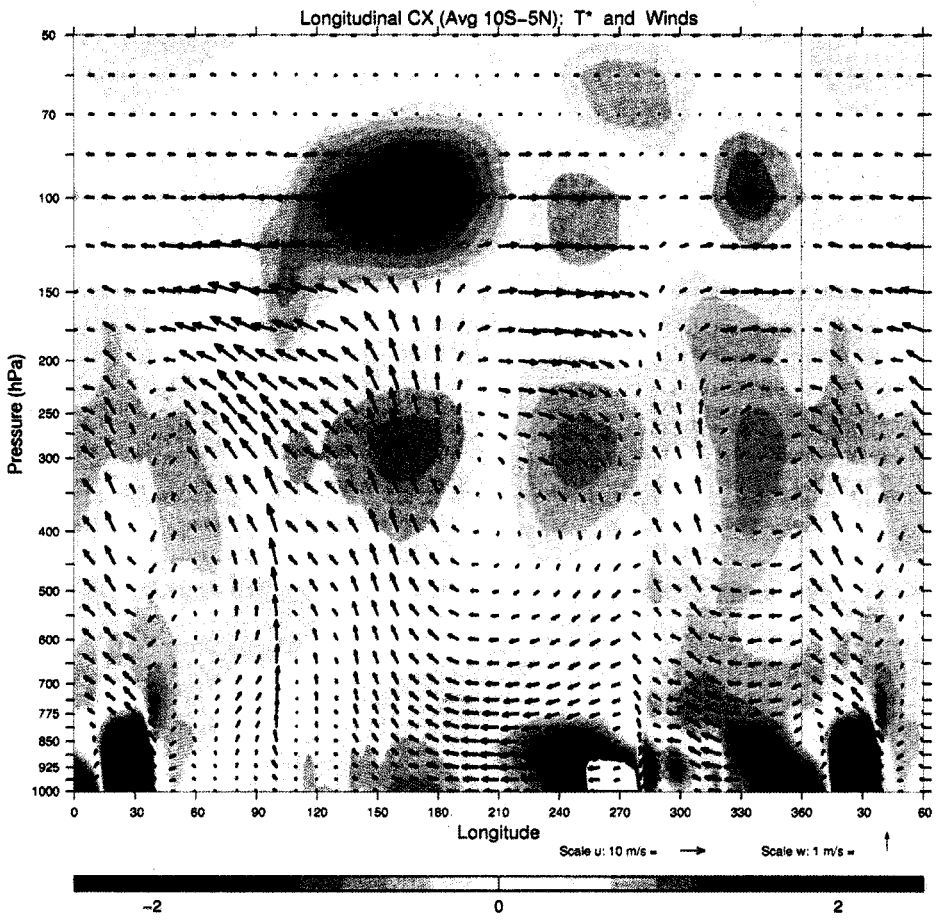

Figure 5.4: Same as in Fig. 5.3 but for the eddy temperature field (T*; °C).

The annual mean relative humidity (RH) field shown in Figure 5.5 is characterized by relatively large values (up to 90%) in the boundary layer and in the ~200-100 hPa layer, consistent with the structure in soundings examined by Ciesielski et al. (2003).

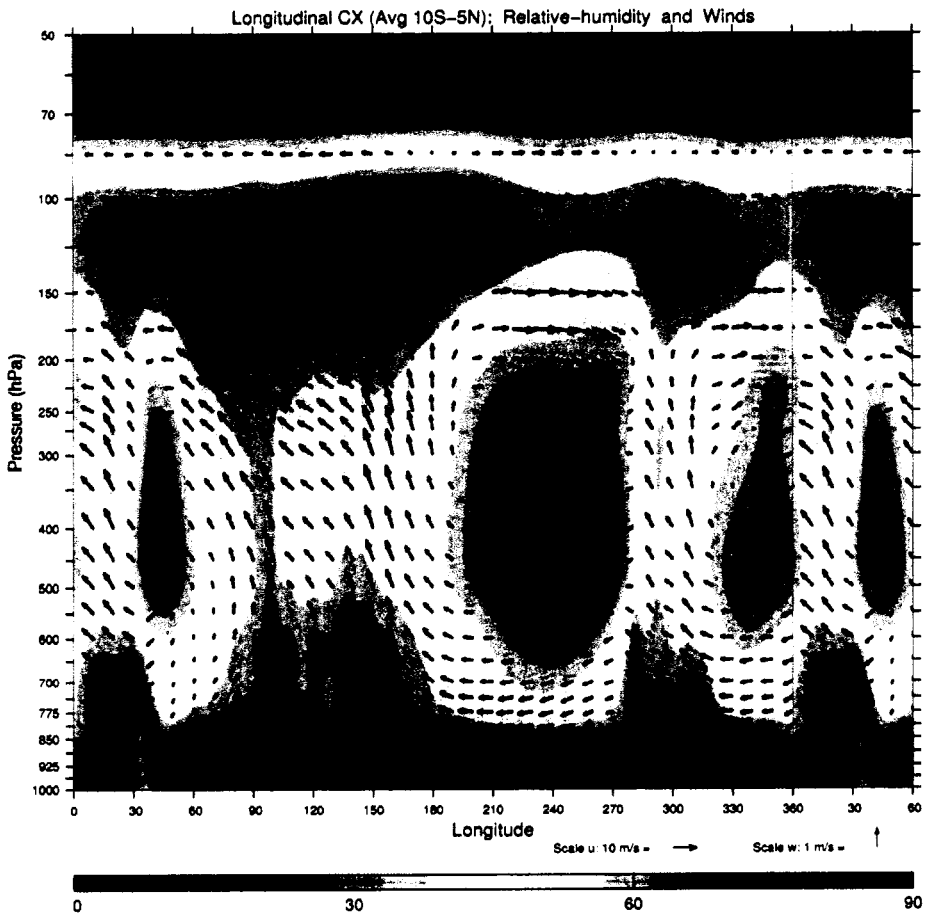

Figure 5.5: Same as in Fig. 5.3 but for the relative humidity field (percent %).

The maximum RH in the upper tropospheric region is located in the same longitudinal band as the extrema in Z^* and T^*, around 165°E. Relative humidities as low as 30% are observed in regions of subsidence in the middle troposphere. In regions of ascent RH increases rapidly with height in the 200-150 hPa layer, the upper limit of moist convection (Highwood and Hoskins, 1998; Jackson et al., 2001; Yu et al, 1998). The 150-100 hPa layer is nearly saturated.

The distribution of equivalent potential temperature θ_e shown in Figure 5.6 exhibits a minimum ~700hPa and a gradual increase of atmospheric stability with altitude in the

upper troposphere. The waves are clearly discernible in the θ_e field at altitudes extending all the way up to the tropopause, with evidence of a phase reversal ~175hPa.

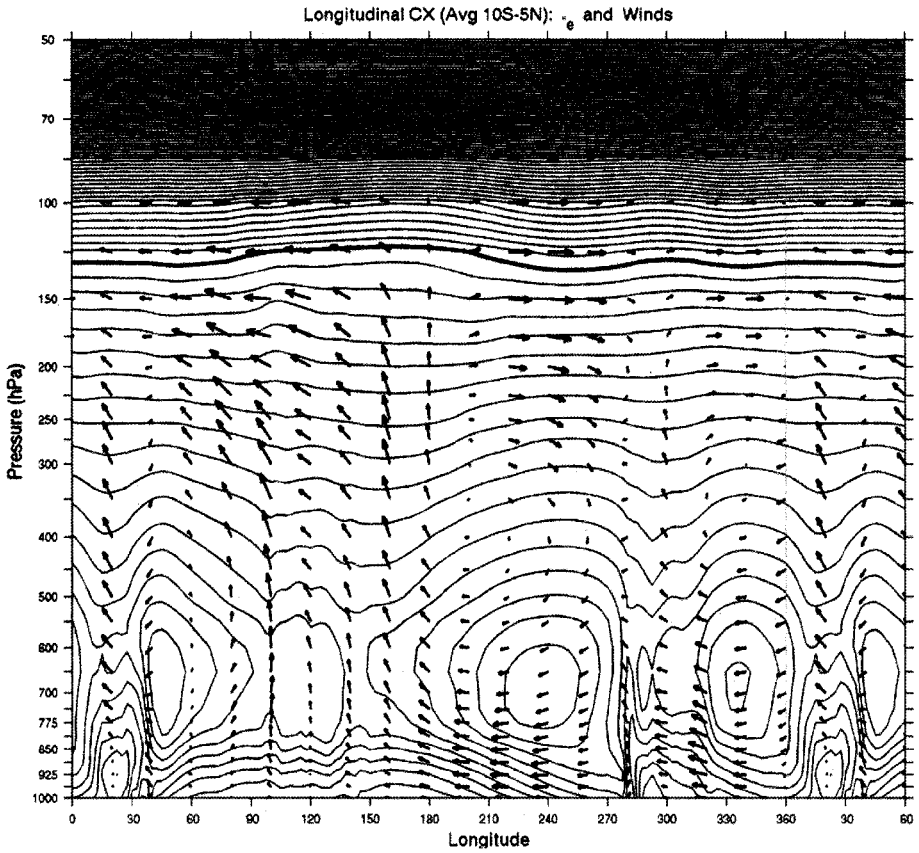

Figure 5.6: Same as in Fig. 5.3 but for the equivalent potential temperature field. Contour interval 2K; for reference the 360K line is thickened.

At the 300hPa level the circulation in the waves is thermally direct, with ascent over the warm pool and the relatively warm continents and descent over the Atlantic and Pacific equatorial cold tongues. Above ~150hPa the circulation is thermally indirect, with ascent of cold air and descent of warmer air. The strongest ascent is centered ~165°E, where the isentropes at these levels bulge upward. Air diverges out of the region of ascent flows across isentropes toward higher values, which is indicative of cold advection, and,

hence, radiative heating. In agreement with analysis of the horizontal transport at tropopause levels by Holton and Gettelman (2001) and the three dimensional air trajectories computed by Fueglistaler et al. (2004), the easterly jet at the tropopause level at 120°E is characterized by flow across the θ_e surfaces toward higher values, indicative of a troposphere-to-stratosphere mass flux.

5.4 Vertical profiles of wave amplitude

Figure 5.7 shows vertical profiles of the root-mean-squared amplitude of the annual-mean stationary waves in the geopotential height, temperature and vertical velocity fields, for the same equatorial belt as considered before. Each profile was computed by taking the square-root of the spatially averaged amplitude of the annual-mean stationary field (e.g. $rms(Z^*) = sqrt[mean(Z^{*2})]$). The wave perturbations in the temperature field reach their maximum amplitude at the 100hPa and 300hPa levels, where the corresponding geopotential height perturbations exhibit their strongest vertical gradient. The minimum in the amplitude of the temperature perturbations is located ~175hPa, coincident with the amplitude maximum in the geopotential height perturbations. In the layer of strongest condensation heating between ~775 and 400 hPa the temperature perturbations are relatively weak and the vertical velocity perturbations are nearly constant with altitude. There is no pronounced vertical velocity maximum in this layer. Above 350hPa the vertical velocity steadily decreases with decreasing pressure, indicative of divergence out of regions of ascent. The steepest slope is found ~175hPa, where the geopotential height perturbations are strongest. The vertical velocity perturbations approach zero ~100hPa.

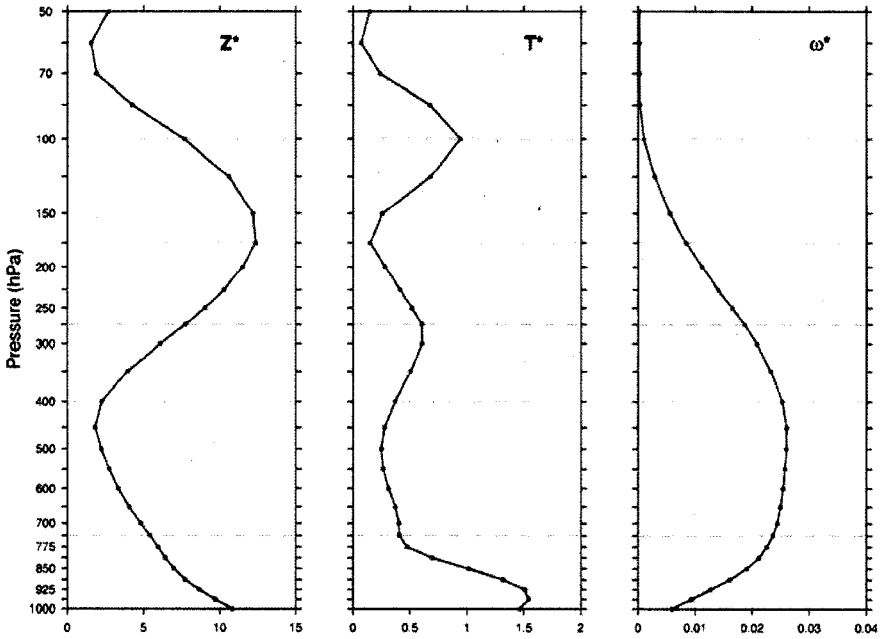

Figure 5.7: Vertical profiles of the root-mean-squared amplitude of the annual-mean stationary waves in the geopotential height (left; m), temperature (middle; °C) and vertical velocity (right; Pa s^{-1}) fields.

Up to this point we have focused exclusively on the annual mean *stationary* wave fields. One may wonder if the horizontal and vertical structures depicted here are also representative of the *transient* waves in the tropical troposphere. Figure 5.8 shows the vertical profile of the *rms* amplitude for the annual-mean stationary vertical velocity and two terms representing transient perturbations. The first term is defined as the departure of the seasonally-varying monthly climatology from the annual mean, and will be referred to as the *climatological-transient* vertical velocity component and the second term is defined as the departures of the monthly values from the seasonally-varying monthly climatology, and will be referred to as the *anomalous-transient* vertical velocity component.

The three vertical profiles exhibit similar shapes, with strong increase in amplitude with height just above the earth's surface indicative of boundary layer convergence, nearly constant values in the mid-tropospheric convective layer, and a monotonic decrease with height in the 300-100 hPa layer. A similar resemblance between vertical profiles for stationary-waves and transients is also observed in the case of the geopotential and temperature fields (not shown).

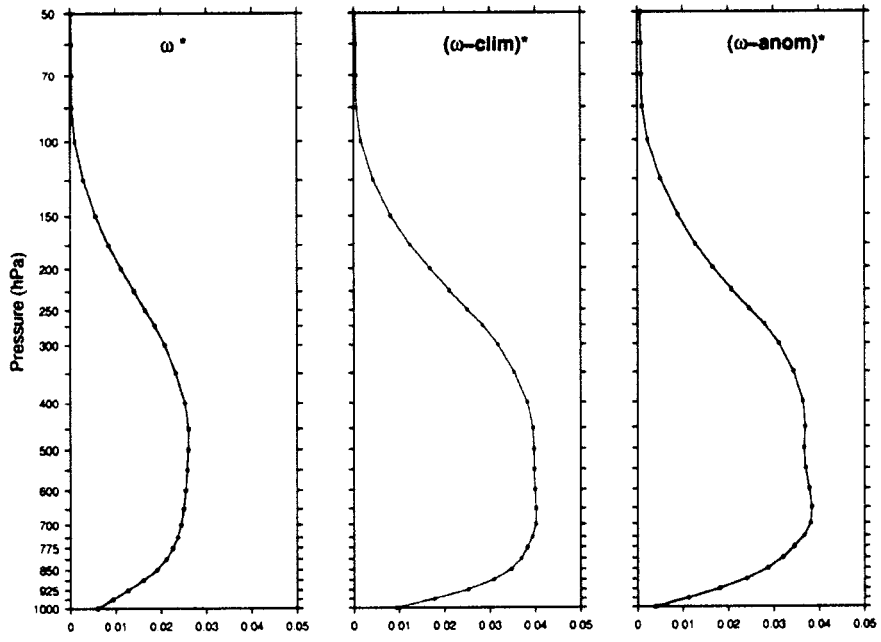

Figure 5.8: Vertical profiles of the root-mean-square amplitude for: annual-mean stationary (left), climatological-transient (middle) and anomalous-transient (right) vertical velocity perturbations (Pa s^{-1}).

The schematic in Figure 5.9 summarizes the observed vertical structure of the equatorial stationary waves in a region of ascent. Rather than a clearly defined level of maximum ascent, one finds a layer of nearly constant vertical velocity, extending from around 750hPa, not far above the top of the boundary layer, up to ~400hPa. The maximum mid-tropospheric temperature is located around 300hPa, above the layer of

strongest ascent and maximum latent heat release. The low level convergence is concentrated in the boundary layer while the upper level divergence extends from ~ 400 to 100hPa. Although the tops of most deep convective clouds are located around 200-150 hPa, the divergence on the planetary-scale extends upward to ~100hPa in accordance with the observed slowly decreasing rate of ascent. The maximum amplitude of the stationary eddies, at ~175hPa is pictured as being above the tops of most of the convective clouds, and vertically flanked by temperature extrema of opposing sign.

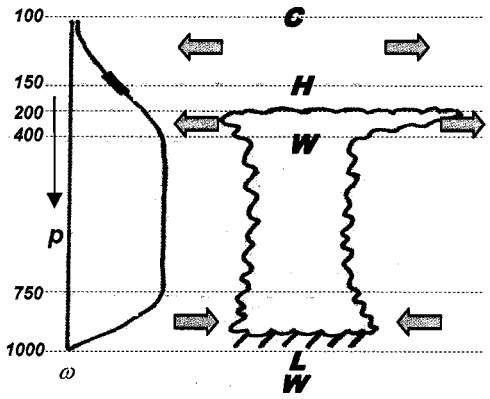

Figure 5.9: Schematic of the vertical organization of the tropical convection and the profile of vertical velocity, as shown by the observations. "*C*" stands for *Cold*, "*W*" stands for *Warm*, "*H*" stands for *High* and "*L*" stands for "*Low*".

5.5 Discussion

In this section we have described the three-dimensional structure of the annual mean tropical stationary waves based primarily on the ERA-40 data. We have focused mainly on the *annual mean* structure. That is not to say that variability does not play an important role in modulating these waves and the structure of the upper troposphere. The

seasonally-varying stationary waves and the anomaly fields observed in association with the annual cycle, El Niño/La Niña and the Madden-Julian Oscillation, could have somewhat different structures than the patterns and features emphasized here.

We have shown that the geopotential height field in the tropics, though much flatter than in extratropical latitudes, is nonetheless highly informative. It is more revealing than the streamfunction field in the sense that it bears a strong relation to the total wind field, which includes a substantial irrotational component. The observed geopotential height field in the tropical belt strongly resembles theoretical solutions of shallow-water wave equation models forced by a tropical heat source.

On the equator, the 165°E longitude marks the transition between the regions of deep convection over the Indo-Pacific warm pool and the equatorial Pacific dry zone and serves as a useful reference point for describing the equatorial stationary waves. It corresponds to the longitude where the tropical SLP gradient change sign (Figure 5.2) and it is also the region where the stationary waves exhibit their maximum amplitude in the upper tropospheric eddy geopotential height (Figure 5.3), temperature (Figure 5.4) and relative humidity (Figure 5.5) fields.

The theoretical framework reviewed in Chapter 1 is capable of explaining the main features of the observed horizontal stationary waves (Figure 5.1 a and b): the equatorial Kelvin wave and westerly winds are observed to the east of the heat source and the easterly jet and the equatorially symmetric Rossby gyres to the west of the main region of convection. Some differences between the observed and modeled features are noticeable, e.g. the fact that the observed maximum equatorial geopotential height is located ~45° to

the east of the Indonesian convective region, which is centered around 120°E, while the theory places it close to the center of the heat source. Previous studies have attributed this aspect of the flow to nonlinear effects (Hendon, 1986) or to localized cooling over tropical Asia (Sardeshmukh and Hoskins, 1988).

The low latitude stationary waves reach their maximum amplitude at ~175hPa, near or just above the tops of most deep convective clouds and just below the troposphere-stratosphere transition zone. It is also located near the level where the net radiative heating rate changes sign, from negative below to positive above. Below the level of maximum amplitude, the circulation is thermally direct, with strong ascent and latent heat warming in the rain areas and descent and radiative cooling in regions of subsidence. The active convection is limited to the altitude range where radiative cooling is efficient; thus the tropical convective anvil clouds occur at the level where the clear-sky radiative cooling decreases rapidly with altitude, in the layer centered ~200hPa (Hartmann and Larson, 2002). Above the level of peak wave amplitude the temperature and geopotential zonal departures are out of phase, indicative of a thermally indirect circulation. Although convective clouds do not penetrate to these levels, noticeable ascent is still observed, particularly around 165°E, in association with the vigorous divergent flow that characterizes the Rossby-Kelvin stationary wave pattern.

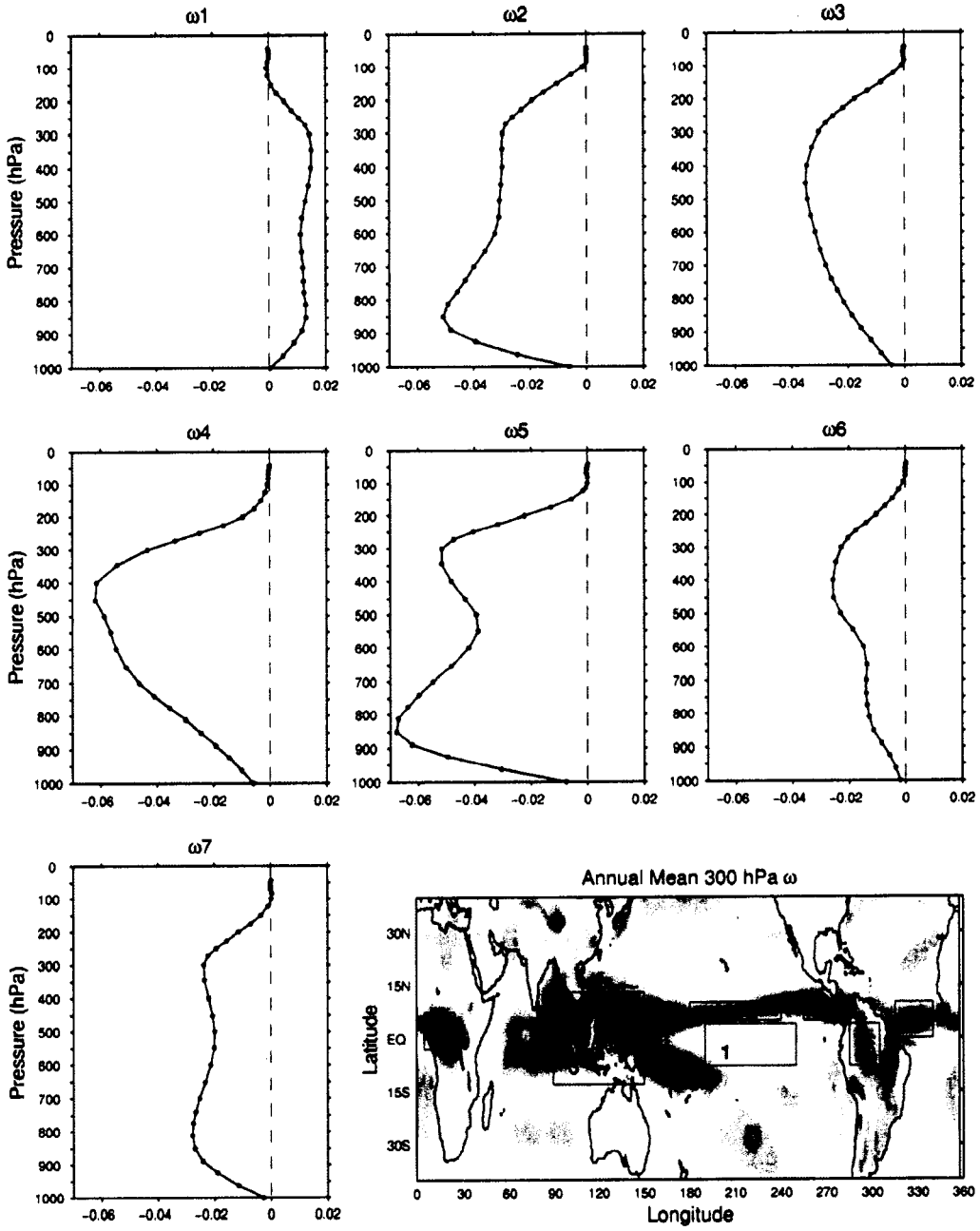

Figure 5.10: Vertical profiles of the vertical velocity field, averaged over different areas in the tropics, as shown in the map at the bottom.

The different behavior of convection at various locations throughout the Tropics is revealed by the vertical velocity soundings in Figure 5.10. The rate of descent over the equatorial Pacific dry zone (Figure 5.10a) exhibits a broad maximum extending from 850 to 300hPa, with a hint of a mid-level minimum. The three ITCZ regions (2, 5, and 7) exhibit a pronounced maximum just above the top of the boundary layer. In contrast, the continental regions (4 and 6) and the warm pool (3) exhibit a single, well defined maximum in the middle troposphere. The African convection (4) is the most vigorous of all, as also indicated by the satellite-observed frequency and distribution of lightning (Christian et al., 2003). Yet vertical velocities over Africa decrease much faster with altitude, approaching zero around 150hPa, than those over the warm pool, in which the ascent extends up to around 100hPa. Hence, there appears to be something 'special' about the warm pool that enables the planetary-scale ascent to extend higher than elsewhere in the tropics. It is conceivable that the slow, hydrostatically-balanced ascent in the planetary-scale stationary waves in this region rather than the updrafts in the convective clouds is responsible for maintaining the extremely cold temperatures in the tropopause transition zone in this region.

The dominance of the Indo-Pacific warm pool in the planetary-wave pattern in the upper troposphere (e.g., as opposed to Africa or South America), may be due to simply the fact that the upper level divergence (Trenberth, 2000) and deep convection over the warm pool is wider in zonal extent than the regions of enhanced convection over equatorial Africa and South America.

6. Variability of equatorial stationary waves

6.1 Introduction

In the previous chapter we documented the long-term *annual mean* structure of the equatorial stationary waves and the role that these waves play in shaping the tropical upper troposphere. Here we examine the *time-dependent* behavior of the low latitude zonally asymmetric circulations, in the context of the main modes of tropical variability: the annual cycle, ENSO, and the MJO.

In this section we use all year monthly ERA40 data and pentad NCEP data (Kalnay et al., 1996) for the period of record 1979-2001, to show that the principal modes of variability of the near equatorial flow all involve fluctuations back and forth between a *perturbed state* characterized by heavy rainfall over the Indo-Pacific warm pool ocean and an associated equatorially symmetric Rossby-wave couplet, and a *relaxed state* characterized by relatively light rainfall over this region and relatively uniform geopotential height and weak winds over the entire tropics.

6.2 Modes of variability

6.2.1 ENSO

The configuration of the stationary waves in the cold and warm phases of the ENSO cycle is contrasted in Figure 6.1. These plots were generated by compositing the data (total fields) with respect to the cold tongue index (CTI), defined as the average

SST anomalies over the 6°N-6°S, 180°-90°W region. The warm and cold composites are based on the ten highest and ten lowest values of the index. The contrast between the relaxed, predominantly zonal flow pattern in the warm phase (CTI+), versus the highly perturbed flow pattern observed in association with the cold phase (CTI-), is clearly evident.

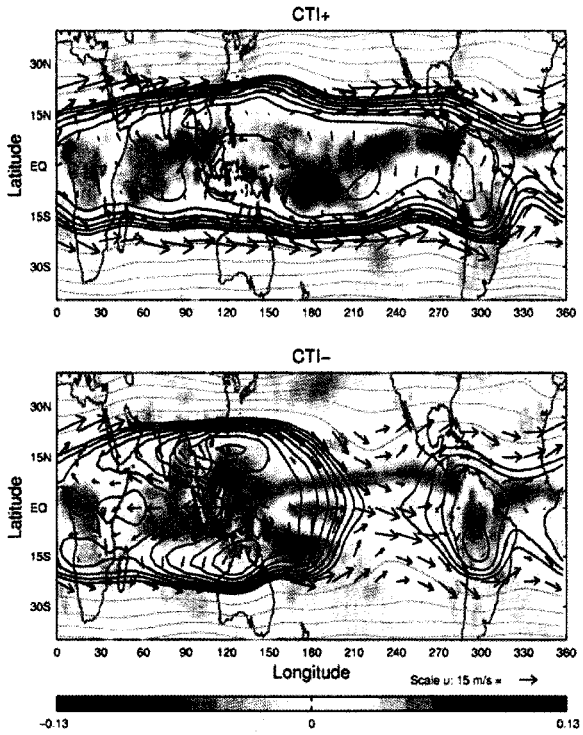

Figure 6.1: Composite maps with respect to the CTI index. The fields represented (geopotential height, wind and 300hPa omega) and the plotting convection are similar to those in Figure 5.1a.

The equatorial trough over the Indian Ocean and the large geopotential height gradient to the east of the Rossby-wave couplet are much more pronounced over the Pacific Ocean during the cold phase of the ENSO cycle. The easterly winds over the maritime continent and Indian Ocean and westerly winds over the central and eastern

Pacific are also much stronger. The stronger upper tropospheric flow pattern during the cold phase is accompanied by a pronounced contrast between the ascent over the warm pool region and descent over the eastern and central Pacific equatorial dry zone.

As a measure of the strength of the upper level stationary waves we use the Δu_{150} index, defined at each month as the difference between the strongest easterly and westerly winds on the equator, at the 150hPa level. The month-to-month correlation coefficient between Δu_{150} and the CTI, for 1979-2001, is 0.73, confirming that the ENSO cycle modulates the strength of the planetary-wave pattern.

6.2.2 The MJO

Fluctuations in the tropical circulation observed on the intra-seasonal time scale can also be described in terms of transitions back and forth between a perturbed state and a relaxed state of the upper tropospheric flow. In this case, the modulation of the strength of the pattern is accompanied by an eastward propagation of the convection from the Indian Ocean sector into the Pacific sector.

As a means of describing the evolution of the Madden Julian Oscillation (MJO), Wheeler and Hendon (2004) define the seasonally independent indices MJO1 and MJO2, the real and imaginary parts of a single complex number whose time series describes a counterclockwise rotating vector. The pair of indices were obtained by projecting the observed data, with the annual cycle and components of interannual variability removed, onto a pair of multiple-variable EOFs of the combined fields of near-equatorially averaged 850hPa zonal wind, 200hPa zonal wind, and satellite-observed outgoing longwave radiation (OLR) data.

MJO1, the real part of the index, can be viewed as a measure of the strength of the convection over the maritime continent centered at ~120°E, while the MJO2, the imaginary part of the index, can be regarded as an indicator of the longitude of the maximum convection; it is positive when the strongest convection is shifted east of its climatological maximum, toward the Pacific sector.

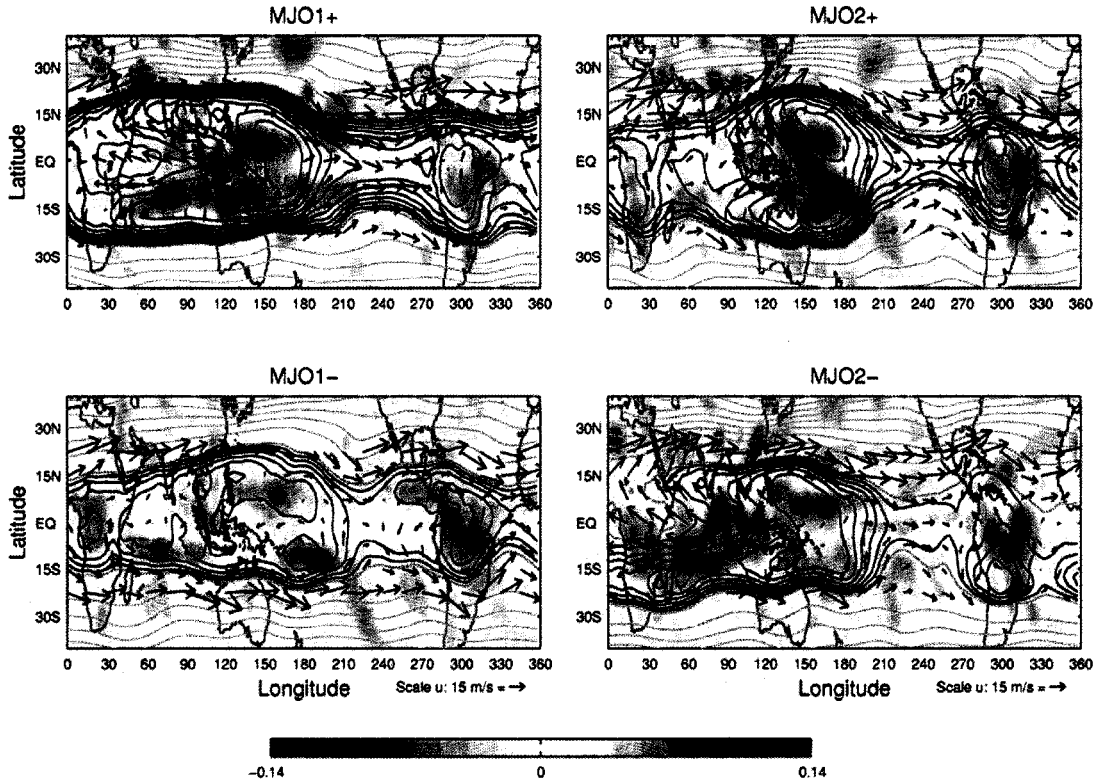

Figure 6.2: Same as in Figure 6.1 but for the MJO1 (left hand panels) and MJO2 (right hand panels) indices.

In order to document the changes in the upper level flow observed in association with the intra-seasonal oscillation, we have composited the data in terms of Wheeler and Hendon's indices. Figure 6.2 shows composite maps (obtained by averaging over

the data for the ten highest and ten lowest values of the respective index) for what might be termed the four phases of the MJO.

MJO1+ is characterized by enhanced rainfall over Indonesia, strong upper level stationary waves with well-developed Rossby gyres flanking a deep equatorial trough, strong equatorial easterly and westerly winds on the west and east sides of the main region of convection, respectively, and off-equatorial troughs over the dry eastern Pacific region (the *perturbed* phase of the upper tropospheric flow). Conversely, MJO1- is characterized by weak rainfall over the maritime continent and the adjacent regions, weak upper tropospheric waves and weak equatorial zonal winds (the *relaxed* phase). During positive MJO2, when convection is located over the western Pacific, the upper level stationary wave pattern appears 'contracted', with the 'Rossby gyre - equatorial trough - easterly jet' system having the most limited longitudinal extent.

When convection is located over the Indian Ocean (MJO2-), the equatorial geopotential trough is well developed and the winds in the region tend to be south-easterly as reflecting the influence of the Indian monsoon. Notice that throughout the evolution of the MJO cycle the eastern side of the couplet remains fixed and it is only the lobes to the west of the heat source that move back and forth resulting in an elongated or contracted wave pattern. The pentad Δu_{150} index correlates with MJO1 at –0.53, indicating that the strength of the stationary waves is modulated by the amplitude of the intra-seasonal oscillation.

6.2.3 Seasonal variations

The amplitude of the equatorial stationary waves also varies with season. In Chapter 4 we showed that these waves exhibits a pronounced semi-annual cycle with maximum amplitude during the monsoon seasons and minimum amplitude during the transition seasons, a month or two after the equinoxes. We also pointed out that the waves are weakest during April and May.

Figure 6.3 contrasts the April-May (AM) upper tropospheric wind and geopotential height fields with their counterparts averaged over the other ten months of the year (June through March).

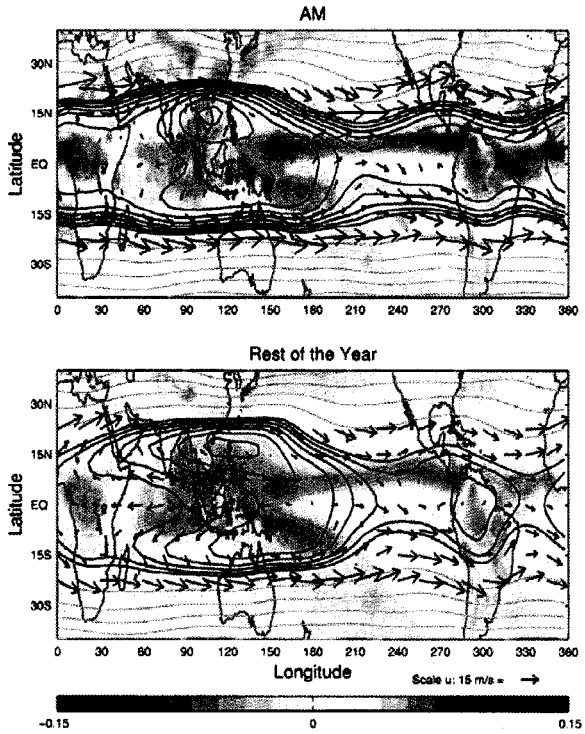

Figure 6.3: Same as in Figure 6.1 but instead of compositing, the data was averaged over the specified seasons.

Consistent with the findings for ENSO and MJO1, the decreased precipitation over the warm pool during spring is associated with weak stationary waves at upper levels (the *relaxed* phase), while the remaining ten months of the year exhibit more pronounced stationary waves at these levels (the *perturbed* phase).

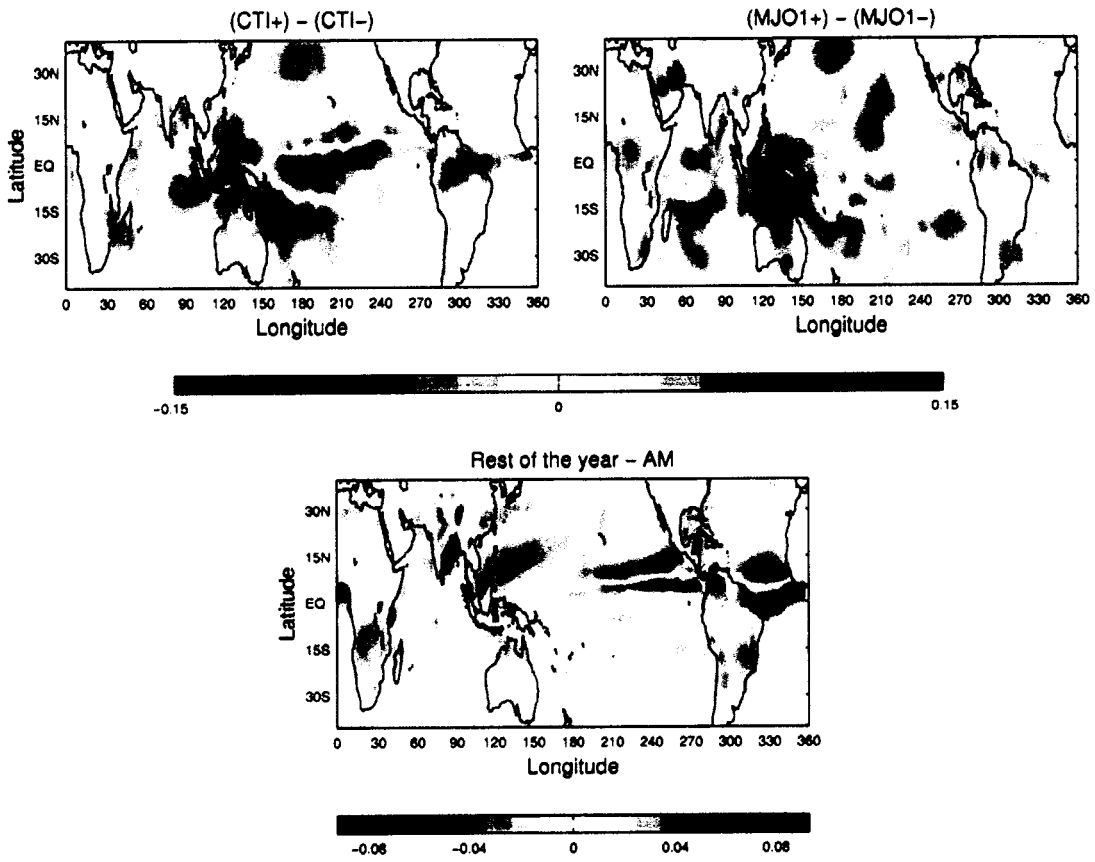

Figure 6.4: Difference maps between opposite composite maps for CTI, MJO1 (upper and middle panels) and between average seasonal maps (bottom panel), for the 300hPa omega field.

The 300hPa vertical velocity field associated with the difference between the ENSO, MJO1 and the annual cycle *relaxed* minus *perturbed* phases, respectively, is shown in Figure 6.4. In all three cases, the convection tends to be enhanced over the warm pool and suppressed over the central and eastern Pacific. The east-west

asymmetries that give rise to a Walker circulation over the Pacific are modulated most strongly by the ENSO cycle. The modulation is more subtle in the case of the MJO1 and annual cycle.

6.3 Convection and upper tropospheric flow

6.3.1 Composite maps

So far we exclusively observed the coupled system of the convection and upper tropospheric flow only in relation to principal modes of tropical variability. In this subsection we will use an indicator of the heating at a particular equatorial location as a basis for constructing composite maps. Instead of 300hPa vertical velocity we use CMAP precipitation field (Xie and Arkin, 1997).

We consider two equatorial boxes centered at 120°E, the midpoint of the massive convection region over the maritime continent, and 165°E, the focal longitude in the overall structure of the stationary waves as discussed in Chapter 5. The boxes are centered on the equator. They are 10° of latitude in width and 60° of longitude in length. Results were found to be relatively insensitive to the size of the boxes. As in the previous section, the composite charts are based on the ten highest and ten lowest values of the respective indices. Figure 6.5 contrasts composite maps for maximum and minimum averaged precipitation in the 120° box. When the precipitation in the box is minimum, the upper tropospheric flow is fairly weak, with a high degree of zonal symmetry (the *relaxed* state). On the contrary, maximum precipitation at 120°E is

characterized by a pronounced upper level stationary wave pattern, strong equatorial zonal winds and pronounced east-west asymmetries (the *perturbed* state).

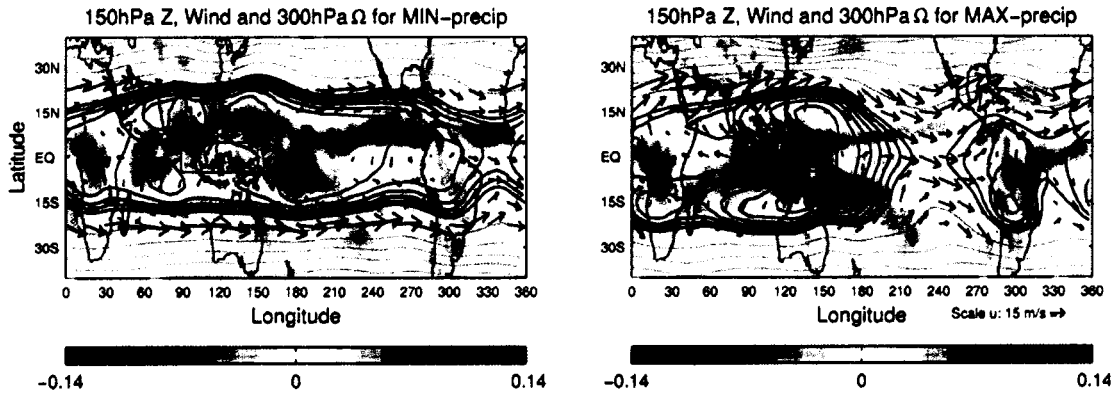

Figure 6.5: Composite maps with respect to an index defined as the average precipitation in the box centered at 120°. The fields (geopotential height, wind and 300hPa omega) represented and the plotting convection are similar to those in Figure 5.1a.

These findings are consistent with results of the previous subsection. Since variations in the convection over the Indo-Pacific warm pool are largely a result of the combined effects of the annual march, ENSO and MJO, this correspondence is in no way surprising, but it does confirm that the intensity of the Rossby-wave couplet at upper levels is strongly related to the intensity of the rainfall over the warm pool.

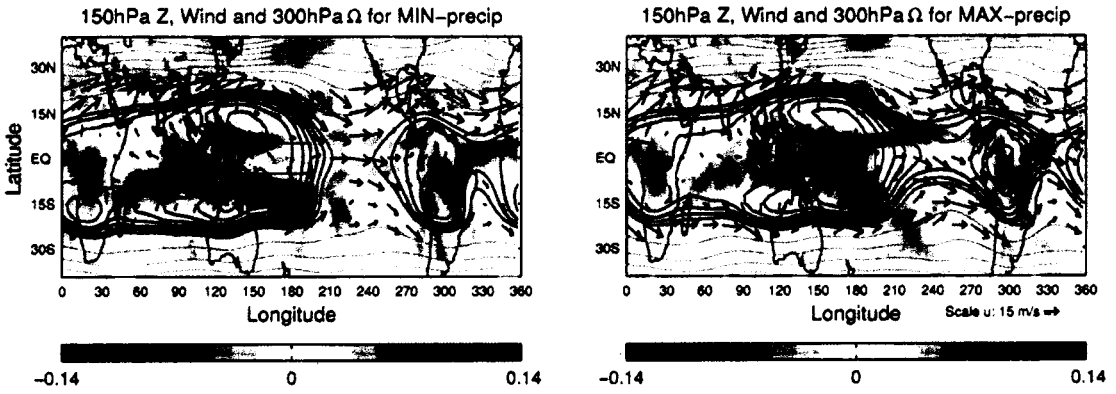

Figure 6.6: Same as in Figure 6.5 but for a box centered at 165°(E).

Moving the box 45° to the east, to 165°E, over the western equatorial Pacific (Figure 6.6), one can observe a different picture when comparing the two composite maps. In this case the upper tropospheric flow is in the *perturbed* state for both minimum and maximum precipitation in the box, hinting at the idea that the equatorial planetary waves are not strongly coupled to the rainfall rate in this particular region.

The contrasting character of the two composites, with a strong stationary-wave response to fluctuations in rainfall at 120°E and a weak stationary-wave response to fluctuations in rainfall at 165°E, is suggestive of a modal stationary-wave response to fluctuations in tropical heating.

6.3.2 MCA of the tropical precipitation and geopotential height

To place the foregoing results in the context of the total variability of the tropical circulation we performed a Maximal Covariance Analysis (MCA; Bretherton et al., 1992) on the anomalous precipitation field (15°S-15°N) and 150hPa geopotential height (40°S-40°N). This analysis technique extracts the pair of patterns that explains the most of the total squared covariance between two fields. The first two vectors emerging from the analysis are shown in Figure 6.7.

The first vector (Figure 6.7 top panels) explains 77% of the squared covariance and projects strongly upon the pattern observed in association with the ENSO cycle (e.g. Figure 6.4, upper panel or Dima, 2002). The precipitation and geopotential height associated time series for this first vector correlate with the CTI at levels of 0.81 and 0.60, respectively. Our findings are consistent with those in Yulaeva and Wallace (1994), who performed an MCA between the tropical temperature (MSU2) and the

outgoing longwave radiation (OLR) and obtained a leading pattern that is strongly linked to ENSO and that explains 79% of the total squared covariance.

The second singular vector (Figure 6.7 c, d) explains 10% of the squared covariance. As in the first vector, the precipitation pattern is dominated by two SW-NE oriented bands of precipitation of opposite sign over the western Pacific. Two equatorially symmetric centers of action of the same latitudinal extent to those associated with ENSO but located farther west, characterize the geopotential pattern over the central Pacific region in relation to the second singular vector. Weak anomalies of opposite sign are observed over the remainder of the domain.

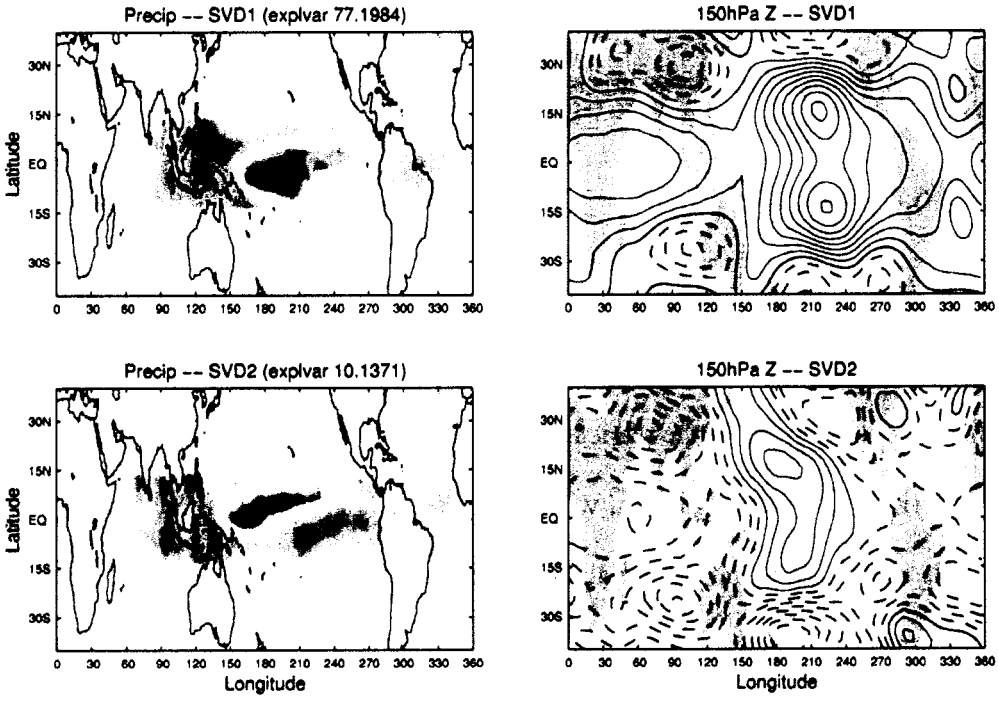

Figure 6.7: The first two emerging singular vectors (upper panels and bottom panels, respectively) emerging from an MCA between precipitation and 150hPa geopotential height, as described in text.

The standardized time series associated with these first two singular vectors (PC1 and PC2), for the precipitation field, are shown in Figure 6.8. The evolution of PC1 resembles that of the ENSO cycle. The behavior of PC2 is less clear: during 1982-83 and 1997-98 events it exhibits fluctuations that led those in PC1 by 5 to 7 months. Such a particular relationship between these two time series is interesting and deserves further investigation, however, such an analysis is beyond the scope of this study.

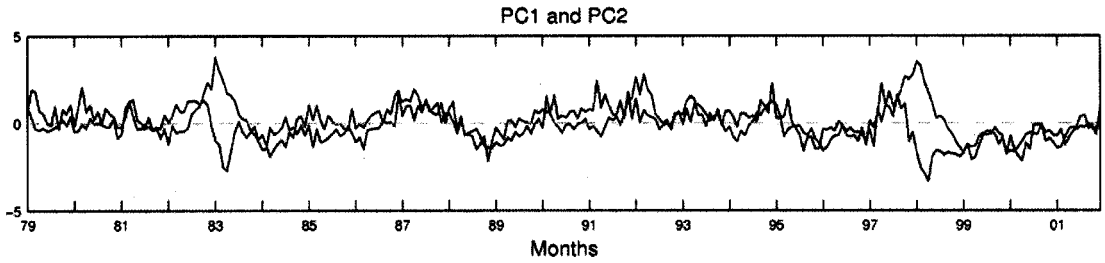

Figure 6.8: Standardized time series associated with the first two singular vectors resulted from the MCA analysis between the precipitation and the 150hPa geopotential height field: PC1 (black) and PC2 (blue).

6.4 Discussion

The main modes of tropical variability, ENSO, MJO and the annual cycle, although acting at different time scales, share important common characteristics: they can all be described as oscillations of the planetary-scale waves between two preferred states. One state describes the *relaxed* pattern, when the geopotential height is practically flat over the whole tropical belt and the zonal and meridional winds are fairly weak. Such a state is characteristic of situations with much reduced precipitation over the warm pool and a weakening of the equatorial cold tongue in the Eastern Pacific, conditions observed during El Niño (CTI+) and the boreal spring (AM). On the other hand, increased convection over the warm pool and pronounced cold tongue on the other side of the

Pacific basin enhances the east-west asymmetries over the Pacific Ocean and acts to enhance the stationary waves. In this *perturbed* state, the planetary waves, as defined by the near-equatorial wind and geopotential height patterns, are characterized by a juxtaposition of Rossby and Kelvin waves. La Nina and the months of the year other than April/May fall in this category. The patterns associated with oscillations in the amplitude of the MJO experience similar fluctuations between a relaxed state (MJO1-) and a perturbed state (MJO1+), but in this case the equatorial cold tongue is not directly involved in the process.

The composite analysis performed for rainfall rates within prescribed boxes indicates that the planetary waves are far more sensitive to fluctuations in precipitation over the maritime continent than over most any other areas in the tropics. Moreover, the MCA revealed that the preferred mode of coupled tropical variability is a pattern that describes oscillations in the east-west asymmetries over the Pacific basin, much like ENSO.

7. Summary

In this thesis we have explored different facets of the structure and variability of the tropical circulation, with emphasis on the region closest to the equator. In contrast to the numerous studies that have focused on the monsoons, which emphasize the antisymmetric component of the patterns, we mainly focused here on the equatorially symmetric component of the tropical flow and its role in the variability at low latitudes.

Lindzen and Hou (1988) argued that the idea of a single cross-equatorial Hadley cell dominates the zonally averaged tropical variability. As we have shown in Chapter 3, an equatorially symmetric pair of Hadley cells is in fact present in all months of the year and its squared amplitude is comparable to that of the equatorially asymmetric component of the MMC. We also showed that the cross-equatorial mean meridional circulation varies sinusoidally, rather than in the manner of a square-wave as argued by Lindzen and Hou. This meridional structure and temporal evolution of this seasonally varying mode are indicative of a close association with the monsoons.

This seasonally varying flow in the cross-equatorial mean meridional circulation plays a crucial role in maintaining the angular momentum balance in the equatorial region (Chapter 4). The observational study of Lee (1999) focused on the 200hPa tropospheric level and pointed out the factors contributing to the maintaining of easterly winds over the equatorial region. Were it not for the easterly momentum convergence by the annual variation of the mean meridional circulation, westerly winds produced by the convergence of westerly momentum into the equatorial region by eddy momentum

fluxes, would be dominant in the region. We have extended the analysis of Lee to include all the levels of the troposphere as given by the NCEP Reanalysis, and to demonstrate the dominance of the climatological-mean stationary waves in the momentum transport. The equatorially symmetric component of the mean eddy kinetic energy has a semi-annual variation with maximum amplitude during the monsoonal seasons instead of during the transition seasons as one might have expected. Surprisingly, the equatorially symmetric component of the eddies is dominant over the asymmetric component, and it is clearly evident during all months of the year (Chapter 4, Figure 4.18).

Beginning with Chapter 4 and continuing through the rest of the study, we consistently used the geopotential height field in describing the structure of the equatorial stationary waves, as opposed to the streamfunction field, the variable predominantly employed in depicting the tropical circulation in previous studies. To make the case stronger, we compare in Figure 7.1 the same level annual mean geopotential height and streamfunction field. While the streamfunction field is incapable of delineating much of the wave characteristics, the geopotential height field can depict all of the important wave features, e.g., the Rossby gyres, the Kelvin wave component, and the pronounced trough over the equatorial Indian Ocean. Hence, the geopotential height is, in our view, the variable of choice in describing any type of equatorial waves.

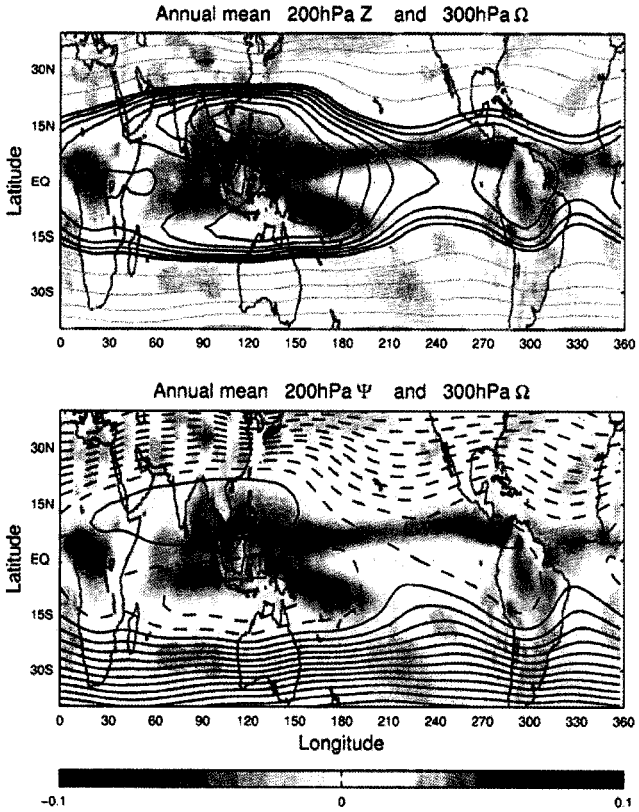

Figure 7.1: Annual mean 200hPa geopotential height (upper panel) and streamfunction field (bottom panel) (contours) and 300hPa omega (color).

The angular momentum analysis in Chapter 4 suggests another way of partitioning the earth's general circulation into latitudinal belts. The conventional partitioning, based primarily on the sign of the surface winds, consists of three belts in each hemisphere: the tropics (0°-30°), the midlatitudes (30°-60°) and the polar region (60°-90°). But if one were to consider the upper level eddy momentum transport, then the earth could be divided into four belts: (1) the equatorial region (0°-10°), (2) the outer tropics (10°-30°), (3) the midlatitudes (30°-60°) and (4) the polar region (60°-90°). These area separations are represented in Figure 7.2. Regions (1) and (3) are characterized by convergence of

momentum while (2) and (4) feature divergence of momentum. The stationary waves generated in the equatorial belt (1) bring in westerly momentum from the outer tropics and the waves generated in the extratropics (3) bring in westerly momentum from the tropics and the polar regions. The latter waves get absorbed in the outer tropics and contribute to generation of easterlies here. The northward momentum transport around 30° latitude has the largest amplitude and remains the most important feature in the transport of momentum at global scale. The momentum transport around 10° that we emphasized in this study, although much smaller in amplitude and with no direct effect on the surface winds because it is balanced by the meridional advection of momentum at upper tropospheric levels, plays its own important role in the general circulation.

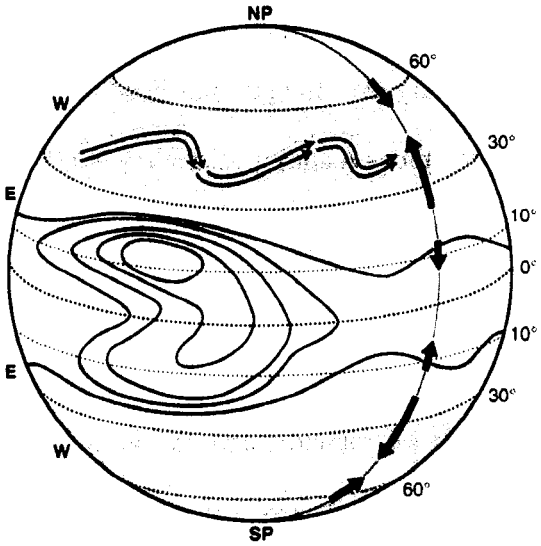

Figure 7.2: Schematic latitudinal division of the earth based on the eddy momentum convergence/divergence criteria.

An analysis of these equatorial stationary waves was performed in Chapter 5, with emphasis on the equatorially symmetric component. The maximum amplitude of these

waves is located near the level that marks the top of the deep convective clouds. The geopotential height, temperature, vertical velocity and relative humidity fields, all reach their maximum amplitude around the same longitude, 165°E. We hypothesized that the ascent taking place around this longitude in the upper tropospheric layer, much of which takes place above the tops of deep convection clouds, may be determined by the structure of the stationary wave itself rather than mirroring updrafts in convective systems. The horizontal structure and, to some extent, the high degree of equatorial symmetry of the equatorial stationary waves, were also captured in the shallow water wave equation model runs that we performed.

The annual cycle, ENSO and MJO all affect the structure of the predominantly equatorially symmetric stationary waves by modulating the precipitation over the Indo-Pacific warm pool or perturbing the strength and position of the eastern Pacific cold tongue (Chapter 6). Hence, the equatorial stationary waves are modulated by the longitudinal east-west asymmetries, most evident in the Pacific basin. The upper tropospheric stationary waves respond by oscillating between two distinct states which we described as *perturbed* and *relaxed.* Composite analyses and MCA calculations indicate that the leading mode of tropical variability is indeed a pattern that resembles ENSO and involves the thermal contrast across the Pacific Ocean.

Bibliography

Atticks, M. and G. Robinson, 1983: Some features of the structure of the tropical tropopause. *Q. J. R. Meteorol. Soc.*, Vol. 109, 295-308.

Barnett, T. P., 1984: Interaction of the Monsoon and Pacific Trade Wind System at Interannual Time Scales. Part III: A partial Anatomy of the Southern Oscillation. *Mon. Wea. Rev.*, Vol. 112, 2388–2400.

Bjerknes, J., 1969: Atmospheric teleconnections from the equatorial Pacific. *Mon. Wea. Rev.*, Vol. 97, 163-172.

Bretherton, C. S., C. Smith and J. M. Wallace, 1992: An Intercomparison of Methods for Finding Coupled Patterns in Climate Data. *J. Climate*, Vol. 5, 541–560.

Ciesielski, P. E., R. H. Johnson, P. T. Haertel and J. Wang. 2003: Corrected TOGA COARE Sounding Humidity Data: Impact on Diagnosed Properties of Convection and Climate over the Warm Pool. *J. Climate*, Vol. 16, 2370–2384.

Chiang, J. C., S. E. Zebiak and M. A. Cane, 2001: Relative Roles of Elevated Heating and Surface Temperature Gradients in Driving Anomalous Surface Winds over Tropical Oceans. *J. Atmos. Sci.*, Vol. 58, 1371–1394.

Christian H. J., and authors, 2003: Global frequency and distribution of lightning as observed from space by the Optical Transient Detector, *J. Geophys. Res.*, Vol. 108 (D1), 4005, doi: 10.1029 / 2002JD002347.

Das, P. K., 1986: Monsoon Meteorology. *World Meteorological Organization*, 850 pp.

DeWeaver, E. and S. Nigam. 2000: Do Stationary Waves Drive the Zonal-Mean Jet Anomalies of the Northern Winter? *J. Climate*, Vol. 13, 2160–2176.

Dima, I. M., 2002 (Master Thesis): Annular structures in low latitude wind and temperature variability. *University of Washington Libraries*, QC852 Th51192, location nsstx. 39352058507450.

—— and J. M. Wallace, 2003: On the seasonality of the Hadley cell. *J. Atmos. Sci.*, Vol. 60, 1522–1527.

——, J. M. Wallace and I. Kraucunas, 2005: Tropical zonal momentum balance in the NCEP Reanalyses. *J. Atmos. Sci.*, Vol. 62, 2499-2513.

Fang, M., and K. K. Tung, 1999: Time-dependent nonlinear Hadley circulation. *J. Atmos. Sci.*, Vol. 56, 1797–1807.

Fleming, E. L., G.-H. Lim and J. M. Wallace, 1987: Differences between the spring and autumn circulation of the northern hemisphere. *J. Atmos. Sci.*, Vol. 44, 1266–1286.

Fueglistaler S., H. Wernli, T. Peter, 2004: Tropical troposphere-to-stratosphere transport inferred from trajectory calculations. *J. Geophys. Res.*, Vol. 109, D03108, doi: 10.1029 / 2003JD004069.

Hendon, H. H., 1986: Time-Mean Flow and Variability in a Nonlinear Model of the Atmosphere with Orographic Forcing. *J. Atmos. Sci.*, Vol. 43, 433–448.

Hartmann, D. L. and K. Larson, 2002: An Important Constraint on Tropical Cloud-Climate Feedback. *Geophys. Res. Lett.*, Vol. 29 (20), 1951, 4, doi: 10.1029 / 2002GL015835.

Gettelman, A., M. L. Salby, and F. Sassi, Distribution and influence of convection in the tropical tropopause region, *J. Geophys. Res.*, 107 (D10), 4080, doi:10.1029 / 2001JD001048.

Gill, A. E., 1980: Some simple solutions for heat-induced tropical circulation. Q. J. R. Meteorol. Soc., Vol. 106, 447-462.

Glickman, T., Ed., 2000: Glossary of Meteorology. 2nd ed. American Meteorological Society, 855 pp.

Hadley, G., 1735: Concerning the cause of the general trade-winds. *Phil. Trans.*, Vol. 29, 58–62.

Held, I. M. and A. Y. Hou, 1980: Nonlinear axially symmetric circulations in a nearly inviscid atmosphere. *J. Atmos. Sci.*, Vol. 37, 515-533.

——, M. Ting and H. Wang, 2002: Northern Winter Stationary Waves: Theory and Modeling. *J. Climate*, Vol. 15, 2125-2144.

Hendon, H. H. and D. L. Hartmann. 1982: Stationary Waves on a Sphere: Sensitivity to Thermal Feedback. *J. Atmos. Sci.*, Vol. 39, 1906–1920.

Highwood, E. J. and B. J. Hoskins, 1998: The tropical Tropopause. *Q. J. R. Meteorol. Soc.*, Vol. 124, 1579-1604.

Holton, J. R., and A. Gettelman 2001: Horizontal transport and the dehydration of the stratosphere. *Geophys. Res. Lett.*, Vol. 28 (14), 2799–2802.

Hou, A. Y. and R. S. Lindzen, 1992: The influence of concentrated heating on the Hadley circulation. *J. Atmos. Sci.*, Vol. 49, 1233–1241

Hsu, H H , 1996: Global View Of The Intraseasonal Oscillation During Northern Winter. *J. Climate*, Vol. 9, 2386-2406.

Jackson, D. R., J. Methven and V. D. Pope, 2001: Transport in the Low-Latitude Tropopause Zone Diagnosed Using Particle Trajectories. *J. Atmos. Sci.*, Vol. 58, 173–192.

Kalnay, E., M. Kanamitsu, R. Kistler, W. Collins and co authors, 1996: The NCEP/NCAR 40-year reanalysis project. *Bull. Amer. Meteor. Soc.*, Vol. 77, 437–471.

Kraucunas, I. P. and D. L. Hartmann, 2005: Equatorial superrotation and the factors controlling the zonal-mean zonal winds in the tropics. *J. Atmos. Sci.*, Vol. 62, 371–389.

——, 2005: The influence of hemispheric asymmetry and realistic basic states on tropical staitonary waves in a nonlinear shallow water model. - submitted -

Kutzbach, J. E., 1967: Empirical eigenvectors of sea-level pressure, surface temperature and precipitation complexes over North America. *J. Appl. Meteorol.*, Vol. 6, 91-802.

Lau, N-C, 1979: The Observed Structure of Tropospheric Stationary Waves and the Local Balances of Vorticity and Heat. *J. Atmos. Sci.*, Vol. 36, 996-1016.

Lau, K.-M. and P. H. Chan. 1988: Intraseasonal and Interannual Variations of Tropical Convection: A Possible Link between the 40–50 Day Oscillation and ENSO? *J. Atmos. Sci.*, Vol. 45, 506–521.

—— and S. Shen. 1988: On the Dynamics of Intraseasonal Oscillations and ENSO. *J. Atmos. Sci.*, Vol. 45, 1781–1797.

Lea, D. W., D. K. Pak, L. C. Peterson, K. A. Hughen, 2003: Synchroneity of Tropical and High-Latitude Atlantic Temperatures over the Last Glacial Termination. *Science*, Vol 301, 1361-1364, doi: 10.1126/science.1088470.

Lee, S., 1999: Why are the climatological zonal winds easterly in the equatorial upper troposphere. *J.Atmos. Sci.*, Vol. 56, 1353–1363.

Lindzen, R. S. and A. Y. Hou, 1988: Hadley circulations for zonally averaged heating centered off the equator. *J. Atmos. Sci.*, Vol. 45, 2416–2427.

—— and S. Nigam. 1987: On the Role of Sea Surface Temperature Gradients in Forcing Low-Level Winds and Convergence in the Tropics. *J. Atmos. Sci.*, Vol. 44, 2418–2436.

Lorenz, E. N., 1967: The nature and theory of the general circulation of the atmosphere. *Tech. Doc.* 218, World Meteorological Organization, 161 pp.

——, 1956: Empirical orthogonal functions and statistical weather prediction. *Scientific Report No.1*, Statistical Forecasting Project, MIT, Department of Meteorology.

Madden, R. A. and P. R. Julian, 1994: Observations of the 40–50-Day Tropical Oscillation—A Review. *Mon. Wea. Rev.*, Vol. 122, 814–837.

Matsuno, T., 1966: Quasi-geostrophic motions in the equatorial area. *J. Met. Soc. Japan*, Vol. 44, 25–42.

McPhaden, M. J., A. J. Busalacchi, R. Cheney, J.-R. Donguy, K. S. Gage, D. Halpern, M. Ji, P. Julian, G. Meyers, G. T. Mitchum, P. P. Niiler, J. Picaut, R. W. Reynolds, N. Smith, K. Takeuchi, 1998: The Tropical Ocean-Global Atmosphere observing system: A decade of progress. J. Geophys. Res., Vol. 103 (C7), 14169-14240, doi: 10.1029/97JC02906.

Mitchell, T. P. and J. M. Wallace, 1992: The Annual Cycle in Equatorial Convection and Sea Surface Temperature. *J. Climate*, Vol. 5, 1140–1156.

Newell, R. E., J. W. Kidson, D. G. Vincent, and G. J. Boer, 1972: The General Circulation of the Tropical Atmosphere and Interactions with Extratropical Latitudes. *MIT Press*, Vol. 1, 258 pp.

North, G. R., T. L. Bell, R. F. Cahalan and F. J. Moeng, 1982: Sampling erorrs in the estimation of empirical orthogonal functions. *Mon. Wea. Rev.*, Vol. 110, 699-706.

Oort, A. H. and E. M. Rasmusson, 1970: On the annual variation of the monthly mean meridional circulation. *Mon. Wea. Rev.*, Vol. 98, 423-442.

—— and J. J. Yienger, 1996: Observed interannual variability in the Hadley circulation and its connection to ENSO. *J. Climate*, Vol. 9, 2751–2767.

—— and J. P. Peixoto, 1983: Global angular momentum and energy balance requirements from observations. *Advances in Geophysics,* Vol. 25, Academic Press, 355–490.

Peixoto, J. P., and A. H. Oort, 1992: Physics of Climate. *American Institute of Physics*, USA, 520 pp.

Ramage, C.S., 1971: Monsoon Meteorology. *Academic Press*, 296 pp.

Rasmusson E. M. and T. H. Carpenter, 1982: Variations in Tropical Sea Surface Temperature and Surface Wind Fields Associated with the Southern Oscillation/El Niño. *Mon. Wea. Rev.*, Vol. 110, 354–384.

Rosen, R. R. and D. A. Salstein, 1980: A comparison between circulation statistics computed from conventional data and nmc hough analyses. *Mon. Wea. Rev.*, Vol. 108, 1226–1247.

Saravanan, R., 1993: Equatorial superrotation and maintenance of the general circulation in two-level models. *J. Atmos. Sci.*, Vol. 50, 1211-1227.

Sardeshmukh, P.D. and B.J. Hoskins, 1988: The generation of global rotational flow by idealised tropical divergence. *J. Atmos. Sci.*, Vol. 45, 1228-1251.

Schneider, E.K. and R.S. Lindzen, 1977: Axially symmetric steady-state models of the basic state for instability and climate studies. Part I. Linearized calculations. *J. Atmos. Sci.*, Vol. 34, 263-279.

——, 1977: Axially symmetric steady-state models of the basic state for instability and climate studies. Part II - Nonlinear calculations. *J. Atmos. Sci.*, Vol 34, 280-296.

——, 1984: Response of the annual and zonal mean winds and temperatures to variations in the heat and momentum sources. *J. Atmos. Sci.*, Vol. 41, 1093-1115.

Schulman, L. L., 1973: On the summer hemisphere Hadley cell. *Quart. J. Roy. Meteor. Soc.*, 99, 197–201.

Seltzer, G. O., D. T. Rodbell, P. A. Baker, S. C. Fritz, P. M. Tapia, H. D. Rowe, and R. B. Dunbar, 2002: Early Warming of Tropical South America at the Last Glacial-Interglacial Transition. *Science*, Vol 296, 1685-1686, doi: 10.1126 / science. 1070136.

Simmons, A. J., and J. K. Gibson, 2000: The ERA-40 Project Plan. *ERA-40 Project Report Series No. 1*, 63 pp., Eur. Cent. for Medium-Range Weather Forecasts, Reading, UK.

Starr, V. P., 1948: An essay on the general circulation of the earth's atmosphere. *J. Meteor.*, Vol. 5, 39–43.

Starr, V. P., J. P. Peixoto and N. E. Gaut, 1970: Momentum and zonal kinetic energy balance of the atmosphere from five years of hemispheric data. *Tellus*, Vol. 22, 251–274.

Suarez, M. J., and D. G. Duffy, 1992: Terrestrial superrotation: A bifurcation of the general circulation. *J. Atmos. Sci.*, Vol. 49, 256–269.

Trenberth, K. E., D. P. Stepaniak and J. M. Caron. 2000: The Global Monsoon as Seen through the Divergent Atmospheric Circulation. *J. Climate*, Vol. 13, 3969–3993.

Tuyl, A. H. V., 1986: Advective influences on forced tropical motions. *J. Atmos. Sci.*, Vol. 43, 141–161.

Wallace, J. M., 1983: Contribution in "Large-scale dynamical processes in the atmosphere". *Academic Press*, University of Reading, England, 393 pp.

——, E. M. Rasmusson, T. P. Mitchell, V. E. Kousky, E. S. Sarachik, and H. v. Storch, 1998: On the structure and evolution of ENSO-related climate variability in the tropical Pacific: Lessons from TOGA. *J. Geophys. Res.*, Vol. 103, 14241-59.

Walker, G.T., 1924: Correlations in seasonal variations of weather. I. A further study of world weather. *Mem. Indian Meteorol. Dep.* 24, 275-332.

Webster, P. J. and R. Lukas, 1992: TOGA COARE: The Coupled Ocean—Atmosphere Response Experiment. *Bull. Amer. Meteor. Soc.*, Vol. 73, 1377–1416.

Webster, P. J., 1972: Response of the tropical atmosphere to local steady forcing. *Mon. Wea. Rev.*, Vol. 100, 518-541.

Walker, C. C. and T. Schneider, 2005: Response of idealized Hadley circulations to seasonally varying heating. *Geophys. Res. Lett.*, Vol. 32, L06813, doi: 10.1029 / 2004GL022304.

Webster, P. J., V. O. Magan˜a, T. N. Palmer, J. Shukla, R. A. Tomas, M. Yanai, and T. Yasunari, 1998: Monsoons: Processes, predictability and the prospects for prediction. *J. Geophys. Res.,* Vol. 103, 14 451– 14 510.

Wheeler, M. C. and H. H. Hendon, 2004: An All-Season Real-Time Multivariate MJO Index: Development of an Index for Monitoring and Prediction. *Mon. Wea. Rev.*, Vol. 132, 1917–1932.

Wu, Z., E. S. Sarachik and D. S. Battisti, 2000: Vertical Structure of Convective Heating and the Three-Dimensional Structure of the Forced Circulation on an Equatorial Beta Plane. *J. Atmos. Sci.,* Vol. 57, 2169–2187.

——, D. S. Battisti and E. S. Sarachik, 2000: Rayleigh Friction, Newtonian Cooling, and the Linear Response to Steady Tropical Heating. *J. Atmos. Sci.,* Vol. 57, 1937–1957.

Xie, P. and P. A. Arkin, 1997: Global precipitation: A 17-year monthly analysis based on guage observations, satellite estimates, and numerical model outputs. *Bull. Amer. Meteor. Soc.*, Vol. 78, 2539-2558.

Yu, J.-Y., C. Chou and J. D. Neelin. 1998: Estimating the Gross Moist Stability of the Tropical Atmosphere. *J. Atmos. Sci.*, Vol. 55, 1354–1372.

Yulaeva, E. and J. M. Wallace, 1994: The signature of ENSO in global temperature and precipitation fields derived from the Microwave Sounding Unit. *J. Climate*, Vol. 7, 1719-1736.

Appendix A

Robustness of patterns with respect to the 1979-2001 trend

Throughout the study we consistently used data covering the 1979-2001 time period. As mentioned in Chapter 2, we chose to restrict ourselves to this particular period as to work with data that incorporated satellite-based remote sensing data that became available after 1979. But this recent period is also a time of significant global warming trends. Figure A.1 shows the monthly average temperature anomalies from the period with best coverage (1961-1990). The upward trend of the last two decades stands out clearly.

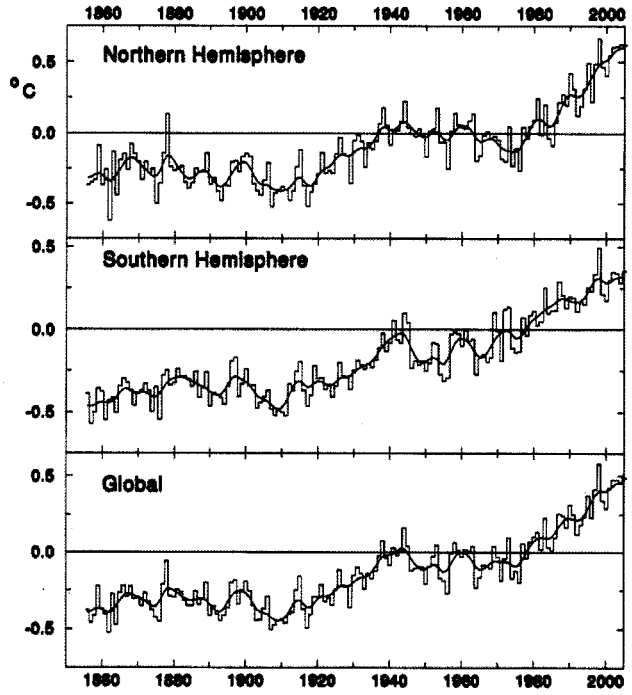

Figure A.1: Hemispheric and global average temperature trends (http://www.cru.uea.ac.uk/cru/data/temperature/).

Hence, it is reasonable to question whether the results presented in this study are affected by the non-stationarity of the data or not. To address this question we recomputed selected patterns based on data for the first and last quarter of the record. Two examples of such computations are presented in Figures A.2 and A.3.

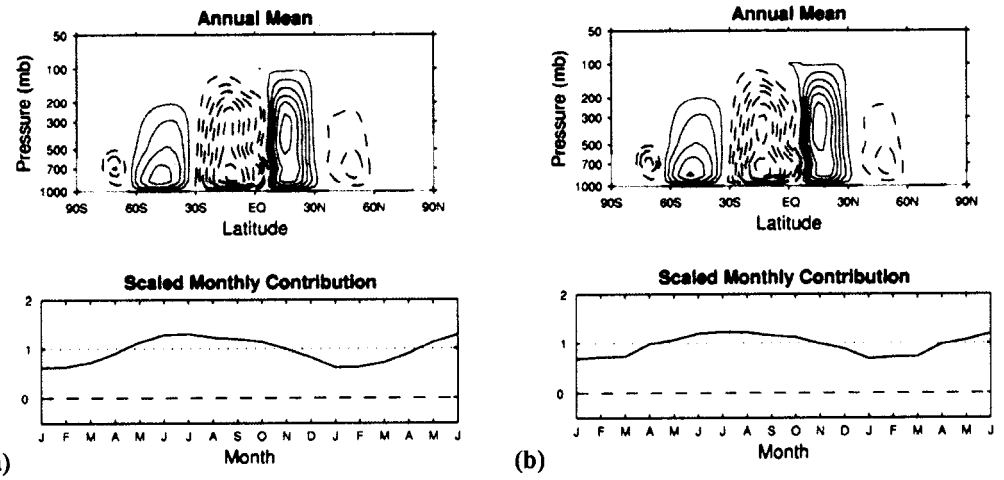

Figure A.2: Same as in Figure 3.5 but for (a) 1979-1984 and (b) 1996-2001.

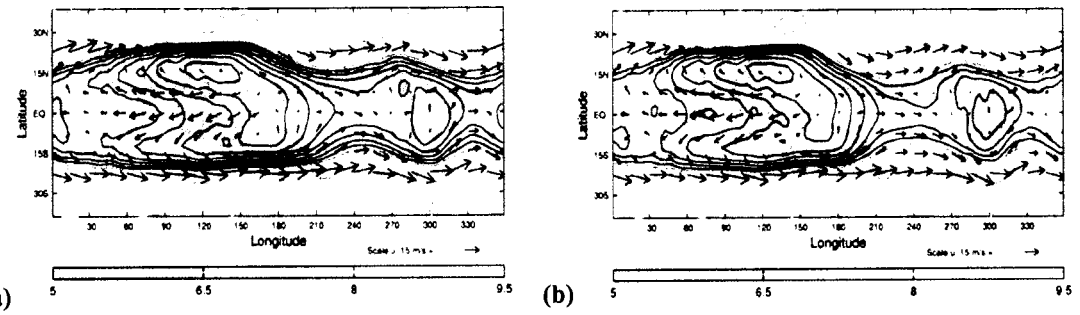

Figure A.3: Same as in Figure 4.4 but for (a) 1979-1984 and (b) 1996-2001.

As one can notice, the differences between the patterns in panels (a) and (b) are very small. This is true for the structure of the patterns as well as their amplitudes. Similarly insignificant differences are discernable when one compares these figures with their analogues for the entire period (Figure 3.5 and 4.4, respectively). We

conclude that the global warming trend characterizing the time period considered in our analysis, although significant, it does not affect our results or general conclusions.

Appendix B

Error evaluation in closing the momentum budget

In the budget analysis presented in Chapter 4 we focused on the terms with greatest influence in controlling the upper troposphere equatorial zonal wind. The NCEP Reanalysis data used represent model output and is not free from errors. Hence, one can not expect the global momentum budget to balance exactly. In our analysis we have considered the momentum equation to be in balance when the residual term is much smaller than the leading terms in the budget.

In order to estimate the errors involved in closing the momentum budget in our region of interest, we revisit equation 4.1 (reproduced below) and closely compare the amplitudes of *all* the terms in the equation. For long enough periods of time, as considered in our analysis, the wind tendency ($\partial[u]/\partial t$) on the left hand side of the equation approaches zero. We want to verify to what extent the sum of the terms on the right hand side of the equation also approaches zero. The only assumption we make in our analysis is that the friction term ($[F_x]$) at the upper tropospheric levels we concentrate on, is small enough to be neglected.

$$\frac{\partial[u]}{\partial t} \cong [v]\left(f - \frac{1}{\cos\phi}\frac{\partial[u]\cos\phi}{\partial y}\right) - [\omega]\frac{\partial[u]}{\partial p} - \frac{1}{\cos^2\phi}\frac{\partial[u^*v^*]\cos^2\phi}{\partial y} - \frac{\partial[u^*\omega^*]}{\partial p} - [F_x]$$

(a) **(b)** **(c)** **(d)**

The four remaining terms on the RHS of the equation, the horizontal (a) and vertical (b) momentum convergence by the MMC and the horizontal (c) and vertical (d)

eddy momentum convergence, are shown in Figure B.1. Also shown in the bottom panel of the figure is the sum of all four terms or 'the residual'. Note that in order to have the terms represented side by side we used different contouring interval in (a) and (c) from (b) and (d) (see caption of the figure).

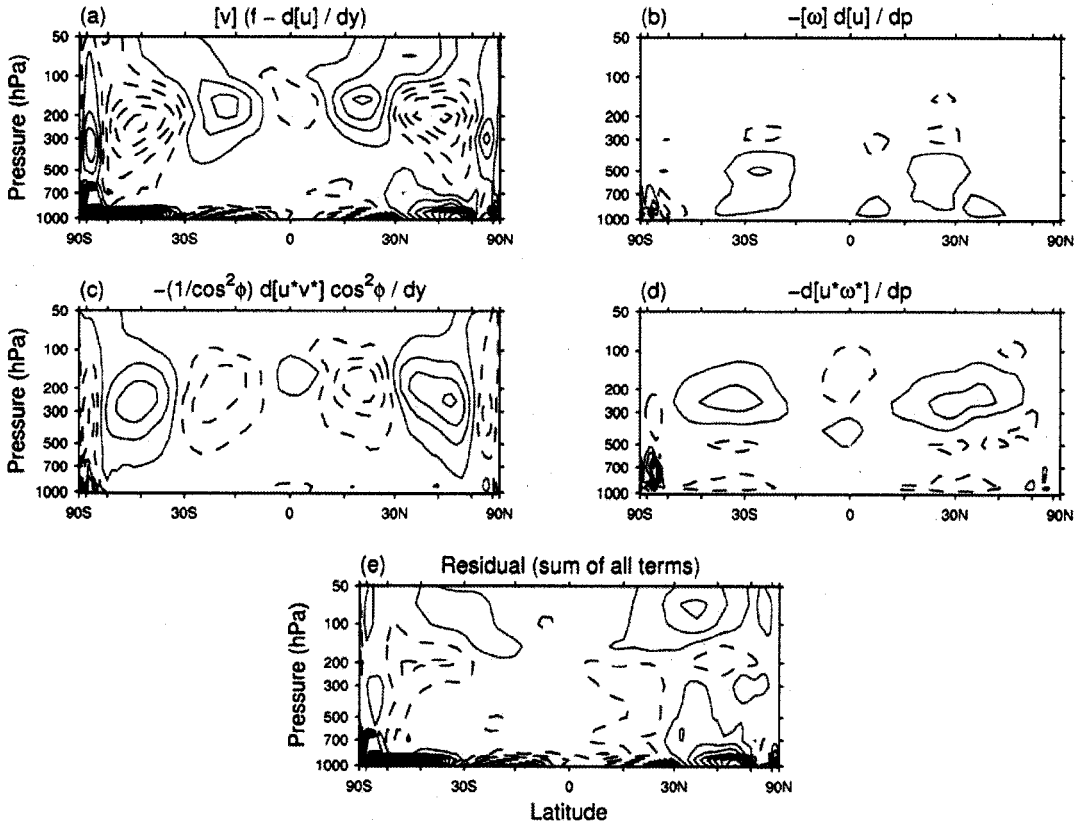

Figure B.1: The terms on the RHS in the momentum budget equation 4.1. The friction term is neglected and is not shown. The contour interval is 10×10^{-6} ms^{-2} in (a), (c) and (e) and 0.5×10^{-6} ms^{-2} in (b) and (d).

It is evident that the horizontal contribution terms (a) and (c) have similar amplitudes and structures and dominate the momentum budget, while the vertical contributions terms (b) and (d) are at least an order of magnitude smaller than their

horizontal counterparts. The corresponding numerical values for all terms, at 150hPa, on the equator, are shown in the table below.

***Table B.1**: Numerical values of terms in Figure B.1, on the equator, at 150hPa*

Term	***(a)***	***(b)***	***(c)***	***(d)***	***Residual***
Value (ms^{-2})	-7.152×10^{-6}	9.535×10^{-9}	7.225×10^{-6}	-4.691×10^{-7}	-4.053×10^{-7}

The difference between terms (a) and (c) is remarkably small. Term (d) and (b) are at least an order of magnitude smaller than any of the leading terms (a) or (c). It is clear that the overall balance is controlled by the horizontal convergence terms (a) and (c) while both vertical terms (b) and (d) have negligible contributions.

Vita

Ioana Maria Dima was born in Bucharest, Romania, on April 12, 1973, to Aurelia Eugenia Dima and Vasile N. Dima. She followed the steps of her two older brothers, Mihai and Gabriel Dima, graduating in 1991 from the Gheorghe Lazar High School in Bucharest and receiving in 1996 her Bachelor of Science in Physics from University of Bucharest. The following year she graduated from the university's Master degree program in Atmospheric Physics. She came to United States in 1998 to begin graduate studies at the Department of Atmospheric Sciences at the University of Washington, in Seattle, under the supervision of Professor John M. Wallace. In 2002 she earned a Master of Science degree in Atmospheric Science and in 2005 she received her Ph.D. in Atmospheric Science.